



## Assignment of master's thesis

**Title:** Estimation of detection probability in multitarget filters using object advanced image processing techniques

**Student:** Bc. Michal Seibert

**Supervisor:** doc. Ing. Kamil Dedecius, Ph.D.

**Study program:** Informatics

**Branch / specialization:** Knowledge Engineering

**Department:** Department of Applied Mathematics

**Validity:** until the end of summer semester 2024/2025

### Instructions

**Abstract:** The subject of the thesis is the dynamic adjustment of the detection probability in random finite set (RFS)-based filters. These filters can track objects in noisy environments from imprecise measurements. However, they rely on the knowledge of the object (mis)detection probability. If this quantity is set inappropriately, the filters are oversensitive and prone to track loss. However, there is no convenient methodology for a consistent estimation of the detection probability. The present thesis aims to focus on its inference using algorithms for object detection and image segmentation. For object detection, the YOLO model should be used, for segmentation, the Segment anything from Meta AI is a possible way towards a solution. These models can recognize various objects in the image. It is conjectured that the combination of these algorithms can yield a filter with good robustness to target misdetections.

The goals are as follows:

- study the principles of the multitarget tracking algorithms
- study the principles of image segmentation and object detection
- propose a technique for estimation of object detection probability
- perform assessment of the proposed algorithm and discuss the obtained results

Literature:

- [1] A. F. Garcia-Fernandez, A. S. Rahmathullah, and L. Svensson, "A Metric on the Space of Finite Sets of Trajectories for Evaluation of Multi-Target Tracking Algorithms," IEEE Trans.



Signal Process., vol. 68, pp. 3917–3928, 2020, doi: 10.1109/TSP.2020.3005309.

[2] R. Mahler, Advances in Statistical Multisource-Multitarget Information Fusion. Artech house, 2014.

[3] B. N. Vo and W. K. Ma, "The Gaussian mixture probability hypothesis density filter," IEEE Transactions on Signal Processing, vol. 54, no. 11, pp. 4091–4104, 2006, doi: 10.1109/TSP.2006.881190.

[4] L. Stone, R. Streit, T. Corwin, and K. Bell, Bayesian Multiple Target Tracking. Artech house, 2013.

[5] R. R. Sanaga, "Multi-target tracking with uncertainty in the probability of detection," MSc. Thesis, Purdue Univ., 2019.



Master's thesis

**ESTIMATION OF  
DETECTION PROBABILITY  
IN MULTITARGET FILTERS  
USING OBJECT ADVANCED  
IMAGE PROCESSING  
TECHNIQUES**

**Bc. Michal Seibert**

Faculty of Information Technology  
Department of Applied Mathematics  
Supervisor: doc. Ing. Dedecius Kamil, Ph.D.  
April 29, 2024

Czech Technical University in Prague

Faculty of Information Technology

© 2024 Bc. Michal Seibert. All rights reserved.

*This thesis is school work as defined by Copyright Act of the Czech Republic. It has been submitted at Czech Technical University in Prague, Faculty of Information Technology. The thesis is protected by the Copyright Act and its usage without author's permission is prohibited (with exceptions defined by the Copyright Act).*

Citation of this thesis: Seibert Michal. *Estimation of detection probability in multitarget filters using object advanced image processing techniques*. Master's thesis. Czech Technical University in Prague, Faculty of Information Technology, 2024.

# Contents

<b>Acknowledgments</b>	<b>vii</b>
<b>Declaration</b>	<b>viii</b>
<b>Abstract</b>	<b>ix</b>
<b>List of abbreviations</b>	<b>x</b>
<b>1 Introduction</b>	<b>1</b>
1.1 Evolution and development of multi-target tracking . . . . .	1
1.2 Applications of multi-target tracking . . . . .	2
1.3 Research interests . . . . .	2
1.4 Structure . . . . .	4
<b>2 Theoretical Background</b>	<b>6</b>
2.1 Bayesian inference . . . . .	6
2.2 Bayes' rule . . . . .	7
2.3 Multivariate Gaussian distribution . . . . .	8
2.4 Gaussian mixture . . . . .	11
2.5 State-space model . . . . .	11
2.5.1 Constant velocity model . . . . .	14
2.5.2 Constant acceleration model . . . . .	16
2.6 Hidden Markov Model . . . . .	17
2.7 Bayes' filter . . . . .	18
2.8 Kalman filter . . . . .	19
2.8.1 Kalman filter inference . . . . .	20
<b>3 Target tracking</b>	<b>23</b>
3.1 Data association . . . . .	24
3.2 Clutter . . . . .	24
3.2.1 Validation region . . . . .	24
3.3 Single target tracking . . . . .	27
3.3.1 PDA filter . . . . .	27
3.4 Multi-target tracking . . . . .	30
3.4.1 RFS statistics . . . . .	31
3.4.2 PHD filter . . . . .	33
<b>4 Object detection and segmentation</b>	<b>42</b>
4.1 Object detection . . . . .	42
4.1.1 YOLO . . . . .	45
4.2 Image segmentation . . . . .	46
4.2.1 Semantic segmentation . . . . .	47
4.2.2 Instance segmentation . . . . .	47
4.2.3 Panoptic segmentation . . . . .	48

4.2.4	Traditional image segmentation . . . . .	49
4.2.5	Deep learning image segmentation . . . . .	50
4.2.6	Segment Anything . . . . .	53
4.2.7	Grounded Segment Anything . . . . .	54
<b>5</b>	<b>Dynamic time and state varying detection probability</b>	<b>56</b>
5.1	Problem definition . . . . .	56
5.1.1	The modified GM-PHD filter . . . . .	57
5.1.2	S1: YOLO + PHD . . . . .	59
5.1.3	S2: YOLO + SAM + PHD . . . . .	60
5.1.4	S3: Grounded SAM + PHD . . . . .	61
5.2	Dynamic detection probability in video data . . . . .	62
5.3	Modified pruning for GM-PHD filter . . . . .	65
5.4	Merging in GM-PHD filter with dynamic detection probability . . . . .	67
<b>6</b>	<b>Experiments</b>	<b>70</b>
6.1	E1: Traffic without any obstacle . . . . .	71
6.1.1	V1 . . . . .	71
6.1.2	V1 – GM-PHD with the constant detection probability . . . . .	71
6.1.3	V1 – GM-PHD with the dynamic detection probability . . . . .	74
6.1.4	V2 . . . . .	81
6.1.5	V2 – GM-PHD with the constant detection probability . . . . .	82
6.1.6	V2 – GM-PHD with the dynamic detection probability . . . . .	84
6.2	E2: Traffic with an obstacle . . . . .	90
6.2.1	V3 . . . . .	90
6.2.2	V3 - GM-PHD with the constant detection probability . . . . .	91
6.2.3	V3 – GM-PHD with the dynamic detection probability . . . . .	93
6.2.4	V2a . . . . .	98
6.2.5	V2a – GM-PHD with the dynamic detection probability . . . . .	98
6.2.6	V2b . . . . .	100
6.2.7	V2b – GM-PHD with the dynamic detection probability . . . . .	101
6.3	E3: Changing the model . . . . .	102
6.3.1	V2 . . . . .	103
6.3.2	V2b – GM-PHD with the dynamic detection probability . . . . .	104
<b>7</b>	<b>Conclusion</b>	<b>109</b>
<b>Gitlab repository</b>		<b>115</b>

## List of Figures

2.1 Examples of plots of multivariate Gaussian distribution. . . . .	10
2.2 Gaussian distribution with corresponding marginals. . . . .	10
2.3 Examples of plots of multivariate Gaussian mixture distribution. There are three components in figures with means $\{[0, 0], [3, 3], [-3, -1]\}$ . Note that the density of peaks is very low, because the sum has to be equal 1. . . . .	12
2.4 Gaussian mixture distribution with means $\{[0, 0], [2, 2]\}$ , weights $\{[0.6, 0.4]\}$ and corresponding marginals. . . . .	12
2.5 Demonstration of the course of the hidden Markov process. . . . .	18
 3.1 Several measurements $z_i$ appeared in the validation region of a single target. $\hat{z}$ is a predicted measurement and none or any of the measurement $z_1 - z_3$ may have originated from the target. . . . .	26
3.2 Several measurements $z_i$ appeared in the validation region of one of targets $\hat{z}_1$ or $\hat{z}_2$ . $\hat{z}_1$ and $\hat{z}_2$ are predicted measurements and none or any of the measurement $z_1 - z_3$ may have originated from the target $\hat{z}_1$ and none or any of the measurement $z_3 - z_4$ may have originated from the target $\hat{z}_2$ . . . . .	27
 4.1 Image detection and segmentation task types. (Source: techvidvan.com). . . . .	43
4.2 CNN architecture example. (Source learnopencv.com) . . . . .	44
4.3 Yolo architecture proposed in [35] has 24 convolutional layers followed by 2 fully connected layers. Convolutional layers were pretrained on the ImageNet classifier at half resolution (224 x 224 input image) and the doubled the resolution for detection. (Source [35].) . . . . .	46
4.4 U-net architecture (example for 32x32 pixels in the lowest resolution). (Source [55]) . .	51
4.5 Transformer architecture. (Source [57]) . . . . .	51
4.6 Multi-head attention. (Source [57]) . . . . .	52
4.7 SAM architecture (Source [62]) . . . . .	54
4.8 The demonstration of SAM's performance. These masks were annotated fully automatically by SAM and are part of the SA-1B dataset. (Source [62]) . . . . .	54
 5.1 YOLO segmentation example. This picture shows all detected objects the YOLO model is trained for and also the segmented objects' masks. These masks are imperfect, but often sufficient enough. (Kartouzská street, Prague) . . . . .	60
5.2 Comparison of using only a bounding box vs combination of a bounding box and a point as an input for SAM. . . . .	61
5.3 The cooperation of YOLO and SAM models. The YOLO provides bounding boxes of objects, which are inputs to SAM. The SAM model then makes segmented masks of these objects. (Kartouzská street, Prague) . . . . .	61
5.4 The result of the Grounded SAM model. Grounding DINO marks objects with bounding boxes and SAM segments objects inside these bboxes. Marked objects are founded by Grounding DINO with text input <i>person, car</i> . (Kartouzská street, Prague) . . . . .	62
 6.1 Development chart of number of detected targets, targets in the filter's queue, displayed targets and the true targets' count. . . . .	73

6.2	Image sequence of tracked objects using the GM-PHD filter with the constant detection probability. . . . .	74
6.3	Development chart of the number of detected targets, targets in the filter's queue, displayed targets and the true targets' count. . . . .	76
6.4	Image sequence of tracked objects using the GM-PHD filter with the dynamic detection probability and YOLO only. . . . .	77
6.5	Development chart of the number of detected targets, targets in the filter's queue, displayed targets and the true targets' count. . . . .	78
6.6	Image sequence of tracked objects using the GM-PHD filter with the dynamic detection probability, the YOLO object detector and the SAM image segmentation model. . . . .	79
6.7	Development chart of the number of detected targets, targets in the filter's queue, displayed targets and the true targets' count. . . . .	80
6.8	Image sequence of tracked objects using the GM-PHD filter with the dynamic detection probability and the Grounded SAM model. . . . .	81
6.9	Development chart of the number of detected targets, targets in the filter's queue, displayed targets and the true targets' count. . . . .	83
6.10	Image sequence of tracked objects using the GM-PHD filter with the constant detection probability. . . . .	83
6.11	Development chart of the number of detected targets, targets in the filter's queue, displayed targets and the true targets' count. . . . .	85
6.12	Image sequence of tracked objects using the GM-PHD filter with the dynamic detection probability and YOLO only. . . . .	86
6.13	Development chart of the number of detected targets, targets in the filter's queue, displayed targets and true targets' count. . . . .	87
6.14	Image sequence of tracked objects using the GM-PHD filter with the dynamic detection probability, the YOLO object detector and the SAM image segmentation model. . . . .	88
6.15	Development chart of the number of detected targets, targets in the filter's queue, displayed targets and true targets' count. . . . .	89
6.16	Image sequence of tracked objects using the GM-PHD filter with the dynamic detection probability, the DINO object detector and the SAM image segmentation model. . . . .	90
6.17	Development chart of the number of detected targets, targets in the filter's queue, displayed targets and true targets' count. . . . .	92
6.18	Image sequence of tracked objects using the GM-PHD filter with the constant detection probability. . . . .	92
6.19	Development chart of the number of detected targets, targets in the filter's queue, displayed targets and true targets' count. . . . .	94
6.20	Image sequence of tracked objects using the GM-PHD filter with the dynamic detection probability and YOLO only. . . . .	94
6.21	Development chart of the number of detected targets, targets in the filter's queue, displayed targets and true targets' count. . . . .	95
6.22	Image sequence of tracked objects using the GM-PHD filter with the dynamic detection probability, the YOLO object detector and the SAM image segmentation model. . . . .	96
6.23	Development chart of the number of detected targets, targets in the filter's queue, displayed targets and true targets' count. . . . .	97
6.24	Image sequence of tracked objects using the GM-PHD filter with the dynamic detection probability, the DINO object detector and the SAM image segmentation model. . . . .	98
6.25	Image sequence of the tracked objects using the GM-PHD filter with the dynamic detection probability and YOLO only. . . . .	100
6.26	Image sequence of tracked objects using the GM-PHD filter with the dynamic detection probability and YOLO only. . . . .	102
6.27	Image sequence of tracked objects using the GM-PHD filter with the dynamic detection probability, Grounded SAM and adjusted models – part 1. . . . .	105

6.28	Image sequence of tracked objects using the GM-PHD filter with the dynamic detection probability, Grounded SAM and adjusted models – part 2 . . . . .	106
6.29	The evolution of targets' detection probabilities and weights. . . . .	107

## List of Tables

6.1	The parameter settings for Experiment E1-V1 with the constant detection probability. . . . .	71
6.2	The parameter settings for Experiment E1-V1-S1 with the dynamic detection probability.	75
6.3	The parameter settings for Experiment E1-V1-S2 with the dynamic detection probability.	78
6.4	The parameter settings for Experiment E1-V1-S3 with the dynamic detection probability.	80
6.5	The parameter settings for Experiment E1-V2 with the constant detection probability. . . .	82
6.6	The parameter settings for Experiment E1-V2-S1 with the dynamic detection probability.	84
6.7	The parameter settings for Experiment E1-V2-S2 with the dynamic detection probability.	86
6.8	The parameter settings for Experiment E1-V2-S3 with the dynamic detection probability.	88
6.9	The parameter settings for Experiment E2-V3 with the constant detection probability. . . .	91
6.10	The parameter settings for Experiment E2-V3-S1 with the dynamic detection probability.	93
6.11	The parameter settings for Experiment E2-V3-S2 with the dynamic detection probability.	95
6.12	The parameter settings for Experiment E2-V3-S3 with the dynamic detection probability.	96
6.13	The parameter settings for Experiment E2-V2a-S1 with the dynamic detection probability.	99
6.14	The parameter settings for Experiment E2-V2b-S1 with the dynamic detection probability.	101
6.15	The parameter settings for Experiment E3-V2-S3 with the dynamic detection probability.	104
6.16	The evolution of detection probabilities and weights of targets $C_L$ and $C_R$ . . . . .	107

*In the form of this thesis, I would like to express my heartfelt thanks and gratitude to many people who supported me during my studies at Faculty of Information Technology.*

*First of all let me say thank you to doc. Ing. Dedečius Kamil, Ph.D. not only for his expert guidance during writing this work, but also for introducing me to the topic of multi-target tracking, which has been a refreshing and exceptionally pleasing new problem to me, and for his immense support throughout my masters studies.*

*Furthermore, I would like to express my gratitude to my fabulous family, who supported me the most during my whole study and has always encouraged me in rough periods.*

*Last, but not least, my greatest thanks belongs to my lovely and supporting girlfriend, who has bravely withstood with me throughout my studies and always aided me to overcome challenging moments.*

## **Declaration**

I hereby declare that the presented thesis is my own work and that I have cited all sources of information in accordance with the Guideline for adhering to ethical principles when elaborating an academic final thesis.

I acknowledge that my thesis is subject to the rights and obligations stipulated by the Act No. 121/2000 Coll., the Copyright Act, as amended, in particular the fact that the Czech Technical University in Prague has the right to conclude a licence agreement on the utilization of this thesis as a school work pursuant of Section 60 (1) of the Act.

In Prague on April 29, 2024

## Abstract

This thesis focuses on the problem of multi-target tracking with noisy measurements in a cluttered environment. Algorithms for tracking multiple targets with the uncertainty in the number of targets and their survival are often sensitive to the correct setting of parameters relative to the environment. One of the key parameters is the detection probability, which is often constant. In this work, a method to estimate this probability for each target at any time step is demonstrated through tracking objects in video footages. Advanced deep-learning algorithms for image processing are utilized to provide targets' measurements. Outputs of these methods are then exploited to calculate the detection probability. To analyse the capability of the proposed method, the Gaussian mixture probability hypothesis density (GM-PHD) filter is used. This filter falls among fundamental random finite sets statistics-based multi-target algorithms. The appropriateness of the proposed method is then discussed with regards to its limitations and possible future improvements.

**Keywords** Gaussian mixture probability hypothesis density filter, multi-target tracking, image processing, detection probability, random finite sets, Markov process

## Abstrakt

Tato práce se zaměřuje na problém sledování cílů se zašuměnými měřeními v prostředí s obsahem falešných cílů. Algoritmy pro sledování více cílů s nejistotou v počtu cílů a nejistotou v jejich přežití jsou mnohdy citlivé na správné nastavení parametrů vzhledem k prostředí. Jedním z klíčových parametrů je pravděpodobnost detekce, která se mnohdy uvažuje konstantní. V této práci je představena metoda pro odhad této pravděpodobnosti pro každý cíl v každém časovém okamžiku při sledování cílů na video záznamech. K získání měření od cílů je použito pokročilých metod umělé inteligence pro zpracování obrazu, jejichž výstupy jsou využity k vypočtení pravděpodobnosti detekce. K analýze funkčnosti použitého řešení je využito Gaussian mixture probability hypothesis density (GM-PHD) filtru, který patří mezi základní algoritmy pro sledování více cílů, založené na statistice konečných náhodných množin. Vhodnost použitého řešení je poté diskutována spolu s omezeními a potenciálními budoucími možnostmi dalšího vylepšení.

**Klíčová slova** Gaussian mixture probability hypothesis density filter, sledování více cílů, zpracování obrazu, pravděpodobnost detekce, konečné náhodné množiny, Markovský proces

## List of abbreviations

STT	Single target tracking
MTT	Multi-target tracking
KF	Kalman filter
EKF	Extended Kalman filter
UKF	Unscented Kalman filter
PF	Particle filter
PDA	Probabilistic data association
IPDA	Joint probabilistic data association
JPDA	Joint probabilistic data association
MMSE	Minimum mean square error
RFS	Random finite set
FISST	Finite set statistics
MHT	Multiple hypothesis tracker
PHD	Probability hypothesis density
GM-PHD	Gaussian mixture probability hypothesis density
CPHD	Cardinalized probability hypothesis density
PMBM	Poisson multi-Bernoulli mixture
YOLO	You only look once
GMM	Gaussian mixture model
MD	Mahalanobis distance
CVM	Constant velocity model
CAM	Constant acceleration model
HMM	Hidden Markov model
CNN	Convolutional neural network
SAM	Segment anything model

# Chapter 1

## Introduction

Multi-target tracking (MTT), a fundamental aspect of surveillance and monitoring systems, has undergone significant advancements in recent years, transforming it into a critical field with diverse applications across various domains. The scope of MTT extends beyond mere tracking, encompassing tasks such as object detection, identification, and trajectory prediction. The primary goal is to maintain a comprehensive situational awareness, providing invaluable information for decision-making processes in various applications, ranging from defense and surveillance to autonomous systems and robotics. This section provides an overview of the evolution, applications, significance, and current research focus of multi-target tracking.

### 1.1 Evolution and development of multi-target tracking

Multi-target tracking has undergone a significant evolution since its inception in the early 20th century, driven by the need to track multiple objects in increasingly complex scenarios. Initially rooted in the radar technology developed during World War II [1] for single-target detection, MTT algorithms have since evolved to address a diverse range of tracking challenges.

The historical development of MTT can be traced throughout several key milestones. In the 1970s and 1980s, basic tracking algorithms emerged, laying the foundation for subsequent advancements. The integration of probabilistic techniques, notably the Kalman filter [2], in the 1970s marked a significant improvement in tracking accuracy. However, as tracking scenarios became more non-linear and non-Gaussian, traditional methods revealed limitations, prompting a transition to data-driven approaches.

By the early 2000s, MTT entered an era of a data-driven innovation. Particle filters [3] gained popularity for their ability to handle nonlinear and non-Gaussian scenarios, albeit with increased computational complexity. Concurrently, the attention was directed towards an efficient data association, leading to the development of filters such as the Joint Probabilistic Data Association (JPDA) [4] and Random Finite Set (RFS) [5] based methods.

Today, the landscape of MTT algorithms is characterized by diversity, with approaches tailored to specific tracking challenges. Two main categories dominate: association-

based methods and RFS-based methods.

Association-based methods focus on linking measurements to existing tracks or creating new tracks. This category includes well-established algorithms such as the Kalman filter and its variants (Extended Kalman Filter [6], Unscented Kalman Filter [7]), as well as more advanced methods like the Joint Probabilistic Association (JPDA) filter and the Multiple Hypothesis Tracker (MHT) [8], which address clutter and uncertainty in tracking scenarios.

In contrast, RFS-based methods offer a probabilistic framework to simultaneously model multiple target states. Operating on sets of possible target states, these methods provide a comprehensive representation of uncertainty and variability in tracking scenarios. Examples include the Probability Hypothesis Density (PHD) filter [9], Cardinalized Probability Hypothesis Density (CPHD) filter [10], and Poisson multi-Bernoulli mixture (PMBM) filter [11], which offer scalability and flexibility in complex tracking environments.

The future of MTT lies in the synergistic integration of association-based and RFS-based methods to overcome current challenges and address emerging needs in real-world tracking applications. By leveraging the strengths of both paradigms, researchers aim to achieve breakthroughs in tracking accuracy, efficiency, and scalability, paving the way for transformative advancements in multi-target tracking technology.

## 1.2 Applications of multi-target tracking

The versatility of MTT is reflected in its diverse applications across various domains. In defense, MTT plays a pivotal role in monitoring and tracking multiple targets simultaneously, aiding in threat assessment, target prioritization, and distinguishing between different targets.

The advent of autonomous systems, particularly in vehicles, has heightened the importance of MTT in predicting and tracking the movements of pedestrians, vehicles, and other obstacles. This application enhances the safety and efficiency of autonomous vehicles by providing a real-time awareness of the surrounding environment [12].

Surveillance systems rely on multi-target tracking for monitoring activities in crowded environments and identifying suspicious behavior.

Moreover, in fields such as robotics, defense, healthcare monitoring, and wildlife preservation, multi-target tracking systems contribute significantly to the enhancement of situational awareness, enabling a real-time decision-making, which improves resource allocation efficiency and supports various mission-critical tasks.

## 1.3 Research interests

Contemporary research in multi-target tracking is characterized by a strong emphasis on addressing key challenges to further enhance the performance and robustness of tracking systems. Current research focus is on problems such as:

- **Data Association in complex environment:** Handling scenarios with high target density, occlusions, and clutter remains a complex issue. Robust methods for accurate

and efficient data association in crowded and dynamic environments are still actively researched.

- **Handling non-linear and non-Gaussian dynamics:** Real-world scenarios often exhibit non-linear and non-Gaussian characteristics. Improving the tracking algorithms to effectively handle these complexities, possibly through the integration of advanced probabilistic models, is an ongoing area of research.
- **Real-time processing and computational efficiency:** Many MTT algorithms, especially those with high computational demands, face challenges in meeting real-time processing requirements. Efficient algorithms that strike a balance between computational complexity and tracking accuracy are continuously sought.
- **Sensor fusion and heterogeneous data integration:** Integrating information from various sensors, each with its own characteristics and limitations, remains a persistent challenge. Developing robust methods for sensor fusion to improve tracking accuracy and reliability is an active research area.
- **Handling variability in target behavior:** Targets in real-world scenarios may exhibit diverse and unpredictable behaviors. Adapting tracking algorithms to handle varying target speeds, accelerations, and maneuvers remains an unsolved problem.
- **Online learning and adaptive algorithms:** Designing algorithms that can adapt and learn online as they encounter new scenarios or dynamic changes in the environment is a topical issue. Adaptive tracking systems that can continuously improve their performance without extensive retraining are sought after.

As we will see later in this work, all Gaussian filters that take clutter into consideration rely on an accurate setting of a motion model or a measurement model. Moreover, recursion requires an estimation of parameters such as the survival probability and the detection probability. This thesis focuses on tracking targets in video data and takes advantage of image processing model YOLO (You Only Look Once) [13]. Due to this combination, we are able to estimate the detection probability in time and enhance the tracking capability of the filter.

The probabilistic formulation of the RFS-based filters and the inherent Bayesian processing of available information allow to accommodate the uncertainty arising from the presence of false detections, missed detections, and data association ambiguities. Nevertheless, a fundamental challenge persists: The performance of the filters is highly sensitive to the accurate setting of the target detection probability. This quantity, representing the likelihood of correctly identifying and associating observations with actual targets, is a critical parameter. It has a substantial impact on the Bayesian updating of the prior information. However, in real-world scenarios, the sensor performance is susceptible to various environmental conditions. Adverse weather, occlusions, or just the nature of the current scenario can lead to variations in detection probabilities. A mismatch between assumed and actual detection probabilities can result in a suboptimal tracking performance, leading to missed detections, false alarms, or inaccurate target state estimates [14].

The RFS-based formulation of the PHD or (P)MBM filters naturally takes the uncertainty about the detection probability into account [14]. The update formulas involve it as a function of the target state. In the figurative sense, this allows to model it as a function of the spatial and temporal properties of the environment. Still, two difficulties arise. First, the (Gaussian) filters are analytically tractable only if the detection probabilities are scalar numbers. Second, the nature of the detection probabilities differs from scenario to scenario.

In general, several methods have been proposed to deal with unknown detection probabilities. A Gaussian-beta modeling of a slowly-varying detection profile in the Cardinalized PHD filter is reported in [10]; its alternative for MBM filters follows in [15], and for PMBM filter in [16]. In [17], the authors propose to overcome some deficiencies in the CPHD filter [10] by different clutter/detection probability models. Another variant was recently proposed in [18]. A track-state augmentation with an amplitude offset-based prediction of the detection probability appeared in [19], however, this method suffers difficulties in multistatic fields. An automatic identification system-based sensor performance assessment for clutter-free environments is developed in [20]. A recent paper [21] deals with the unknown detection profile in the trajectory PHD/CPHD filters. There, the algorithm learns from the history of the unknown target detection probability.

As we track objects in video data, it allows us to avoid the generic solutions and focus on the peculiarities associated with this specific data type. In particular, an advantage of YOLO is taken, offering a high-performance real-time object detection with high accuracy and efficiency [13]. Its ability to simultaneously predict multiple bounding boxes and class probabilities within an image is used, providing a streamlined and efficient approach to object detection. However, YOLO-based multi-target tracking systems can still be compromised under conditions such as adverse weather, low lighting, or in scenarios with occlusions. Sensors may encounter difficulties in accurately detecting and localizing targets, leading to gaps or errors in the tracking process.

## 1.4 Structure

The structure of this thesis is as follows:

**Chapter 2** provides the theoretical background necessary for understanding the multi-target problem. This chapter follows up Bayesian inference, multivariate Gaussian distributions, mixtures, and state-space models. Next follows the intersection of discussed concepts and linking them in the possibilities of use in the form of a Kalman filter.

**Chapter 3** is dedicated to the target tracking problem itself. In this part, we explain terms as clutter or validation region and baseline formulations for single target tracking are presented. Next comes the overview of RFS-based methods and, especially, an explanation of the PHD filter and its recursion for linear Gaussian models.

**Chapter 4** discusses the topic of object detection and segmentation techniques algorithms with additional details dedicated to image processing models used in this work.

**Chapter 5** explains the problem of the dynamic detection probability in multi-target tracking. In this chapter, we propose a method to estimate the detection probability using deep-learning image processing models.

**Chapter 6** includes experiments that analyze the capability of the proposed method to estimate the detection probability.

## Chapter 2

# Theoretical Background

Multi-target tracking relies heavily on mathematical concepts from the probability theory, statistics, and linear algebra to model and infer the state of multiple objects over time. The key mathematical concepts involved in MTT include Bayesian inference, which provides a framework for updating estimates based on observed evidence, and the use of probabilistic models such as the Gaussian distribution and its extensions, such as Gaussian mixture models. In addition, MTT commonly employs state space models to represent the dynamics of object motion, with popular models including the constant velocity and constant acceleration models. These models are integrated into Bayesian filters, such as the Kalman filter, which recursively estimate the state of a target given by noisy measurements.

### 2.1 Bayesian inference

Bayesian inference stands as a foundational pillar within the realm of a probabilistic reasoning, offering a fundamental methodology for systematically updating beliefs in response to observed evidence. A fundamental theorem in probability theory, the Bayes' rule, is rooted in the Bayesian inference. It formalizes the process of revising prior beliefs in light of new data. The essence of Bayesian inference transcends mere statistical calculations; it embodies a philosophical stance towards uncertainty, emphasizing the incorporation of prior knowledge and the iterative refinement of beliefs through the assimilation of empirical observations. Within the context of multi-target tracking, Bayesian inference plays a paramount role, providing a principled framework for joining information from disparate sources, such as sensor measurements, historical data, and domain expertise. By embracing Bayesian principles, MTT algorithms gain the capacity to model and quantify uncertainty inherent in tracking scenarios, thereby fostering robustness and adaptability in the face of dynamic and complex environments. Moreover, Bayesian inference empowers MTT systems to exploit contextual cues and domain-specific knowledge, enhancing their ability to discern meaningful patterns among noise and uncertainty. Due to the Bayesian inference, MTT researchers and practitioners are equipped with a powerful tool to help encounter the intricacies of multi-target tracking, facilitating informed decision-making, and advancing the frontier of robust sys-

tems. Thus, Bayesian inference emerges not merely as a mathematical construct, but as a guiding philosophy underpinning the quest for understanding and reasoning in the face of uncertainty.

## 2.2 Bayes' rule

Bayes' rule, a cornerstone of Bayesian inference, embodies a fundamental principle in probability theory that underpins the systematic revision of beliefs in the face of new evidence. Mathematically expressed as a simple formula, Bayes' rule encapsulates the process of updating prior probabilities based on observed data, thereby yielding posterior probabilities that reflect the incorporation of new information. At its basis, the Bayes' rule provides a formal mechanism for quantifying the impact of new evidence on the likelihood of various hypotheses or states of nature. The rule states that the posterior probability of a hypothesis given observed data is proportional to the product of the likelihood of the data given the hypothesis and the prior probability of the hypothesis, divided by the marginal likelihood of the data. In essence, Bayes' rule facilitates a principled approach to inference, allowing practitioners to integrate prior knowledge with empirical observations to arrive to more informed and reliable conclusions. In the context of multi-target tracking, Bayes' rule serves as the base upon which the tracking algorithms are built, enabling the continuous refinement of estimates about the state of multiple targets based on sensor measurements and historical data. By adhering to the principles of Bayes' rule, MTT systems can effectively navigate the inherent uncertainty and complexity of tracking scenarios, thereby enhancing their robustness and accuracy.

► **Definition 2.1** (Conditional distribution). *Let  $X$  and  $Y$  be jointly continuous random variables,  $f_Y$  continuous at  $y$  and  $f_Y(y) > 0$ . Then, the conditional distribution function of  $X$ , given condition  $Y = y$  is defined by*

$$F_{X|Y}(x|y) := \lim_{\epsilon \rightarrow 0} P\{X \leq x | Y \in (y, y + \epsilon)\} = \frac{\partial F(x, y)/\partial y}{f_Y(y)}. \quad (2.1)$$

Differentiating this, the conditional density function of  $X$ , given the condition  $Y = y$ , is

$$f_{X|Y}(x|y) := \frac{\frac{\partial^2 F(x, y)}{\partial x \partial y}}{f_Y(y)} = \frac{f(x, y)}{f_Y(y)}. \quad (2.2)$$

Naturally, fixing  $y$ ,  $F_{X|Y}(\cdot|y)$  and  $f_{X|Y}(\cdot|y)$  are proper distribution and density functions, respectively. It is also clear that  $X$  and  $Y$  are independent if and only if  $F_{X|Y}(x|y) = F_X(x)$  and  $f_{X|Y}(x|y) = f_X(x)$  for all  $x$  and  $y$  for which these quantities are defined.

► **Definition 2.2** (Bayes' theorem). *Let  $x$  and  $y$  be random variables with densities  $f(x)$  and  $f(y)$ , respectively. Then Bayes' theorem is defined as*

$$f(x|y) = \frac{f(y|x)f(x)}{f(y)}, \quad f(y) > 0, \quad (2.3)$$

where

- $f(x|y)$  is the conditional posterior density of  $x$ ,
- $f(x)$  is the prior density,
- $f(y|x)$  is the likelihood and  $f(x)$  is the marginal density of  $X$ , also called *evidence*, and is given by

$$f(y) = \int f(x, y) dx. \quad (2.4)$$

Combining Equations (2.1), (2.2) and (2.4) to Formula (2.3) we get complete formula for Bayes' theorem

$$f(x|y) = \frac{f(y|x)f(x)}{f(y)} = \frac{f(y|x)f(x)}{\int f(y|x)f(x)dx}. \quad (2.5)$$

Since the denominator is the normalizing constant independent of  $x$ , often only proportionality is used

$$f(x|y) \propto f(y|x)f(x). \quad (2.6)$$

## 2.3 Multivariate Gaussian distribution

In the realm of multi-target tracking, various probability distributions are employed to model the uncertainty associated with target states and measurements. However, among these distributions, the multivariate Gaussian distribution holds a preeminent position due to its versatility, mathematical tractability, and empirical relevance. While other distributions may capture specific aspects of target behavior or measurement noise, the Gaussian distribution emerges as the cornerstone of MTT due to its ability to characterize complex probability distributions in multi-dimensional spaces. As a result, the common assumption among MTT filters is that the targets follow linear Gaussian dynamics and measurement models, as in [1], [9], or [11]. The Gaussian distribution finds ubiquitous application across various components of tracking algorithms, including

- **State representation:** Gaussian distributions are used to model the probability distributions of target states, allowing for efficient representation and propagation of uncertainty over time.
- **Measurement model:** Gaussian distributions are employed to model the likelihood of sensor measurements given the true target state, facilitating the incorporation of sensor data into the tracking process.
- **Filtering algorithms:** Gaussian-based filters leverage the Gaussian assumption to derive recursive estimation algorithms for tracking multiple targets with optimal efficiency and accuracy.
- **Data association:** Gaussian mixture models (GMMs), which represent mixtures of Gaussian distributions, are utilized for probabilistic data association in MTT, enabling robust handling of measurement uncertainty and target ambiguity.

► **Note 2.3.** The multivariate Gaussian distribution is a generalization of the univariate Gaussian distribution, but instead of a scalar mean and variance, there is a mean vector and a covariance matrix, that describe correlations between variables. The distribution of a  $k$ -dimensional random vector  $X = (X_1, \dots, X_k)^T$  can be written in the notation

$$X \sim \mathcal{N}(\mu, \Sigma),$$

with  $k$ -dimensional mean vector  $\mu = \mathbb{E}[X] = (\mathbb{E}[X_1], \mathbb{E}[X_2], \dots, \mathbb{E}[X_k])^T$  and  $k \times k$  positive semi-definite covariance matrix  $\Sigma$  with elements

$$\Sigma_{ij} = \mathbb{E}[(X_i - \mu_i)(X_j - \mu_j)] = \text{Cov}[X_i, X_j]. \quad (2.7)$$

The probability density function (PDF) is given by formula

$$\mathcal{N}(x; \mu, \Sigma) = \frac{1}{\sqrt{(2\pi)^k |\Sigma|}} \exp\left(-\frac{1}{2}(x - \mu)^T \Sigma^{-1} (x - \mu)\right), \quad (2.8)$$

where  $k$  is the length of the vector  $x$  and  $|\cdot|$  denotes the determinant of a matrix. It should be noted that the exponent is known as the Mahalanobis distance.

► **Definition 2.4** (Mahalanobis distance). *For vectors  $x \in R^n$  and  $y \in R^n$  and a positive semi-definite  $n \times n$  matrix  $S$ , their Mahalanobis distance is defined as*

$$d(x, y) = \sqrt{(x - y)^T S^{-1} (x - y)}. \quad (2.9)$$

The Mahalanobis distance (MD) is the distance between two points in an  $n$ -dimensional space and, unlike the Euclidean distance, it measures distances even between the correlated points for multiple variables.

Target tracking filters regularly use conditional probabilities and joint distributions, especially Gaussian.

► **Theorem 2.5** (Conditional joint Gaussian distribution). *Let  $x$  and  $y$  are Gaussian random variables with distributions  $\mathcal{N}(x; \mu_x, \Sigma_{xx})$  and  $\mathcal{N}(y; \mu_y, \Sigma_y)$ , respectively. Let their joint probability be given by*

$$p(x, y) = \mathcal{N}\left(\begin{bmatrix} x \\ y \end{bmatrix}; \begin{bmatrix} \mu_x \\ \mu_y \end{bmatrix}, \begin{bmatrix} \Sigma_{xx} & \Sigma_{xy} \\ \Sigma_{yx} & \Sigma_{yy} \end{bmatrix}\right). \quad (2.10)$$

*Then, the conditional distribution of  $x$  given  $y$  is defined as*

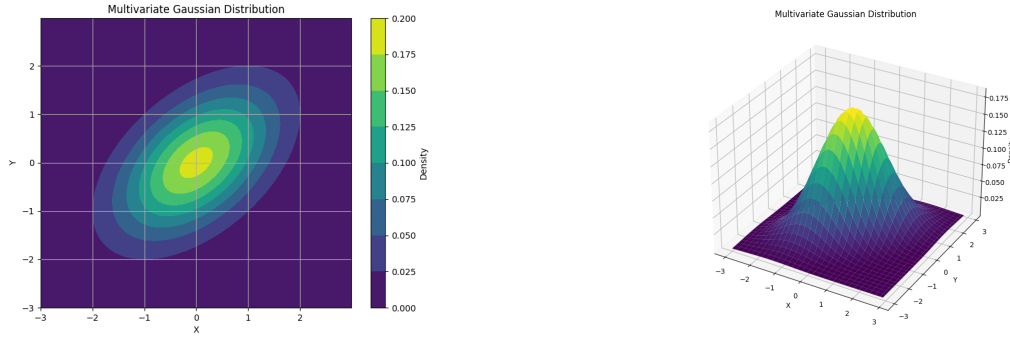
$$p(x|y) = \mathcal{N}(x; \mu_{x|y}, \Sigma_{x|y}), \quad (2.11)$$

*where*

$$\mu_{x|y} = \mu_x + \Sigma_{xy} \Sigma_{yy}^{-1} (y - \mu_y), \quad (2.12)$$

$$\Sigma_{x|y} = \Sigma_{xx} - \Sigma_{xy} \Sigma_{yy}^{-1} \Sigma_{yx}. \quad (2.13)$$

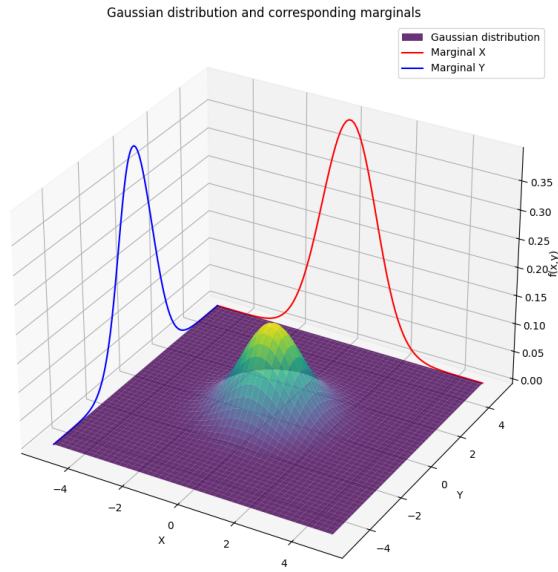
Examples of a multivariate Gaussian distribution are shown in Figure 2.1 and marginal distributions for multivariate Gaussian distribution can be found in Figure 2.2.



**(a)** Example of multivariate Gaussian distribution - contour plot.

**(b)** Example of multivariate Gaussian distribution - 3D plot.

■ **Figure 2.1** Examples of plots of multivariate Gaussian distribution.



■ **Figure 2.2** Gaussian distribution with corresponding marginals.

## 2.4 Gaussian mixture

Gaussian mixture models offer a flexible and powerful framework for representing complex probability distributions by combining multiple Gaussian components. In the Gaussian mixture model, a vector of parameters (e.g., observations of a signal) is modeled using a mixture distribution comprising several Gaussian components.

$$p(\Theta) = \sum_{i=1}^k w_i \mathcal{N}(\mu_i, \Sigma_i), \quad (2.14)$$

where the  $i^{th}$  component is characterized by Gaussian distribution with weight  $w_i$ , mean  $\mu_i$  and covariance matrix  $\Sigma_i$ . These parameters are encapsulated to the parameter  $\Theta$  in  $p(\cdot)$ .

In the context of multi-target tracking, Gaussian mixture models find utility in capturing the complex nature of target states and measurements. MTT often involves dealing with linear Gaussian models, where the posterior density is represented as a mixture of one or more Gaussian components. This representation enables MTT algorithms to probabilistically model the uncertainties associated with target dynamics, sensor measurements, and data association.

The probability density function (pdf) of a Gaussian mixture distribution is a weighted sum of each Gaussian component, expressed as

$$p(x) = \sum_{i=1}^k w_i \mathcal{N}(x; \mu_i, \Sigma_i), \quad (2.15)$$

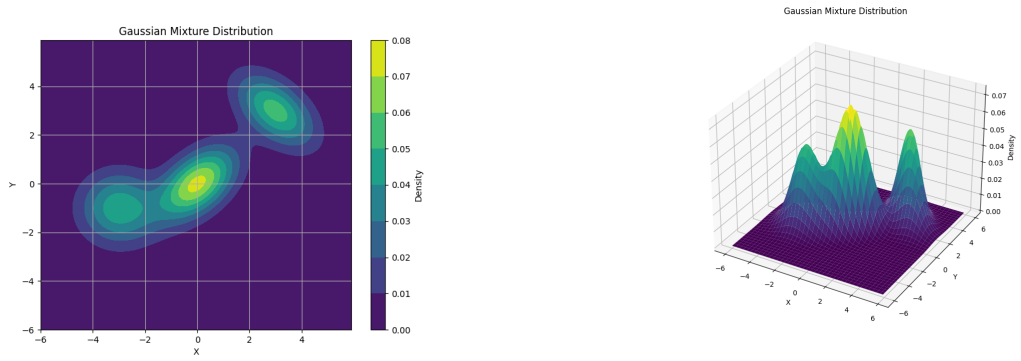
where  $k$  is the number of Gaussian components,  $w_i > 0$  is the weight of  $i^{th}$  component and  $\sum_{i=1}^k w_i = 1$ . Gaussian mixture models in multi-target algorithms are represented as intensity functions, i.e., components' weights do not have to sum to 1.

In MTT, Gaussian mixture models are particularly useful for tasks such as data association, where they probabilistically assign measurements to existing tracks or create new tracks based on the likelihood of observations given the target states. By modeling complex distributions of target states and measurements, Gaussian mixture models enable the MTT algorithms to handle uncertainties and ambiguities inherent in real-world tracking scenarios, including occlusions, clutter, and target interactions.

Examples of multivariate Gaussian mixture distribution are shown in Figure 2.3. Gaussian mixture distribution with marginal distribution for each dimension in Figure 2.4.

## 2.5 State-space model

State-space models serve as a fundamental framework for describing the evolution of dynamic systems over time. In the context of multi-target tracking, state-space models provide a formalism for representing motion dynamics of targets and the measurement process, enabling an efficient and accurate inference of target states from sensor data.



**(a)** Example of multivariate Gaussian mixture distribution - contour plot.

**(b)** Example of multivariate Gaussian mixture distribution - 3D plot.

**Figure 2.3** Examples of plots of multivariate Gaussian mixture distribution. There are three components in figures with means  $\{[0, 0], [3, 3], [-3, -1]\}$ . Note that the density of peaks is very low, because the sum has to be equal 1.

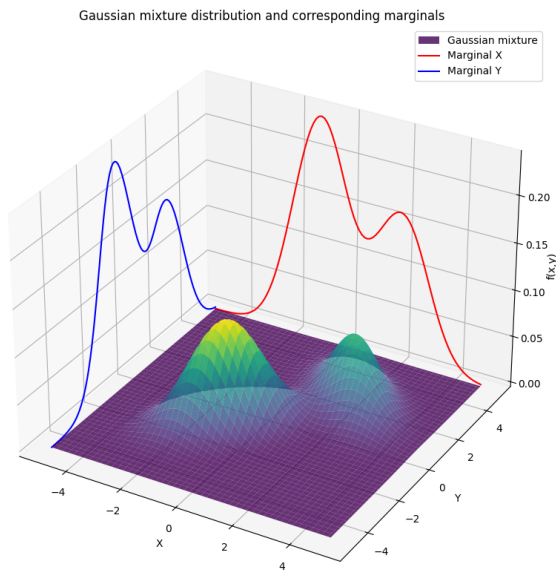


**Figure 2.4** Gaussian mixture distribution with means  $\{[0, 0], [2, 2]\}$ , weights  $\{[0.6, 0.4]\}$  and corresponding marginals.

At the core of a state-space model lies a set of latent variables, known as the state vector, which encapsulates the unobservable quantities of interest, such as the position, velocity, and acceleration of targets in MTT. The dynamics governing the evolution of the state vector are typically described by a transition model, which specifies how the state evolves over time according to a probabilistic process. This transition model can take various forms depending on the nature of the system dynamics, ranging from simple linear or non-linear models to more complex stochastic processes.

In addition to the transition model, state-space models incorporate an observation model that describes the relationship between the observed measurements and the underlying state variables. This observation model accounts for the uncertainties and noise inherent in the measurement process, allowing for the probabilistic mapping of observed data to the latent state space.

State-space model can be represented as a pair of stochastic equations.

### 1. State transition equation:

$$x_k = f(x_{k-1}, u_k, w_k), \quad (2.16)$$

where  $x_k$  represents the state vector at time  $k$ ,  $f$  denotes the transition function describing the evolution of the state,  $u_k$  represents optional control inputs, and  $w_k$  denotes process noise.

### 2. Observation equation:

$$z_k = h(x_k, v_k), \quad (2.17)$$

where  $z_k$  represents the observed measurements at time  $k$ ,  $h$  denotes the observation function mapping the state to measurements, and  $v_k$  represents the measurement noise.

In MTT, state-space models provide a natural framework for representing the motion dynamics of multiple targets and the sensor measurements associated with each target. Each target is typically associated with its own state vector, enabling simultaneous tracking of multiple objects within the same probabilistic framework.

State-space models enable MTT algorithms to perform a range of tasks, including target prediction, data association, and state estimation by propagating the state forward in time using the transition model and updating the state based on observed measurements using the observation model. By incorporating uncertainty explicitly into the tracking process, state-space models facilitate robust inference of target states in complex and dynamic tracking scenarios.

While state-space models offer a powerful framework for multi-target tracking, they also present several challenges.

- **Model complexity:** Designing an appropriate state-space model requires careful consideration of the underlying dynamics and measurement process, which can be challenging in complex tracking scenarios with non-linearities and uncertainties.
- **Parameter estimation:** Estimating the parameters of a state-space model from data, such as the transition and observation matrices, can be computationally demanding and prone to issues such as overfitting or underfitting.

- **Computational Complexity:** Performing inference in state-space models often involves recursive algorithms such as the Kalman filter or the particle filter, which can be computationally intensive, especially in high-dimensional or real-time tracking applications.

Despite these challenges, state-space models remain a foundation of multi-target tracking, offering a principled and flexible framework for representing and reasoning about dynamic systems in the presence of uncertainty. There are many state space models used in MTT. Before we define the two of the most common ones in the forthcoming sections, it should be noted, that the definitions in (2.16) and (2.17) are too general, because  $f_k$  and  $h_k$  could be any functions.

To get a closed-form solution in the Bayesian inference framework, we need to choose conjugate distributions for the likelihood and the prior. The Kalman filter (see Section 2.8 for more) works for the Gaussian-linear case, where the functions  $f_t$  and  $h_t$  represent linear and noisy variables and are distributed as Gaussians with zero mean. The Gaussian linear state-space model has the formulation:

$$p(x_k|x_{k-1}) = Fx_{k-1} + Bu_k + w_k \quad w_k \sim \mathcal{N}(0, Q), \quad (2.18)$$

$$p(z_k|x_k) = Hx_k + v_k \quad v_k \sim \mathcal{N}(0, R), \quad (2.19)$$

$$p(x_0) \sim \mathcal{N}(\hat{x}_0, P_0), \quad (2.20)$$

where

- $F$  is the transition matrix of appropriate dimension,
- $B$  is the input matrix of appropriate dimension,
- $H$  is the measurement matrix of appropriate dimension,
- $Q$  is the symmetric positive semi-definite covariance matrix of motion noise  $w_k$ ,
- $R$  is the symmetric positive semi-definite covariance matrix of measurement noise  $v_k$ ,
- $\hat{x}_0$  and  $P_0$  are the mean and the covariance matrix of the prior state.

The control variable  $u_k$ , in general, represents some input signal from the environment, and  $B$  specifies how the input signal affects the dynamic system. This variable is usually not considered in MTT scenarios. In multi-target tracking, Gaussian linear models are most often worked with, thus following formulation is used instead:

$$p(x_k|x_{k-1}) = \mathcal{N}(x_k; Fx_{k-1}, Q), \quad (2.21)$$

$$p(z_k|x_k) = \mathcal{N}(z_k; Hx_k, R), \quad (2.22)$$

$$p(x_0) \sim \mathcal{N}(x_0; \hat{x}_0, P_0). \quad (2.23)$$

### 2.5.1 Constant velocity model

The constant velocity model (CVM) is a fundamental component of multi-target tracking systems, providing a simplified yet effective representation of target motion dynamics

over time. This model assumes that the target's velocity remains constant between consecutive time steps, making it particularly suitable for tracking objects with relatively smooth and predictable motion patterns. In this section, we explore the conceptual basis, mathematical formulation, and practical implications of the constant velocity model in the context of MTT.

At its core, the constant velocity model embodies the notion of inertia, where a target maintains a constant velocity unless acted upon by external forces. This conceptual simplicity allows for a straightforward representation of target motion, making the constant velocity model a popular choice for MTT applications where targets exhibit relatively uniform and predictable movement behaviors.

Mathematically, the constant velocity model describes the evolution of a target's state vector over time in terms of its position and velocity. At each time step  $k$ , the state vector  $x_k$  comprised from the position  $[x_{1,k}, x_{2,k}]^T$  and the velocity  $s$  of the target, is decomposed as follows,

$$x_k = [x_{1,k}, x_{2,k}, s_{1,k}, s_{2,k}]^T. \quad (2.24)$$

The dynamics of the constant velocity model can be represented using a state transition matrix  $F$  and a process noise vector  $w_k$ , where the state transition matrix captures the relationship between the target's state at consecutive time steps

$$x_{k+1} = Fx_k + w_k. \quad (2.25)$$

All together, vector  $x_k$ , matrices  $F$  and  $Q$ , might, for example, be represented as

$$x_k = \begin{bmatrix} x_{1,k} \\ x_{2,k} \\ s_{1,k} \\ s_{2,k} \end{bmatrix}, \quad F = \begin{bmatrix} 1 & 0 & \Delta & 0 \\ 0 & 1 & 0 & \Delta \\ 0 & 0 & 1 & 0 \\ 0 & 0 & 0 & 1 \end{bmatrix}, \quad Q = q^2 \begin{bmatrix} \frac{\Delta^3}{3} & 0 & \frac{\Delta^2}{2} & 0 \\ 0 & \frac{\Delta^3}{3} & 0 & \frac{\Delta^2}{2} \\ \frac{\Delta^2}{2} & 0 & \Delta & 0 \\ 0 & \frac{\Delta^2}{2} & 0 & \Delta \end{bmatrix}, \quad (2.26)$$

where  $\Delta$  stands for delta time, i.e., elapsed time between the last estimation and the current one.  $q$  is the motion noise parameter, which represents the uncertainty in the state transition. The measurement model transforms a state vector from the state-space into the measurement space. Since the filters derived from the Kalman filter assume only linear models, the measurement model for CVM assumes the same space as in the state vectors. As a result, the observation matrix  $H$  and the noise matrix  $R$  can be, with respect to (2.26), formulated

$$H = \begin{bmatrix} 1 & 0 & 0 & 0 \\ 0 & 1 & 0 & 0 \end{bmatrix}, \quad R = r^2 \begin{bmatrix} 1 & 0 \\ 0 & 1 \end{bmatrix}, \quad (2.27)$$

where  $r$  determines the variance of the measurement noise.

To obtain optimal results given by filters, it is essential to set parameters  $r$  and  $q$  appropriately. There are three main possible procedures. The first one requires the knowledge of motion noise given by tracked object and the knowledge of sensor's error when detecting targets, i.e. the noisy measurement. This method is often used in simulations and experiments. The second one is a simple trial and error method with reasonable choices. The last one is using automated methods, like in [22].

By assuming the constant velocity, MTT algorithms can predict the future positions of targets based on their current state and velocity, facilitating trajectory estimation and target prediction.

One common application of the constant velocity model in MTT is in the design of prediction algorithms, where future positions of targets are estimated based on their current state and velocity information. These predictions are essential for anticipating target movements and facilitating data association, enabling the MTT algorithms to maintain track continuity and adapt to changes in the target behavior over time.

Moreover, the constant velocity model can be seamlessly integrated into recursive Bayesian filters, such as the Kalman filter, for state estimation in MTT. By incorporating the constant velocity model into the state-space representation of the tracking problem, Kalman filter-based algorithms can effectively fuse measurement information with dynamic predictions to estimate the most likely trajectories of targets over time.

## 2.5.2 Constant acceleration model

The constant acceleration model (CAM) stands as a sophisticated extension of the state-space model in multi-target tracking, offering a more detailed representation of target motion dynamics. Unlike simpler models such as the constant velocity model, which assumes a constant velocity for targets over time, the CAM acknowledges the potential for changes in target acceleration, allowing for more accurate and flexible trajectory estimation. This section delves into the conceptual basis, mathematical formulation, and practical implications of the constant acceleration model in the context of MTT.

In MTT scenarios, targets often exhibit varying degrees of acceleration due to factors such as changes in speed, direction, or environmental influences. Ignoring these accelerative effects can lead to biased trajectory estimates and diminished tracking accuracy. The CAM addresses this limitation by incorporating an additional acceleration component into the state-space model, enabling more faithful representation of target motion dynamics. By accounting for changes in acceleration, the CAM provides MTT algorithms with a greater flexibility and adaptability in tracking targets with non-uniform motion profiles.

Mathematically, the constant acceleration model extends the state transition function of the state-space model to accommodate changes in acceleration over time. At each time step  $k$ , the evolution of the target's state vector  $x_k$  is governed by a set of dynamic equations that describe the position, velocity, and acceleration of the target

$$x_k = [x_{1,k}, x_{2,k}, s_{1,k}, s_{2,k}, a_{1,k}, a_{2,k}]^T, \quad (2.28)$$

where, as in CVM,  $x_{1,k}$ ,  $x_{2,k}$  is the position of an target in two-dimensional space,  $s_{1,k}$ ,  $s_{2,k}$  is the velocity and  $a_{1,k}$ ,  $a_{2,k}$  are the accelerations in both directions. Matrices

$F$  and  $Q$  can then be expressed

$$x_k = \begin{bmatrix} x_{1,k} \\ x_{2,k} \\ s_{1,k} \\ s_{2,k} \\ a_{1,k} \\ a_{2,k} \end{bmatrix}, \quad F = \begin{bmatrix} 1 & 0 & \Delta & 0 & \frac{1}{2}\Delta^2 & 0 \\ 0 & 1 & 0 & \Delta & 0 & \frac{1}{2}\Delta^2 \\ 0 & 0 & 1 & 0 & 0 & 0 \\ 0 & 0 & 0 & 1 & 0 & 0 \\ 0 & 0 & 0 & 0 & 1 & 0 \\ 0 & 0 & 0 & 0 & 0 & 1 \end{bmatrix}, \quad Q = q^2 \begin{bmatrix} \frac{\Delta^4}{4} & 0 & \frac{\Delta^3}{3} & 0 & \frac{\Delta^2}{2} & 0 \\ 0 & \frac{\Delta^4}{4} & 0 & \frac{\Delta^3}{3} & 0 & \frac{\Delta^2}{2} \\ \frac{\Delta^3}{3} & 0 & \frac{\Delta^2}{2} & 0 & \frac{\Delta^2}{2} & 0 \\ 0 & \frac{\Delta^3}{3} & 0 & \frac{\Delta^2}{2} & 0 & \frac{\Delta^2}{2} \\ \frac{\Delta^2}{2} & 0 & \frac{\Delta^2}{2} & 0 & \Delta & 0 \\ 0 & \frac{\Delta^2}{2} & 0 & \frac{\Delta^2}{2} & 0 & \Delta \end{bmatrix}. \quad (2.29)$$

The measurement model remains unchanged from the standard state-space model, relating the observed measurements  $z_k$  to the target's true state  $x_k$  through a measurement function  $h(\cdot)$  corrupted by measurement noise  $v_t$

$$H = \begin{bmatrix} 1 & 0 & 0 & 0 & 0 & 0 \\ 0 & 1 & 0 & 0 & 0 & 0 \end{bmatrix}, \quad R = r^2 \begin{bmatrix} 1 & 0 \\ 0 & 1 \end{bmatrix}, \quad (2.30)$$

The constant acceleration model offers several practical advantages in MTT applications:

- **Improved trajectory estimation:** By accounting for changes in acceleration, the CAM enables a more accurate and realistic trajectory estimation, particularly for targets exhibiting non-uniform motion patterns or sudden changes in velocity.
- **Enhanced predictive capability:** The inclusion of acceleration dynamics allows MTT algorithms to make more informed predictions about future target states, improving the tracking performance and reducing prediction errors.
- **Robustness to dynamic environments:** In dynamic environments with varying levels of congestion, obstacles, or traffic patterns, the CAM provides MTT algorithms with greater robustness and adaptability, enabling an effective tracking even in challenging scenarios.
- **Applications in autonomous systems:** In autonomous systems such as self-driving cars, drones, or robotics, the CAM plays a crucial role in motion planning, obstacle avoidance, and trajectory prediction, enhancing the safety and efficiency of an autonomous navigation.

In summary, the constant acceleration model represents a significant advancement in multi-target tracking, offering a more nuanced and comprehensive approach to modeling target motion dynamics. By incorporating acceleration effects into the tracking process, the CAM enables MTT algorithms to achieve higher accuracy, robustness, and predictive capability, making it an indispensable tool for a wide range of applications.

## 2.6 Hidden Markov Model

In the domain of multi-target tracking, the hidden Markov model (HMM) serves as a framework for capturing the temporal dynamics of target behavior in complex environments. Building upon the principles of Markov processes, the HMM extends the

state-space model by introducing hidden states that govern the evolution of observable measurements over time. Markov process of the first order is a model, in which current state depends only on the previous state

$$p(x_k|x_1, \dots, x_{k-2}, x_{k-1}, z_1, \dots, z_{k-2}, z_{k-1}) = p(x_k|x_{k-1}) \quad (\text{transition probability}), \quad (2.31)$$

$$p(z_k|x_1, \dots, x_{k-2}, x_{k-1}, x_k, z_1, \dots, z_{k-2}, z_{k-1}) = p(z_k|x_k) \quad (\text{observation likelihood}), \quad (2.32)$$

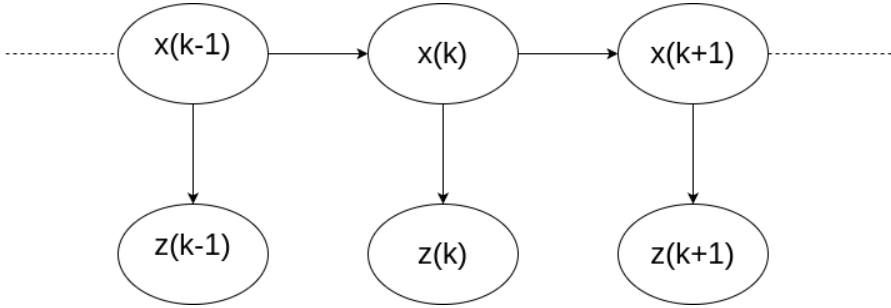
$$p(x_0) \quad (\text{initial state}). \quad (2.33)$$

In models of higher order, the transition probability is

$$p(x_k|x_{k-1}, \dots, x_{k-n}), \quad (2.34)$$

where  $n$  is the number of the order. Details of this model are not described in this work and can be found, e.g., in [23].

In cases where the process is not directly observable, but can be perceived through another observable variable  $z_k$ , we often talk about hidden Markov process.



■ **Figure 2.5** Demonstration of the course of the hidden Markov process.

At its base, the hidden Markov process represents a stochastic process characterized by a set of hidden states that transition probabilistically over time. While these hidden states are unobservable, they influence the generation of observable measurements, which are assumed to be conditionally independent given the hidden states. In the context of MTT, the hidden states may represent latent attributes of targets, such as their locations, velocities, or motion patterns, while the observable measurements correspond to sensor readings or detections obtained from surveillance systems.

## 2.7 Bayes' filter

The Bayes' filter leverages both the motion and the measurement model, operating under the assumption that these models accurately describe the system's behavior. Functioning within a recursive framework, the Bayes' filter continually estimates the internal state of the system over time using available measurements. Each iteration of the filter entails two fundamental steps: a prediction and an update. During the prediction step, the filter anticipates the internal state  $x_k$  based on the preceding state  $x_{k-1}$  and the motion model

$p(x_k|x_{k-1})$ . This prediction step is commonly referred to as the Chapman-Kolmogorov equation [24].

► **Theorem 2.6** (The Chapman-Kolmogorov equation-prediction step). *Given the set of measurements  $z_{0:k-1} = z_0, \dots, z_{k-1}$ , set of control variables  $u_{0:k-1} = u_0, \dots, u_{k-1}, u_k$ , the current state  $x_{k-1}$  and the motion model  $p(x_k|x_{k-1})$ , the prediction step is as follows:*

$$p(x_k|z_{0:t-1}, u_{0:k}) = \int p(x_k|x_{k-1}, u_k) p(x_{k-1}|z_{0:k-1}, u_{0:k-1}) dx_{k-1}, \quad (2.35)$$

where the integral is taken over the entire state space of  $x_{k-1}$ , and  $p(x_{k-1}|z_{0:k-1}, u_{0:k-1})$  is the posterior density of the state at time  $k - 1$ .

During the update step, the Bayes' filter corrects (updates) the prediction step with measurements  $z_k$  using the measurement model  $p(z_k|x_k)$ . This step employs common Bayes' rule.

► **Theorem 2.7** (The update step of Bayes' filter). *Given the output of Bayes' filter prediction step, the measurements  $z_k$  observed at time  $k$  and the measurement model  $p(z_k|x_k)$ , the update step of the Bayes' filter is formulated as follows:*

$$p(x_k|z_{0:t}, u_{0:t}) = \frac{p(z_k|x_k)p(x_k|z_{0:k-1}, u_{0:k})}{p(z_k|z_{0:k-1})} \propto p(z_k|x_k)p(x_k|z_{0:k-1}, u_{0:k}) \quad (2.36)$$

These two steps work in an iterative manner, where, in each iteration, the prediction step is used to predict the state  $x_k$  and then the update step is used to correct this prediction with the provided measurement  $z_k$ .

## 2.8 Kalman filter

The Kalman filter, named after its developer Rudolf E. Kalman, has a rich history dating back to the early 1960s when Kalman first introduced the algorithm in a series of landmark papers. Initially developed for aerospace applications, the Kalman filter gained prominence for its ability to provide an optimal state estimation in the presence of noisy measurements and uncertain dynamics.

Over the years, the Kalman filter has found widespread usage across diverse fields and industries, including aerospace, robotics, finance, and telecommunications. Its applications range from tracking spacecraft trajectories and guiding missiles to monitoring financial markets and controlling autonomous vehicles. The filter's versatility and efficiency have made it a cornerstone of modern estimation and control systems.

The Kalman filter operates on the principles of recursive Bayesian estimation, utilizing a system dynamics model and noisy measurements to predict and update the state of a dynamic system over time. Its mathematical elegance and simplicity make it well-suited for real-time applications, enabling an accurate and efficient state estimation even in complex and uncertain environments.

Despite its success, the Kalman filter continues to evolve, with extensions and variations such as the extended Kalman filter (EKF) [6] and unscented Kalman filter (UKF) [7] addressing more challenging scenarios involving non-linear dynamics and non-Gaussian noise.

In summary, the Kalman filter stands as a seminal contribution to the field of estimation and control, with a rich history of development and widespread usage across diverse domains. Its continued relevance and versatility underscore its status as a foundational tool for state estimation and tracking in modern technological applications.

### 2.8.1 Kalman filter inference

In Section 2.5 we talked about state-space model, which is used by the Kalman filter. Thus we work with equations

$$x_k = Fx_{k-1} + w_t \quad (2.37)$$

$$z_t = Hx_k + v_k, \quad (2.38)$$

where both noise variables are independent and with zero mean

$$w_k \sim \mathcal{N}(0, Q), \quad (2.39)$$

$$v_k \sim \mathcal{N}(0, R). \quad (2.40)$$

Then the state and measurement distributions follows

$$x_k \sim \mathcal{N}(Fx_{k-1}, Q) \quad \text{with density } p(x_k|x_{k-1}), \quad (2.41)$$

$$z_k \sim \mathcal{N}(Hx_k, R) \quad \text{with density } p(z_k|x_k). \quad (2.42)$$

Since the Kalman filter is Bayesian, we need a prior distribution for  $x_k$ . Model  $z_k$  is also Gaussian, thus the conjugate prior is then also a Gaussian with mean  $x_{k-1}^+$  and covariance matrix  $P_{k-1}^+$ ,

$$p(x_k|z_{0:k-1}) = \mathcal{N}(x_{k-1}^+, P_{k-1}^+). \quad (2.43)$$

The prediction step is derived from Formula (2.35). Note, that by multiplying two Gaussian distributions we again get the Gaussian distribution  $\mathcal{N}(x_k^-, P_k^-)$  with hyperparameters

$$x_k^- = Fx_{k-1}^+, \quad (2.44)$$

$$P_k^- = FP_{k-1}^+F^T + Q. \quad (2.45)$$

By multiplying two Gaussian distributions followed by marginalization, we enumerate the state equation. The estimation of state  $x_k^-$  is achieved by a substitution of model variables into appropriate equations. The estimated covariance  $P_k^-$  expresses the degree of uncertainty of the estimation. By applying this step, the uncertainty grows.

The update step corrects the prediction step by incorporating new observed measurements  $z_k$ . For that, formula (2.36) is used. The model is transformed into an exponential

form

$$\begin{aligned} p(z_k | x_k) &\propto \exp \left\{ -\frac{1}{2} (z_k - Hx_k)^T R^{-1} (z_k - Hx_k) \right\} \\ &= \exp \left\{ Tr \left( \underbrace{-\frac{1}{2} \begin{bmatrix} -1 \\ x_k \end{bmatrix} \begin{bmatrix} -1 \\ x_k \end{bmatrix}^T}_{\eta} \underbrace{\begin{bmatrix} z_k^T \\ H^T \end{bmatrix} R^{-1} \begin{bmatrix} z_k^T \\ H^T \end{bmatrix}^T}_{T(z_k)} \right) \right\}. \end{aligned} \quad (2.46)$$

The conjugate prior can be rewritten into a compatible form as follows:

$$\begin{aligned} p(x_k | z_{0:k-1}) &\propto \exp \left\{ -\frac{1}{2} (x_k - x_k^-)^T (P_k^-)^{-1} (x_k - x_k^-) \right\} \\ &= \exp \left\{ Tr \left( \underbrace{-\frac{1}{2} \begin{bmatrix} -1 \\ x_k \end{bmatrix} \begin{bmatrix} -1 \\ x_k \end{bmatrix}^T}_{\eta} \underbrace{\begin{bmatrix} (x_k^-)^T \\ I \end{bmatrix} (P_k^-)^{-1} \begin{bmatrix} (x_k^-)^T \\ I \end{bmatrix}^T}_{\xi_k} \right) \right\}, \end{aligned} \quad (2.47)$$

where  $I$  is an identity matrix of appropriate shape.

The Bayesian update is a sum of the hyperparameter and sufficient statistic,

$$\begin{aligned} \xi_k &= \xi_{k-1} + T(z_k) \\ &= \begin{bmatrix} (x_k^-)^T (P_k^-)^{-1} x_k^- + z_k^T R^{-1} z_k, & (x_k^-)^T (P_k^-)^{-1} + z_k^T R^{-1} H \\ (P_k^-)^{-1} (x_k^-)^T + H^T R^{-1} z_k, & (P_k^-)^{-1} + H^T R^{-1} H. \end{bmatrix} \end{aligned} \quad (2.48)$$

The posterior parameters are then derived

$$\begin{aligned} P_k^+ &= (\xi_{k;[2,2]})^{-1} \\ &= [(P_k^-)^{-1} + H^T R^{-1} H]^{-1} \\ &= (I - K_k H) P_k^- \end{aligned} \quad (2.49)$$

$$\begin{aligned} x_k^+ &= (\xi_{k;[2,2]})^{-1} \xi_{k;[2,1]} \\ &= P_k^+ [(P_k^-)^{-1} (x_k^-)^T + H^T R^{-1} z_k] \\ &= x_k^- + P_k^+ H^T R^{-1} (z_k - Hx_k^-), \end{aligned} \quad (2.50)$$

where

$$K_k = P_k^- H^T (R + H P_k^- H^T)^{-1} \quad (2.51)$$

is the Kalman gain. This form is the optimal Kalman gain, as it minimizes the root mean squared error. In general, the greater the gain, the greater the emphasis of the new measurements. The filter then becomes more sensitive.

There are several possible formulas that express the optimal Kalman filter. One of

the most popular formulations is as follows:

$$\hat{z}_k^- = H\hat{x}_k^-, \quad \text{(measurement prediction)} \quad (2.52)$$

$$v_t = z_t - \hat{z}_k^-, \quad \text{(innovation or prediction error } z_t) \quad (2.53)$$

$$S_t = HP_k^-H^T + R, \quad \text{(covariance of innovation } v_t) \quad (2.54)$$

$$K_t = P_k^-H^TS_t^{-1}, \quad \text{(Kalman gain)} \quad (2.55)$$

$$x_k^+ = \hat{x}_k^- + K_t v_t, \quad \text{(posterior state estimation } x_t) \quad (2.56)$$

$$P_k^+ = (I - K_t H)P_k^-. \quad \text{(posterior covariance)} \quad (2.57)$$

The pseudo-algorithm of the Kalman filter is shown in Algorithm 1.

---

**Algorithm 1** Kalman Filter Algorithm
 

---

```

1: Inputs: Initial state estimate  $\hat{x}_0$ , initial covariance matrix  $P_0$ , system dynamics matrix  $F$ , process
   noise covariance matrix  $Q$ , measurement matrix  $H$ , measurement noise covariance matrix  $R$ , and
   measurements  $Z$ .
2: Outputs: Updated state estimate  $\hat{x}_k$  and updated covariance matrix  $P_k$ .
3:
4: procedure INITIALIZATION( $x_0, P$ )
5:    $\hat{x}_0 = x_0$                                      ▷ Initialize state estimate
6:    $P_0 = P$                                      ▷ Initialize error covariance matrix
7: end procedure
8:
9: procedure PREDICTION STEP
10:   $\hat{x}_{k|k-1} = F\hat{x}_{k-1}$                       ▷ Predict state estimate
11:   $P_{k|k-1} = FP_{k-1}F^T + Q$                   ▷ Predict covariance:
12: end procedure
13:
14: procedure UPDATE STEP( $z_k$ )
15:   $K_k = P_{k|k-1}H^T(HP_{k|k-1}H^T + R)^{-1}$     ▷ Kalman gain
16:   $\hat{x}_k = \hat{x}_{k|k-1} + K_k(z_k - H\hat{x}_{k|k-1})$  ▷ Update state estimate
17:   $P_k = (I - K_k H)P_{k|k-1}$                     ▷ Update covariance
18: end procedure
19:
20: procedure KALMAN FILTER RECURSION
21:   Initialization
22:   for all  $z_k \in Z$  do
23:     Perform Prediction Step
24:     Perform Update Step with  $z_k$ 
25:   end for
26: end procedure
  
```

---

## Chapter 3

# Target tracking

Target tracking plays a pivotal role in surveillance systems, such as radars, where the primary objective is to estimate the trajectory, position, and other characteristics of moving objects within a surveillance area. Derived from the foundational principles of the Kalman filter, target tracking algorithms are tailored to the specific requirements and challenges inherent in radar applications.

Radar-based target tracking encounters various complexities, including survivability and the presence of multiple targets in the same area. Survivability concerns the algorithm's ability to maintain accurate estimates despite target maneuvers, occlusions, or potential target loss. Furthermore, the phenomenon of multiple targets in the same neighbourhood introduces significant ambiguities and challenges in trajectory estimation and association.

In the realm of single-target tracking, algorithms such as the Probabilistic Data Association (PDA) filter [25] and its derivatives, such as the Integrated Probabilistic Data Association (IPDA) filter [4] or multi-target tracking variation Joint Probabilistic Data Association (JPDA) filter [4], are commonly employed. These algorithms provide robust solutions for associating measurements with existing tracks and updating target state estimates in dynamic scenarios.

Beyond single-target tracking, radar systems often necessitate multi-target tracking approaches. These approaches, particularly those based on Random Finite Sets (RFS) [5], offer advanced capabilities for tracking multiple targets simultaneously. RFS-based filters, including the Probability Hypothesis Density (PHD) filter [9], and the Multi-Bernoulli Mixture (MBM) filter [11], excel in scenarios where the number of targets is uncertain or dynamic.

In this chapter, we delve into the intricacies of advanced target tracking algorithms and explore their theoretical foundations, practical implementations, and performance characteristics. By understanding the diverse range of available algorithms and their respective strengths, we can design and deploy effective systems to meet the demands of modern surveillance and applications.

### 3.1 Data association

Data association uncertainty arises in remote sensing systems, such as radar, sonar, or electro-optical devices, when measurements are obtained from sources that may not necessarily be the target of interest [25]. This uncertainty occurs particularly in situations where the target signal is weak, necessitating a lower detection threshold, which may result in the detection of background signals, sensor noise, or clutter. Additionally, data association uncertainty can occur when multiple targets are present in close proximity. Utilizing spurious measurements in a tracking filter can lead to divergence of the estimation error and, consequently, track loss.

Addressing this challenge involves two primary problems. The first is the selection of appropriate measurements to update the state of the target of interest in the tracking filter, which can be, e.g., a Kalman filter or an extended Kalman filter. The second problem involves determining whether the filter needs modifications to account for data association uncertainty. The objective is to obtain the minimum mean square error (MMSE) estimate of the target state and associated uncertainty.

The optimal estimator involves the recursive computation of the conditional probability density function of the state, with detailed conditions provided under which this pdf serves as a sufficient statistic in the presence of data association uncertainty.

### 3.2 Clutter

When it comes to clutter, two scenarios may occur. The first one is a single target in clutter. This problem of tracking a single target in clutter appears when several measurements appear in the validation region. The validated measurements comprise the accurate measurement, if detected within this region, along with spurious measurements originating from clutter or false alarms. For instance, in air traffic control systems, where cooperative targets are involved, each true target includes an identifier known as the squawk number. If this identifier is entirely reliable, data association uncertainty is eliminated. However, in cases where a potentially hostile target is non-cooperative, data association uncertainty becomes a significant challenge.

#### 3.2.1 Validation region

In target tracking scenarios, the process of signal detection provides measurements from which the appropriate ones for inclusion in the target state estimator are chosen. In radar systems, for instance, the signal reflected from the target of interest is sought within a specific time interval, determined by the expected range of the target when it reflects the transmitted energy. A range gate is established and detections falling within this gate can be associated with the target of interest. These measurements could include informations such as range, azimuth, elevation, or direction cosines. For a radar or an active sonar, we might also measure how fast something is moving towards or away from us. For a passive sonar, we might look at the direction somethings coming from, when it arrives, and the difference in sounds it makes. And for optical sensors, we might measure the angle it is seen from. By setting up a multidimensional gate, the signal

from the target is detected efficiently, avoiding the need to search for it across the entire measurement space.

However, while a measurement within the gate is a candidate for an association with the target, it is not guaranteed to have originated from the target itself. Thus, the establishment of a validation region becomes necessary. The validation region is designed to ensure that the target measurement falls within it with a high probability, known as the gate probability, based on the statistical characterization of the predicted measurement. In the event where more than one detection appears within the gate, association uncertainty arises. With this uncertainty, it is important to figure out which measurement really comes from the target and should be used to update our tracking information. This includes factors like the target's estimated position and its variability, or, more broadly, the key information we need about the target. Measurements outside the validation region can be disregarded, as they are too distant from the predicted measurement and are unlikely to have originated from the target of interest. This scenario typically arises when the gate probability is close to unity, and the statistical model used to define the gate is accurate.

Figure 3.1 illustrates a scenario that involves multiple validated measurements. The validation region depicted in the figure is two-dimensional and takes the form of an ellipse centered at the predicted measurement  $\hat{z}$ . The elliptical shape of the validation region arises from the assumption that the error in the target's predicted measurement, known as the innovation, follows a Gaussian distribution. The parameters defining the ellipse are determined by the covariance matrix  $S$  of the innovation.

All measurements within the validation region have the potential to originate from the target of interest. The key assumption here is that the true target generates at most one measurement per scan. As a result, the possible association events include:  $z_1$  originating from the target, with  $z_2$  and  $z_3$  being from clutter;  $z_2$  originating from the target, with  $z_1$  and  $z_3$  being from clutter;  $z_3$  originating from the target, with  $z_2$  and  $z_1$  being from clutter; or all measurements being from clutter. These association events are mutually exclusive and exhaustive, enabling the application of the total probability theorem to obtain the state estimate in the presence of data association uncertainty.

Under the assumption of a single target, the spurious measurements are considered random interference. A common model for such false measurements assumes that they are uniformly spatially distributed and independent across time, corresponding to residual clutter. Any constant clutter is assumed to have already been removed. Their number follows the Poisson distribution.

When several targets, as well as clutter or false alarms, appear in the same neighbourhood, the data association becomes even more challenging. Figure 3.2 shows this scenario, where predicted measurement for the targets are close to each other. These predicted points are labeled as  $\hat{z}_1$  and  $\hat{z}_2$ . In this figure, many association combinations are possible;  $z_1$  from target  $\hat{z}_1$  or clutter;  $z_2$  from target  $\hat{z}_1$  or clutter;  $z_4$  from target  $\hat{z}_2$  or clutter;  $z_3$  from target  $\hat{z}_1$  or target  $\hat{z}_2$  or clutter. However, if  $z_3$  originated from target  $\hat{z}_1$ , then it is probable, that  $z_4$  originated from target  $\hat{z}_2$ .

This scenario demonstrates the intricate relationships among associations when persistent interference from neighboring targets coexists with random interference or clutter. In such cases, joint association events become necessary to properly account for these

dependencies.

A more complex scenario may arise due to the inherent finite resolution capability of signal processing systems. While each measurement is typically assumed to originate from either a target or clutter, an additional possibility must be considered: the merging of detections from multiple targets. Specifically, measurement  $z_3$  could potentially result from such merging, representing an unresolved measurement. This introduces the fourth origin hypothesis for a measurement lying within the intersection of two validation regions.

The discussion highlights the challenges associated with associating measurements to tracks. The complete problem involves associating measurements at each time step, updating the track's sufficient statistic, and propagating it to the subsequent time step.

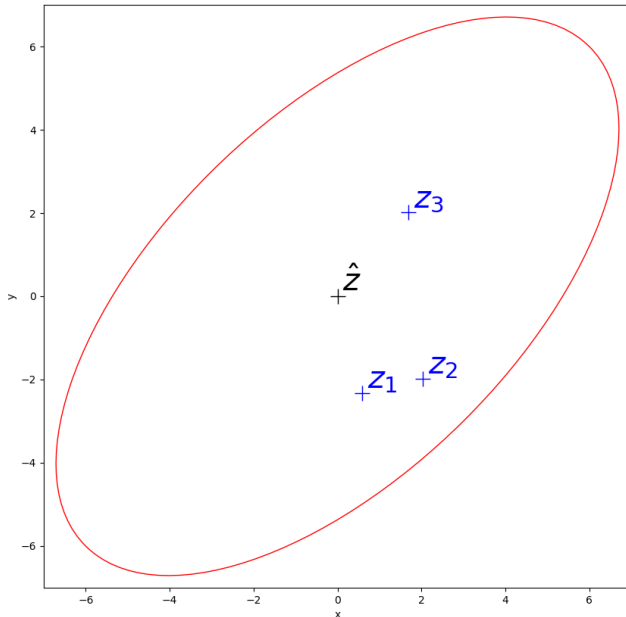


**Figure 3.1** Several measurements  $z_i$  appeared in the validation region of a single target.  $\hat{z}$  is a predicted measurement and none or any of the measurement  $z_1 - z_3$  may have originated from the target.

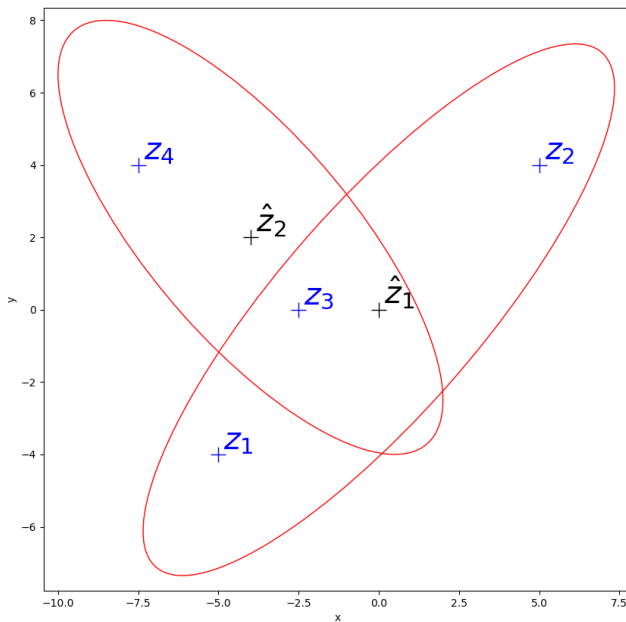


**Figure 3.2** Several measurements  $z_i$  appeared in the validation region of one of targets  $\hat{z}_1$  or  $\hat{z}_2$ .  $\hat{z}_1$  and  $\hat{z}_2$  are predicted measurements and none or any of the measurement  $z_1 - z_3$  may have originated from the target  $\hat{z}_1$  and none or any of the measurement  $z_3 - z_4$  may have originated from the target  $\hat{z}_2$ .

### 3.3 Single target tracking

Unlike conventional Kalman filter, which is not inherently equipped to handle clutter, single target tracking (STT) algorithms are specifically designed to track a single target in presence of clutter and other sources of interference. STT algorithms incorporate mechanisms to enhance target survivability in cluttered environments.

One prominent algorithm in the data association category of target tracking is the Probabilistic Data Association filter (PDA). This filter addresses the challenge of associating measurements with the correct target while accounting for data association uncertainty. This uncertainty arises from the presence of clutter and the possibility of spurious measurements.

#### 3.3.1 PDA filter

The Probabilistic Data Association filter computes the association probabilities for each validated measurement at the current time with respect to the target being tracked [25]. This probabilistic or Bayesian information serves as a foundation for the filter, which effectively addresses the uncertainty regarding the origin of measurements. In scenarios where the state and measurement equations are linear, the resulting PDA algorithm operates based on the Kalman Filter. However, if the state or measurement equations

are non-linear, the PDA algorithm is instead based on the Extended Kalman Filter. This adaptation allows the PDA algorithm to accommodate non-linearity in the system dynamics or measurement processes, ensuring a robust performance in diverse tracking scenarios.

The PDA algorithm comes with many assumptions:

1. Only one target of interest is present, whose state  $x \in R^{n_x}$  is assumed to evolve in time according to the equation

$$x_k = F_{k-1}x_{k-1} + w_{k-1}, \quad (3.1)$$

with the true measurement  $z_k \in R^{n_z}$  given by

$$z_k = H_k x_k + v_k, \quad (3.2)$$

where  $w_{k-1}$  and  $v_k$  are zero mean mutually independent, white Gaussian noise variables with covariances  $Q_{k-1}$  and  $R_k$ , respectively.

2. The track has been initialized.
3. The past information through time  $k - 1$  about the target is summarized approximately by a sufficient statistic in the form of the Gaussian posterior

$$p(x_{k-1}|z_{k-1}) = \mathcal{N}(x_{k-1}; x_{k-1|k-1}, P_{k-1|k-1}). \quad (3.3)$$

4. Every time a measurement validation region is set up around the predicted measurement to select the candidate measurements for association to the target of interest.
5. If the target was detected and the corresponding measurement fell into the validation region, then, according to (3.2), at most one of the validated measurements can be target-originated.
6. The remaining measurements are assumed to be false alarms or clutter and are modeled as independent and identically distributed with uniform spatial distribution. Additionally, the number of false alarms or clutter points obeys either a Poisson distribution, that is, a spatial Poisson process with known spatial density  $\lambda$ , or a diffuse prior.
7. The target detections occur independently over time with known probability  $p_D$ .

All these assumptions make a filter for state estimation, that is almost as simple as the Kalman filter, but more effective in the presence of clutter.

As well as the Kalman Filter, the PDAF consists of a prediction and an update step. Before the update step, two additional steps occur – measurement validation and data association.

### 3.3.1.1 PDAF predict step

The prediction step of PDA filter from time  $k - 1$  to  $k$  is as in the standard KF,

$$x_{k|k-1} = F_{k-1}x_{k-1|k-1}, \quad (3.4)$$

$$\eta_{k|k-1} = H_k x_{k|k-1}, \quad (3.5)$$

$$P_{k|k-1} = F_{k-1}P_{k-1|k-1}F_{k-1}^T + Q_{k-1}, \quad (3.6)$$

where  $P_{k-1|k-1}$  is from the Equation (3.3). The innovation covariance matrix  $S_k$  is computed as

$$S_k = H_k P_{k|k-1} H_k^T + R_k. \quad (3.7)$$

### 3.3.1.2 PDAF measurement validation step

As discussed in Section 3.2.1, measurements considered to have originated from a given target should fall into the validation region. This elliptical region is formulated as

$$\nu(k, \gamma) = \bigcup_{z \in Z_k} [(z - \hat{z}_{k|k-1})^T S_k^{-1} (z - \hat{z}_{k|k-1})) \leq \gamma], \quad (3.8)$$

where  $Z_k$  are all measurements at time  $k$ ,  $\gamma > 0$  is the gate threshold corresponding to the gate probability  $p_G$ , which is the probability, that the region contains the correct measurement if detected and  $S_k$  given in (3.7) is the covariance of the innovation.

### 3.3.1.3 PDAF data association step

Clutter in target tracking is assumed to be a Poisson model with a spatial density  $\lambda$ . In PDAF it yields to the association probability for  $z_{i,k}$  being the correct measurement as

$$\beta_{i,k} = \begin{cases} \frac{\mathcal{L}_{i,k}}{1 - p_D p_G + \sum_{j=1}^{m_k} \mathcal{L}_{j,k}}, & i = 1, \dots, m_k, \\ \frac{1 - p_D p_G}{1 - p_D p_G + \sum_{j=1}^{m_k} \mathcal{L}_{j,k}}, & i = 0, \end{cases} \quad (3.9)$$

where  $i = 0$  stands for case, where none of the measurements are correct, i.e. there is no measurement in the validation region or none of them originate from the target,  $p_D$  is the detection probability,  $p_G$  is the gate probability analogous to (3.8), and

$$\mathcal{L}_{i,k} = \frac{\mathcal{N}(z_{i,k}; \hat{z}_{k|k-1}, S_k) p_D}{\lambda} \quad (3.10)$$

is the likelihood ratio of the measurement  $z_{i,k}$  from the validation region. The parameter  $\lambda$  (the density of the spatial Poisson clutter process) in the denominator of (3.10) models the clutter density of the uniform pdf of the location of false measurement. The Probabilistic Data Association algorithm estimates association probabilities that are influenced by the position of the respective innovation on the Gaussian exponential of the likelihood ratio (3.10), in comparison to other innovations.

### 3.3.1.4 PDAF update step

The update step equation of the update step is formulated as

$$\hat{x}_{k|k} = \hat{x}_{k|k-1} + K_k \nu_k, \quad (3.11)$$

where the combined innovation is

$$\nu_k = \sum_{i=1}^{m_k} \beta_{i,k} \nu_{i,k}, \quad (3.12)$$

and the Kalman gain is the same as in (2.51)

$$K_k = P_{k|k-1} H_k^T S_k^{-1}. \quad (3.13)$$

The covariance matrix associated with the update state (3.11) is expressed as

$$P_{k|k} = \beta_{0,k} P_{k|k-1} + (1 - \beta_{0,k}) P_{k|k}^c + \tilde{P}_k, \quad (3.14)$$

where the covariance of the updated state with the corrected measurement is

$$P_{k|k}^c = P_{k|k-1} - K_k S_k K_k^T, \quad (3.15)$$

and of the innovation term spreads according to

$$\tilde{P}_k = K_k \left( \sum_{i=1}^{m_k} \beta_{i,k} \nu_{i,k} \nu_{i,k}^T - \nu_k \nu_k^T \right) K_k^T. \quad (3.16)$$

With probability  $\beta_{0,k}$  none of the measurements are correct. In such case, there is no update step of the state estimation. The prediction covariance  $P_{k|k-1}$  in (3.14) has weight  $\beta_{0,k}$ . There is a probability  $1 - \beta_{0,k}$  that correct measurement appears and the update covariance  $P_{k|k}^c$  has weight  $1 - \beta_{0,k}$ . However, there is no certainty, which of the validated measurement  $z_k$  is correct, so the positive semidefinite covariance matrix increases. This matrix is the result of the measurement origin uncertainty. Note, that in (3.16) the dependence of the estimation is non-linear. The PDAF is a non-linear estimator, while the estimate update in (3.11) appears linear, but the association probabilities  $\beta_{i,k}$  depend on the innovation in (3.9).

## 3.4 Multi-target tracking

In the field of multi-target tracking, there are many different algorithms and approaches. One of the classes is the particle filters approach ([3], [26]–[28]). These filters are able to handle non-linear motion, but the computational demands are really high. The second class is data association filters and random finite sets filters, which are usually more effective when it comes to computational demands. The example of data association, which we mentioned in Section 3.1, is the PDA filter (Section 3.3.1) or the integrated probabilistic data association filter [4]. The joint probabilistic data association filter [25] and the joint integrated probabilistic data association filter [4] are advanced versions of these filters. They can handle more targets, especially when two or more targets' validation regions overlap. The other family are filters based on random finite sets. Random finite sets statistics are explained in the following section.

### 3.4.1 RFS statistics

Multi-target tracking presents challenges in estimating the states of multiple dynamic objects over time, complicated by varying target counts, cluttered sensor measurements, and data association ambiguity. Traditional tracking frameworks rely on explicit associations between measurements and targets, leading to computational complexities, particularly in scenarios with high target densities and clutter rates.

Recent advancements introduce Random Finite Set (RFS) theory as an alternative approach to multi-target tracking. RFS theory represents sets with random cardinalities and values, offering a flexible framework for modeling uncertain multi-target scenarios. By treating both the multitarget state and sensor measurements as a RFS, tracking algorithms can effectively capture uncertainties.

In a scenario with more targets, i.e., a multi-target scenario, let  $M(k)$  be the number of targets at time  $k$ . At time  $k - 1$ , the target states  $x_{k-1,1}, \dots, x_{k-1,M(k-1)} \in \mathcal{X}$  are assumed to follow Markov process on the state-space  $\mathcal{X} \subseteq \mathbb{R}^{n_x}$ . At the following time step  $k$ , some of these targets may disappear, some may evolve to their new states and, what is more, some new targets may be born. The result are  $M(k)$  targets with states  $x_{k,1}, \dots, x_{k,M(k)} \in \mathcal{X}$ . The RFS model formulation ensures, that the order in which the states are listed has no significance. Also, at time  $k$ ,  $N(k)$  measurements  $z_{k,1}, \dots, z_{k,N(k)} \in \mathcal{Z}$ , observed in the observation-space  $\mathcal{Z} \subseteq \mathbb{R}^{n_z}$ , are received by the sensors, but the origins of these measurements are not known. The RFS model again ensures, that the order in which the measurements came, has no significance. Some of these measurements are generated by the targets, some are false measurements, i.e., clutter.

The goal of multi-target tracking is to collectively estimate both the quantity of targets and their respective states using measurements of uncertain origin. Even under ideal circumstances where the sensor detects all targets without clutter, single-target filtering techniques are inadequate due to the absence of information regarding the origin of each observation.

Given the absence of inherent ordering within the sets of target states and measurements at a specific time, they can be naturally depicted as finite sets, denoted as

$$X_k = \{x_{k,1}, \dots, x_{k,M(k)}\} \in \mathcal{F}(\mathcal{X}) \quad (3.17)$$

$$Z_k = \{z_{k,1}, \dots, z_{k,N(k)}\} \in \mathcal{F}(\mathcal{Z}), \quad (3.18)$$

where  $\mathcal{F}(\mathcal{X})$  and  $\mathcal{F}(\mathcal{Z})$  are collections of all finite subsets of  $\mathcal{X}$  and  $\mathcal{Z}$ , respectively. In the random finite set framework, we consider the sets of targets and measurements, denoted as  $X_k$  and  $Z_k$ , respectively, as the state and the observation. This approach defines multi-target tracking as a filtering task with a state-space  $\mathcal{F}(\mathcal{X})$  and an observation-space  $\mathcal{F}(\mathcal{Z})$ . For single target scenarios, uncertainty is represented using random vectors for state  $x_k$  and measurement  $z_k$ . Similarly, in multi-target scenarios, the uncertainty is modeled using random finite sets for the multi-target state  $X_k$  and the measurement  $Z_k$ . An RFS  $X$  is essentially a random variable that takes on finite sets of values, described by a discrete probability distribution and a set of joint probability densities. The distribution specifies the number of elements in  $X$ , while the densities describe the distribution of these elements.

We now delve into an RFS-based model for the evolution of the multi-target state, taking into account the target motion, birth and death. Given a multi-target state  $X_{k-1}$  at time  $k-1$ , each individual target  $x_{k-1} \in X_{k-1}$  either remains present at time  $k$  with a probability  $p_{S,k}(x_{k-1})$  or disappears with a probability  $1 - p_{S,k}(x_{k-1})$ . If the target continues to exist, the probability density of transitioning from state  $x_{k-1}$  to  $x_k$  is denoted by  $f_{k|k-1}(x_k|x_{k-1})$ . Consequently, for each state  $x_{k-1} \in X_{k-1}$  at time  $k-1$ , its behavior in the subsequent time step is modeled as the RFS

$$S_{k|k-1}(x_{k-1}), \quad (3.19)$$

that can represent two scenarios: either the survival of a target, indicated by the set  $\{x_k\}$ , or the absence of a target, denoted by  $\emptyset$ , implying the target's demise.

The occurrence of a new target at time  $k$  can originate from two possibilities: spontaneous births, which are independent of any existing target, or the spawning from a target present at time  $k-1$ .

Given a multi-target state  $X_{k-1}$  at time  $k-1$ , the state  $X_k$  at time  $k$  is formulated as a union of surviving targets, newly spawned targets, and spontaneously born targets,

$$X_k = \left[ \bigcup_{\zeta \in X_{k-1}} S_{k|k-1}(\zeta) \right] \cup \left[ \bigcup_{\zeta \in X_{k-1}} B_{k|k-1}(\zeta) \right] \cup \Gamma_k, \quad (3.20)$$

where

- $\Gamma_k$  is a RFS of spontaneous births at time  $k$ ,
- $B_{k|k-1}(\zeta)$  is a RFS of targets spawned at time  $k$  from a target with previous state  $\zeta$ .

It is also assumed that RFSs in (3.20) are independent of each other, but the forms of  $\Gamma_k$  and  $B_{k|k-1}(\cdot)$  are problem dependent.

The measurement sets  $Z_k$  are also random finite sets including detection uncertainty and clutter. A target  $x_k \in X_k$  can be either detected with probability  $p_{D,k}(x_k)$  or misdetected with probability  $1 - p_{D,k}(x_k)$ . At time  $k$ , each state  $x_k$  produces an RFS

$$\Theta_k(x_k) \quad (3.21)$$

that is  $z_k$  in a case when the target is detected or  $\emptyset$  otherwise. Furthermore, the sensor not only receives measurements originated from targets, but also a set  $\mathcal{K}_k$ , which are false measurements (clutter). Thus, at time  $k$ , the multi-target measurement set  $Z_k$  observed by the sensor is also formulated as a union of measurements originated from targets and clutter

$$Z_k = \left[ \bigcup_{x \in X_k} \Theta_k(x) \right] \cup \mathcal{K}_k. \quad (3.22)$$

The RFSs are assumed to be independent of each other and the actual form of  $\mathcal{K}_k$  is problem dependent.

Finite Set Statistics (FISST) is fundamental within the RFS framework, providing a systematic way to apply the RFS theory to multi-target tracking. FISST extends

Bayesian filtering techniques to multi-target scenarios, enabling rigorous estimation of multi-target states in the presence of clutter and data association uncertainties. Detailed information, descriptions, and equations can be found in [29]. In this book, for the sake of interest, it can be found that for a function  $f = \partial F_{(\cdot)}(T)$  the set integral over a subset  $S \subset E$  is defined as

$$\int_S f(X) \partial X \equiv \sum_{i=0}^{\infty} \frac{1}{i!} \int_{S^i} f(x_1, \dots, x_i) \lambda_K^i(dx_1 \dots dx_i), \quad (3.23)$$

where  $\lambda_K(S)$  denote the hyper-volume of  $S$  in units of  $K$ , which is usually in MTT modeled as RFS Poisson process with uniform rate of  $K^{-1}$  with intensity  $\lambda = \lambda_K/K$ , i.e.,

$$\mu(\mathcal{T}) = \sum_{i=0}^{\infty} \frac{\lambda^i (\mathcal{T} \cap E^i)}{i!}, \quad (3.24)$$

where  $E$  and  $\mathcal{T}$  are closed and bounded subsets of  $R^n$  [30].

### 3.4.2 PHD filter

The PHD filter serves as an approximation devised to tackle the computational complexity inherent in the multi-target Bayes' filter. Instead of tracking the complete posterior density of multi-target states over time, the PHD filter focuses on propagating the posterior intensity, which represents the first-order statistical moment of the posterior multi-target state [5]. This operational strategy draws parallels with the constant gain Kalman filter, which tracks the first moment (mean) of the single-target state [9].

For a Random Finite Set  $X$  on  $\mathcal{X}$  with a probability distribution  $P$ , its first-order moment is a non-negative function  $v$  on  $\mathcal{X}$ , known as the intensity. This function satisfies the property that for each region  $S \subseteq \mathcal{X}$  [31]

$$\int |X \cap S| P(dX) = \int_S v(x) dx. \quad (3.25)$$

In essence, the integral of  $v$  over any region  $S$  yields the expected number of elements of  $X$  within  $S$ . Consequently, the total mass  $\hat{N} = \int v(x) dx$  represents the expected number of elements of  $X$ . The local maxima of the intensity  $v$  correspond to the points in  $\mathcal{X}$  with the highest local concentration of expected number of elements, which can then be utilized to generate estimates for the elements of  $X$ . The simplest approach involves rounding  $\hat{N}$  and selecting the resulting number of highest peaks from the intensity. In the tracking domain, this intensity is also referred to as the probability hypothesis density.

An important subclass of RFSs, namely the Poisson RFSs, is characterized entirely by its intensities. An RFS  $X$  is considered Poisson if its cardinality distribution  $Pr(|X| = n)$  follows a Poisson distribution with mean  $\hat{N}$ , and for any finite cardinality, the elements  $x \in X$  are independently and identically distributed according to the probability density  $v(\cdot)/\hat{N}$ . In the context of the multi-target tracking problem, it is a common practice to model the clutter RFS [denoted as  $\mathcal{K}_k$  in (3.22)] and the birth RFSs [ $\Gamma_k$  and  $B_{k|k-1}(x_{k-1})$  in (3.20)] as Poisson RFSs.

To formulate the PHD filter, let us first denote the multi-target state and measurement models with

$$\gamma_k(\cdot) \text{ intensity of the births RFS } \Gamma_k \text{ at time } k; \quad (3.26)$$

$$\beta_{k|k-1}(\cdot|\zeta) \text{ intensity of the RFS } B_{k|k-1}(\zeta) \text{ spawned at time } k \text{ by a target with previous state } \zeta; \quad (3.27)$$

$$p_{S,k}(\zeta) \text{ probability that a target still exists at time } k \text{ given that its previous state is } \zeta; \quad (3.28)$$

$$p_{D,k}(x) \text{ probability of detection given a state } x \text{ at time } k; \quad (3.29)$$

$$\kappa_k(\cdot) \text{ intensity of clutter RFS } \mathcal{K}_k \text{ at time } k. \quad (3.30)$$

PHD filter naturally comes with certain assumptions.

1. Each target evolves and generates observations independently of each other.
2. Clutter is Poisson and independent of target-originated measurements.
3. The predicted multi-target RFS governed by  $p_{k|k-1}$  is Poisson.

Assumptions 1 and 2 are very common in several tracking applications. The assumption 3 is acceptable approximation in situations with small correlation between targets and is satisfied when there is no spawning and RFSs  $X_{k-1}$  and  $\Gamma_k$  are Poisson.

### 3.4.2.1 PHD filter recursion

Assume a target state  $x$  described by an intensity function  $v(x)$ . At time  $k$ , the prediction of the prior intensity  $v_{k|k-1}(x)$  is given by

$$\begin{aligned} v_{k|k-1}(x) = & \int p_{S,k}(\zeta) \phi_{k|k-1}(x|\zeta) v_{k-1}(\zeta) d\zeta \\ & + \int \beta_{k|k-1}(x|\zeta) v_{k-1}(\zeta) d\zeta + v_{\gamma,k}(x), \end{aligned} \quad (3.31)$$

where  $p_{S,k}(\cdot)$  is the probability of target survival,  $\phi_{k|k-1}(\cdot|\cdot)$  is the target state transition density, and  $v_{\gamma,k}(\cdot)$  denotes the prior PHD of the target's birth at time  $k$ . The predicted intensity  $v_{k|k-1}$  is then updated by the measurement set  $Z_k$  given by sensors at time  $k$  according to the Bayesian update

$$\begin{aligned} v_k(x) = & [1 - p_{D,k}(x)] v_{k|k-1}(x) \\ & + \sum_{z \in Z_k} \frac{p_{D,k}(x) g_k(z|x) v_{k|k-1}(x)}{\kappa_k(z) + \int p_{D,k}(\zeta) g_k(z|\zeta) v_{k|k-1}(\zeta) d\zeta}, \end{aligned} \quad (3.32)$$

where  $g_k(\cdot|\cdot)$  is the likelihood function,  $p_{D,k}(\cdot)$  is the probability of detection, and  $\kappa_k(\cdot)$  is the clutter density.

Equations (3.31) and (3.32) show that the PHD filter avoids the combinatorial ineffectiveness resulting from the unknown association of measurements with correct targets. The posterior intensity is a function of a single-target state space  $\mathcal{X}$ , thus the recursion is more computationally effective than (2.35) and (2.36) that in the case of the PHD filter operates on  $\mathcal{F}(\mathcal{X})$ . Although, in general, it is not possible to come up with a closed-form solution for the PHD recursion.

### 3.4.2.2 GM-PHD for linear models

In this section we delve into details of multi-target linear PHD Gaussian models. With PHD recursions (3.31) and (3.32) it is achievable to get an efficient multi-target closed-form solution for multi-target algorithms. This solution proposed by Vo and Ma in [9] requires additional assumptions to the already proposed ones. A standard linear Gaussian model for each of the targets is assumed and the linear Gaussian multi-target model includes assumptions on the death, birth, and detections.

4. Each target follows a linear Gaussian dynamical model and the sensor has a linear Gaussian measurement model, i.e.,

$$f_{k|k-1}(x|\zeta) = \mathcal{N}(x; F_{k-1}\zeta, Q_{k-1}), \quad (3.33)$$

$$g_k(z|x) = \mathcal{N}(z; H_k x, R_k), \quad (3.34)$$

where  $\mathcal{N}(\cdot; m, P)$  is a Gaussian density with mean  $m$  and covariance  $P$ ,  $F_{k-1}$  is the state transition matrix,  $Q_{k-1}$  is the process noise covariance,  $H_k$  is the observation matrix and  $R_k$  is the observation noise covariance.

5. The survival and detection probabilities are state independent, i.e.,

$$p_{S,k}(x) = p_{S,k}, \quad (3.35)$$

$$p_{D,k}(x) = p_{D,k}. \quad (3.36)$$

6. The intensities of the birth and spawn RFSs are Gaussian mixtures of the form

$$\gamma_k(x) = \sum_{i=1}^{J_{\gamma,k}} w_{\gamma,k}^{(i)} \mathcal{N}(x; m_{\gamma,k}^{(i)}, P_{\gamma,k}^{(i)}), \quad (3.37)$$

$$\beta_{k|k-1}(x|\zeta) = \sum_{j=1}^{J_{\beta,k}} w_{\beta,k}^{(j)} \mathcal{N}(x; F_{\beta,k-1}^{(j)}\zeta + d_{\beta,k-1}^{(j)}, Q_{\beta,k-1}^{(j)}), \quad (3.38)$$

where  $J_{\gamma,k}$ ,  $w_{\gamma,k}^{(i)}$ ,  $m_{\gamma,k}^{(i)}$ ,  $P_{\gamma,k}^{(i)}$ ,  $i = 1, \dots, J_{\gamma,k}$  are given model parameters that actuate the shape of the birth intensity and  $J_{\beta,k}$ ,  $w_{\beta,k}^{(j)}$ ,  $F_{\beta,k-1}^{(j)}$ ,  $d_{\beta,k-1}^{(j)}$  and  $Q_{\beta,k-1}^{(j)}$ ,  $j = 1, \dots, J_{\beta,k}$  determine the shape of the spawning intensity of a target with previous state  $\zeta$ .

Assumptions 4 and 5 are very common and used in various tracking algorithms [32], but the closed-form solution allows for state- and time-dependent  $p_{S,k}$  and  $p_{D,k}$ . This convenience is used in the practical part of this thesis.

The means  $m_{\gamma,k}^{(i)}$  in assumption 6 are the peaks of the spontaneous birth intensity in (3.37). These are the points with highest concentrations of the expected number of spontaneous births, meaning they represent places like airports or other places with highest probability target appearance.  $P_{\gamma,k}^{(i)}$  is the covariance matrix that regulates the spread of the birth intensity. The weight  $w_{\gamma,k}^{(i)}$  gives the expected number of new targets originating from  $m_{\gamma,k}^{(i)}$ . Similary in (3.38) with addition, that the peak  $F_{\beta,k-1}^{(j)}\zeta + d_{\beta,k-1}^{(j)}$  is an affine function of  $\zeta$ . This spawned target can be pictured as a new target spawned in the neighborhood of another target with previous state  $\zeta$ . This can be, for example, a smaller ship detached from its mother ship.

### 3.4.2.3 GM-PHD recursion for linear models

In this section we delve into Gaussian mixture probability hypothesis density filter recursion for the linear Gaussian multi-target model and its closed-form solution to the (3.31) and (3.32). Suppose, that with assumptions 4-6 the posterior intensity at time  $k - 1$  is a Gaussian mixture of the form

$$\nu_{k-1}(x) = \sum_{i=1}^{J_{k-1}} w_{k-1}^{(i)} \mathcal{N}(x; m_{k-1}^{(i)}, P_{k-1}^{(i)}). \quad (3.39)$$

Then, the predicted intensity for time  $k$  is also a Gaussian mixture and is given by

$$\nu_{k|k-1}(x) = \nu_{S,k|k-1}(x) + \nu_{\beta,k|k-1}(x) + \gamma_k(x), \quad (3.40)$$

where  $\gamma_k(x)$  is given in (3.37). This yields

$$\nu_{S,k|k-1}(x) = p_{S,k} \sum_{j=1}^{J_{k-1}} w_{k-1}^{(j)} \mathcal{N}(x; m_{S,k|k-1}^{(j)}, P_{S,k|k-1}^{(j)}), \quad (3.41)$$

$$m_{S,k|k-1}^{(j)} = F_{k-1} m_{k-1}^{(j)}, \quad (3.42)$$

$$P_{S,k|k-1}^{(j)} = Q_{k-1} + F_{k-1} P_{k-1}^{(j)} F_{k-1}^T, \quad (3.43)$$

$$\nu_{\beta,k|k-1}(x) = \sum_{j=1}^{J_{k-1}} \sum_{l=1}^{J_{\beta,k}} w_{k-1}^{(j)} w_{\beta,k}^{(l)} \mathcal{N}(x; m_{\beta,k|k-1}^{(j,l)}, P_{\beta,k|k-1}^{(j,l)}), \quad (3.44)$$

$$m_{\beta,k|k-1}^{(j,l)} = F_{\beta,k-1}^{(l)} m_{k-1}^{(j)} + d_{\beta,k-1}^{(l)}, \quad (3.45)$$

$$P_{\beta,k|k-1}^{(j,l)} = Q_{\beta,k-1}^{(l)} + F_{\beta,k-1}^{(l)} P_{\beta,k-1}^{(l)} (F_{\beta,k-1}^{(l)})^T. \quad (3.46)$$

Thus the predicted intensity at the time  $k$  is a Gaussian mixture

$$\nu_{k|k-1}(x) = \sum_{i=1}^{J_{k|k-1}} w_{k|k-1}^{(i)} \mathcal{N}(x; m_{k|k-1}^{(i)}, P_{k|k-1}^{(i)}), \quad (3.47)$$

and the posterior intensity at time  $k$  is also a Gaussian mixture

$$\nu_k(x) = (1 - p_{D,k}) \nu_{k|k-1}(x) + \sum_{z \in Z_k} \nu_{D,k}(x; z), \quad (3.48)$$

where

$$\nu_{D,k}(x; z) = \sum_{j=1}^{J_{k|k-1}} w_k^{(j)}(z) \mathcal{N}(x; m_{k|k}^{(j)}(z), P_{k|k}^{(j)}), \quad (3.49)$$

$$w_k^{(j)}(z) = \frac{p_{D,k}^{(j)}(x; z) w_{k|k-1}^{(j)}(z) q_k^{(j)}(z)}{\kappa_k(z) + p_{D,k}^{(j)}(x; z) \sum_{l=1}^{J_{k|k-1}} w_{k|k-1}^{(l)} q_k^{(l)}(z)}, \quad (3.50)$$

$$m_{k|k}^{(j)}(z) = m_{k|k-1}^{(j)} + K_k^{(j)}(z - H_k m_{k|k-1}^{(j)}), \quad (3.51)$$

$$P_{k|k}^{(j)}(z) = [I - K_k^{(j)} H_k] P_{k|k-1}^{(j)}, \quad (3.52)$$

$$K_k^{(j)}(z) = P_k^{(j)} H_k^T (H_k P_{k|k-1}^{(j)} H_k^T + R_k)^{-1}. \quad (3.53)$$

Formulas (3.39), (3.40) and (3.47), (3.48) are the result of applying standard Gaussian properties, i.e., given  $F, d, Q, m$  and  $P$  of appropriate dimensions and  $Q, P$  are positive definite matrices, this yields

$$\int \mathcal{N}(x; F\zeta + d, Q) \mathcal{N}(\zeta; m, P) d\zeta = \mathcal{N}(x; Fm + d, Q + FPF^T) \quad (3.54)$$

and given  $H, R, m$  and  $P$  of appropriate dimensions assuming  $R$  and  $P$  are positive definite matrices

$$\mathcal{N}(z; Hx, R) \mathcal{N}(x; m, P) = q(z) \mathcal{N}(x; \tilde{m}, \tilde{P}), \quad (3.55)$$

where

$$q(z) = \mathcal{N}(z; Hm, R + HPH^T), \quad (3.56)$$

$$\tilde{m} = m + K(z - Hm), \quad (3.57)$$

$$\tilde{P} = (I - KH)P, \quad (3.58)$$

$$K = PH^T(HPH^T + R)^{-1}. \quad (3.59)$$

Equations (3.33), (3.35), and (3.37) - (3.39) are inserted into the PHD prediction Equation (3.31), and then substituting integrals of the type (3.54) by appropriate Gaussian functions. Similarly, Formulas (3.47), (3.48) are established by substituting Equations (3.34), (3.36), and (3.47) into the PHD update Equation (3.32), and subsequently replacing integrals resembling form (3.54) and products of Gaussians resembling Form (3.55) with appropriate Gaussian functions.

If the initial prior intensity  $\nu_0$  is a Gaussian mixture, then all following predicted intensities  $\nu_{k|k-1}$  and posterior intensities  $\nu_k$  are also Gaussian mixtures and the recursion holds. Formulas (3.39) and (3.40) give a closed-form guidance for computing the means, covariances and weights of  $\nu_k$  from  $\nu_{k|k-1}$  after a new set of measurements is available.

The intensity  $\nu_{k|k-1}$  in (3.40) includes three intensities  $\nu_{S,k|k-1}, \nu_{,k|k-1}$  and  $\gamma_k$ . These intensities represent existing targets, spawned targets and spontaneous births. The updated intensity  $\nu_k$  consists of a misdetection case  $(1 - p_{D,k})\nu_{k|k-1}$  and  $|Z_k|$  detection cases  $\nu_{D,k}(\cdot; z)$  for every  $z \in Z_k$ . The GM-PHD recursion prediction step thus follows

the Kalman prediction step and the GM-PHD update step follows the Kalman update step.

By summing the weights of  $\nu_{k|k-1}$  and  $\nu_k$  we can get the expected number of targets  $\tilde{N}_{k|k-1}$  and  $\tilde{N}_k$ , respectively,

$$\tilde{N}_{k|k-1} = \tilde{N}_{k-1} \left( p_{S,k} + \sum_{j=1}^{J_{\beta,k}} w_{\beta,k}^{(j)} \right) + \sum_{j=1}^{J_{\gamma,k}} w_{\gamma,k}^{(j)} \quad (3.60)$$

$$\tilde{N}_k = \tilde{N}_{k|k-1} (1 - p_{D,k}) + \sum_{z \in Z_k} \sum_{j=1}^{J_{k|k-1}} w_k^{(j)}(z), \quad (3.61)$$

where  $\tilde{N}_{k|k-1}$  is the expected number of targets after the prediction step, which is the sum of surviving, spawning and born targets. Similary,  $\tilde{N}_k$  is the expected number of targets after the update step, which is the sum of the updated number of targets plus the mean number of targets that are not detected.

The GM-PHD filter pseudo-algorithm is provided in Algorithm 2.

#### 3.4.2.4 Pruning and merging in GM-PHD filter

Due to the propagation of the Gaussian mixture in time, the PHD filter suffers from computation issues resulting from exponential increase of Gaussian components

$$(J_{k-1}(1 + J_{\beta,k}) + J_{\gamma,k})(1 + |Z_k|) = O(J_{k-1}|Z_k|), \quad (3.62)$$

where  $J_{k-1}$  is the number of Gaussian components of the intensity  $\nu_{k-1}$ .

To resolve this issue, many techniques can be applied. The simplest one is to remove components with a low weight to the next timestep. This can be done by predefining a threshold. Only targets with a higher weight than this threshold continue to survive.

The next possibility is keeping a certain number of targets and removing the ones with the lowest weight. However, some of the Gausssian components can appear so close together, that they can be merged into a single component. Such procedure is a good approximation with appropriate merging threshold. Pseudo-algorithm for this procedure is shown in Algorithm 3.

After computing the posterior intensity  $\nu_k$ , the subsequent objective is to derive estimates for multi-target states. In the context of the Gaussian mixture representation of  $\nu_k$ , extracting estimates for the multi-target states becomes relatively straightforward, as the means of the individual Gaussian components typically correspond to the local maxima of  $\nu_k$ , given that they are adequately separated. However, it is essential to note that closely spaced Gaussian components may have been merged.

Since the magnitude of each peak is influenced by both its weight and covariance, merely selecting the  $\tilde{N}_k$  highest peaks of  $\nu_k$  may yield state estimates associated with Gaussians with weak weights. This scenario is suboptimal, as the expected number of targets attributed to these peaks might be small despite their peak magnitudes being substantial. A more effective approach involves choosing the means of the Gaussians with weights exceeding a certain threshold, such as 0.5. This method ensures a more robust selection of state estimates.

The outlined procedure for the state estimation in the Gaussian mixture PHD filter is summarized in Algorithm 4.

**Algorithm 2** Pseudo-algorithm for the GM-PHD filter

---

**Require:**  $\{w_{k-1}^{(i)}, m_{k-1}^{(i)}, P_{k-1}^{(i)}\}_{i=1}^{J_{k-1}}$ , and the measurement set  $Z_k$ .

1:  
2: **procedure** PREDICTION STEP FOR BIRTH TARGETS:  
3:   **for**  $j = 1, \dots, J_{\gamma,k}$  **do**  
4:      $i := i + 1$ ,  
5:      $w_{k|k-1}^{(i)} = w_{\gamma,k}^{(i)}$ ,  $m_{k|k-1}^{(i)} = m_{\gamma,k}^{(i)}$ ,  $P_{k|k-1}^{(i)} = P_{\gamma,k}^{(i)}$ ,  
6:   **end for**  
7:   **for**  $j = 1, \dots, J_{\beta,k}$  **do**  
8:     **for**  $l = 1, \dots, J_{k-1}$  **do**  
9:        $i := i + 1$ ,  
10:        $w_{k|k-1}^{(i)} = w_{k-1}^{(l)} w_{\beta,k}^{(j)}$ ,  
11:        $m_{k|k-1}^{(i)} = d_{\beta,k-1}^{(j)} + F_{\beta,k-1}^{(j)} m_{k-1}^{(l)}$ ,  
12:        $P_{k|k-1}^{(i)} = Q_{\beta|k-1}^{(j)} + F_{\beta,k-1}^{(j)} P_{k-1}^{(l)} (F_{\beta,k-1}^{(j)})^T$ .  
13:     **end for**  
14:   **end for**  
15: **end procedure**

16:  
17: **procedure** PREDICTION STEP FOR EXISTING TARGETS:  
18:   **for**  $j = 1, \dots, J_{k-1}$  **do**  
19:      $i := i + 1$ ,  
20:      $w_{k|k-1}^{(i)} = p_{S,k} w_{k-1}^{(j)}$ ,  
21:      $m_{k|k-1}^{(i)} = F_{k-1} m_{k-1}^{(j)}$ ,  
22:      $P_{k|k-1}^{(i)} = Q_{k-1} + F_{k-1} P_{k-1}^{(j)} F_{k-1}^T$ ,  
23:   **end for**  
24:    $J_{k|k-1} = i$   
25: **end procedure**

26:  
27: **procedure** COMPUTATION OF PHD UPDATE COMPONENTS:  
28:   **for**  $j = 1, \dots, J_{k|k-1}$  **do**  
29:      $\eta_{k|k-1}^{(j)} = H_k m_{k|k-1}^{(j)}$ ,  $S_k^{(j)} = R_k + H_k P_{k|k-1}^{(j)} H_k^T$ ,  
30:      $K_k^{(j)} = P_{k|k-1}^{(j)} H_k^T [S_k^{(j)}]^{-1}$ ,  $P_{k|k}^{(j)} = [I - K_k^{(j)} H_k] P_{k|k-1}^{(j)}$ .  
31:   **end for**  
32: **end procedure**

33:  
34: **procedure** PHD UPDATE STEP( $Z_k$ )  
35:   **for**  $j = 1, \dots, J_{k|k-1}$  **do** ▷ Misdetection  
36:      $w_k^{(j)} = (1 - p_{D,k}) w_{k|k-1}^{(j)}$ ,  $m_k^{(j)} = m_{k|k-1}^{(j)}$ ,  $P_k^{(j)} = P_{k|k-1}^{(j)}$   
37:   **end for**  
38:    $l := 0$   
39:   **for all**  $z \in Z_k$  **do** ▷ Detection  
40:      $l := l + 1$ ,  
41:     **for**  $j = 1, \dots, J_{k|k-1}$  **do**  
42:        $w_k^{(lJ_{k|k-1}+j)} = p_{D,k} w_{k|k-1}^{(j)} \mathcal{N}(z; \eta_{k|k-1}^{(j)}, S_k^{(j)})$ ,  
43:        $m_k^{(lJ_{k|k-1}+j)} = m_{k|k-1}^{(j)} + K_k^{(j)} (z - \eta_{k|k-1}^{(j)})$ ,  
44:        $P_k^{(lJ_{k|k-1}+j)} = P_{k|k}^{(j)}$ ,  
45:     **end for**  
46:      $w_k^{(lJ_{k|k-1}+j)} := \frac{w_k^{(lJ_{k|k-1}+j)}}{\kappa_k(z) + \sum_{i=1}^{J_{k|k-1}} w_k^{(lJ_{k|k-1}+i)}}$ , for  $j = 1, \dots, J_{k|k-1}$ ,  
47:   **end for**  
48:    $J_k = lJ_{k|k-1} + J_{k|k-1}$ .  
49: **end procedure**

50: Output:  $\{w_k^{(i)}, m_k^{(i)}, P_k^{(i)}\}_{i=1}^{J_k}$ .

---

**Algorithm 3** Pseudo-algorithm for pruning in the GM-PHD filter

---

**Require:**  $\{w_k^{(i)}, m_k^{(i)}, P_k^{(i)}\}_{i=1}^{J_k}$ , a truncation threshold T, a merging threshold U and a maximum number of allowed Gaussian terms  $J_{max}$ . Set  $l = 0$ , and  $I = \{i = 1, \dots, J_k | w_k^{(i)} > T\}$ .

- 1: **procedure** MERGING OF TARGETS
- 2:     **while**  $I \neq \emptyset$  **do**
- 3:          $l := l + 1$
- 4:          $j := \text{argmax}_{i \in I} w_k(i)$ ,
- 5:          $L := \left\{i \in I | (m_k^{(i)} - m_k^{(j)})^T (P_k(i))^{-1} (m_k^{(i)} - m_k^{(j)}) \leq U\right\}$ ,
- 6:          $\tilde{w}_k^{(l)} = \sum_{i \in L} w_k^{(i)}$ ,
- 7:          $\tilde{m}_k^{(l)} = \frac{1}{\tilde{w}_k^{(l)}} \sum_{i \in L} w_k(i) x_k^{(i)}$ ,
- 8:          $\tilde{P}_k^{(l)} = \frac{1}{\tilde{w}_k^{(l)}} \sum_{i \in L} w_k^{(i)} (P_k^{(i)} + (m_k^{(l)} - m_k^{(i)}) (m_k^{(l)} - m_k^{(i)})^T)$ ,
- 9:          $I := I / L$ .
- 10:      **end while**
- 11:     **end procedure**
- 12:
- 13: If  $l > J_{max}$  then replace  $\{\tilde{w}_k^{(i)}, \tilde{m}_k^{(i)}, \tilde{P}_k^{(i)}\}_{i=1}^l$  by those of the  $J_{max}$  Gaussians with largest weights.
- 14:
- 15: Output:  $\{\tilde{w}_k^{(i)}, \tilde{m}_k^{(i)}, \tilde{P}_k^{(i)}\}_{i=1}^l$  as pruned Gaussian components.

---

**Algorithm 4** Pseudo-algorithm for state extraction in the GM-PHD filter

---

**Require:**  $\{w_k^{(i)}, m_k^{(i)}, P_k^{(i)}\}_{i=1}^{J_k}$ .

- 1: Set  $\hat{X}_k = \emptyset$
- 2: **for**  $i = 1, \dots, j_k$  **do**
- 3:     **if**  $w_k^{(i)} > 0.5$ , **then**
- 4:         **for**  $j = 1, \dots, \text{round}(w_k^{(i)})$  **do**
- 5:             update  $\hat{X}_k := [\hat{X}_k, m_k^{(i)}]$
- 6:         **end for**
- 7:     **end if**
- 8: **end for**
- 9: Output:  $\hat{X}_k$  as the multi-target state estimate.

---

## Chapter 4

# Object detection and segmentation

In this thesis we focus on tracking objects in video data using target tracking algorithms with the dynamic detection probability due to the existence of obstacles that cause the sensors misdetect objects in certain situations. The image object detector serves as a sensor for obtaining measurements.

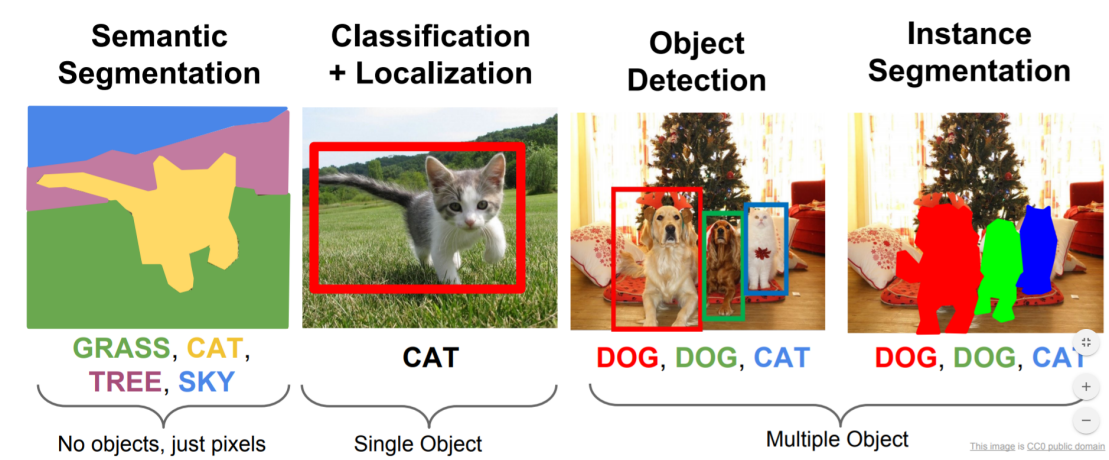
## 4.1 Object detection

Object detection is a fundamental task in computer vision that involves identifying and localizing objects within images or video frames, respectively. Unlike the image classification, which assigns a single label to an entire image, object detection algorithms aim to detect multiple objects of various classes and localize them with bounding boxes. Alongside the image classification and object detections, there are other tasks, such as semantic segmentation and instance segmentation. Figure 4.1 shows the differences between these types of image processing tasks.

The development of the object detection algorithms has progressed significantly over the years, driven by advances in deep learning, dataset availability, and computational power. Traditional object detection methods relied on handcrafted features and machine learning algorithms, such as sliding window-based classifiers, histogram of oriented gradients (HOG) [33], and Haar cascades [34]. While proving effective in certain scenarios, these methods often lacked robustness and scalability, particularly in complex and cluttered scenes.

With the advent of deep learning, convolutional neural networks (CNNs) improved the field of object detection. These networks are capable of automatically learning hierarchical representations of data, making them well suited for image analysis tasks. The rise of CNN-based approaches has led to significant improvements in object detection accuracy and efficiency. At its core, a convolutional neural network is comprised of multiple layers, each designed to perform specific operations on input data, typically images. The fundamental layers in an architecture of these networks include convolutional layers, pooling layers, and fully connected layers.

**1. Convolutional layers:** These layers are responsible for extracting features from the input data. They consist of filters (also called kernels) that slide across the input



■ **Figure 4.1** Image detection and segmentation task types. (Source: techvidvan.com.)

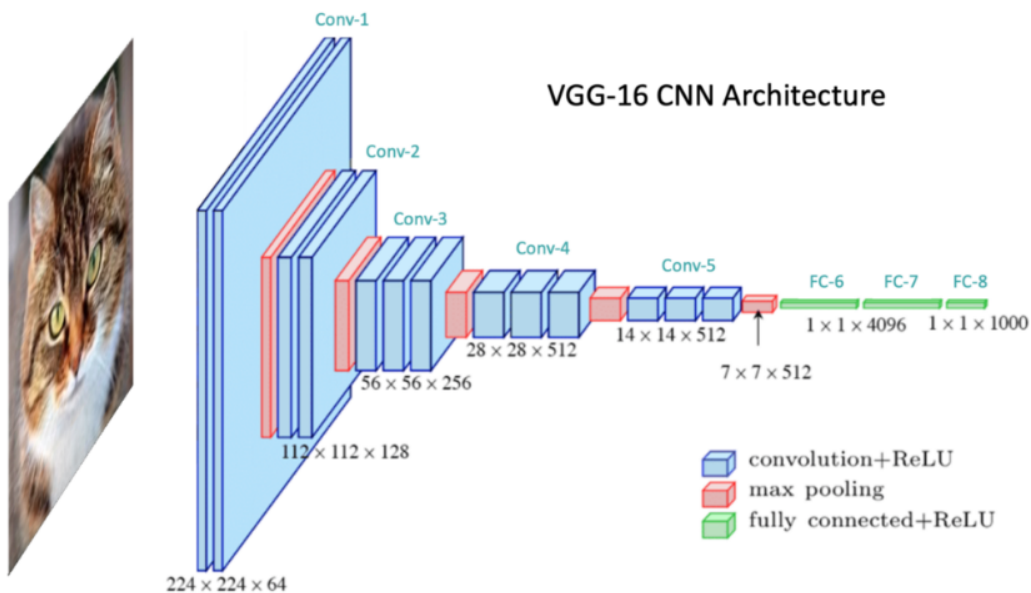
image, performing a mathematical operation known as convolution. Each filter detects certain patterns or features, such as edges, textures, or shapes. By convolving the filters with the input image, the CNN can capture hierarchical representations of features, starting from simple edges and gradients to more complex structures.

2. **Pooling layers:** Pooling layers are interspersed between convolutional layers to reduce the spatial dimensions of the feature maps while retaining important information. Common pooling operations include max pooling and average pooling, which downsample the feature maps by taking the maximum or average value within each pooling region. This downsampling helps in reducing the computational complexity and in controlling the overfitting by enforcing the spatial invariance.
3. **Fully connected layers:** These layers are typically placed at the end of the CNN and serve to classify the features extracted by the convolutional layers. Each neuron in a fully connected layer is connected to every activation in the previous layer, forming a dense network. These layers use techniques like softmax activation to produce probability distributions over the classes in a classification task or regression outputs in a regression task.

It is important to note, that it is common to combine more convolutional, pooling and fully connected layers with differently sized kernels in the architecture to improve the performance. Example of such architecture is shown in Figure 4.2

During training, CNNs use a process called backpropagation to adjust the parameters (weights and biases) of the network based on the disparity between the predicted outputs and the ground truth labels. This optimization process aims to minimize a predefined loss function, such as cross-entropy loss for classification tasks or mean squared error for regression tasks. By iteratively updating the parameters using optimization algorithms like stochastic gradient descent (SGD) or its variants, CNNs gradually learn to recognize and classify patterns within the input data, ultimately improving their performance on various visual tasks such as object detection and segmentation.

Object detection poses several challenges, including variations in object appearance,



■ **Figure 4.2** CNN architecture example. (Source [learnopencv.com](http://learnopencv.com))

scale, orientation, occlusion, and cluttered backgrounds. Additionally, real-world images often contain multiple objects of different classes, making it essential for detection algorithms to handle overlapping and partially visible objects.

Furthermore, object detection systems often have to balance accuracy and speed to meet the demands of real-time applications. Achieving high detection accuracy while maintaining fast inference times is an immense challenge, especially for devices with low hardware resources and applications requiring low-latency processing.

Object detection algorithms typically consist of several components:

- **Input processing:** Images or video frames are preprocessed to standardize their format and size, often involving resizing, normalization, and data augmentation to enhance model generalization.
- **Feature extraction:** Feature extraction is performed to capture relevant information from the input data. In deep learning-based approaches, convolutional neural networks are commonly used to extract hierarchical features that encode object appearance and spatial relationships.
- **Localization:** Localization involves predicting the spatial extent of objects within the image using bounding boxes. This step requires regression or classification to estimate bounding box coordinates and confidence scores for object presence.
- **Classification:** Object classification assigns class labels to detected objects based on their visual appearance. Classification models are trained to distinguish between different object categories, enabling an accurate identification of objects within the scene.

- **Post-processing:** Post-processing techniques, such as the non-maximum suppression (NMS), are applied to refine detection results, suppress duplicate detections, and improve localization accuracy.

### 4.1.1 YOLO

In the realm of object detection, the emergence of You Only Look Once (YOLO) represents a paradigm shift, propelled by the fusion of deep learning and innovative architectural design. YOLO stands as a testament to the transformative power of convolutional neural networks (CNNs) in redefining the landscape of computer vision applications, particularly in real-time object detection scenarios. This object detector was proposed by Joseph Redmon, Santosh Divvala, Ross Girshick, and Ali Farhadi in [35].

At its core, YOLO introduces an innovative concept: the ability to predict bounding boxes and class probabilities for objects within an image in a single pass through the neural network. This departure from the traditional object detection methods, which often involve multi-stage processes and post-processing steps, marks a significant leap forward in efficiency and speed. By consolidating object localization and classification into a unified framework, YOLO streamlines the detection pipeline, enabling seamless integration into various applications requiring rapid decision-making based on visual data.

A distinguishing feature of YOLO lies in its holistic approach to image analysis. Unlike the conventional methods that segment images into regions of interest for further processing, YOLO takes a global perspective by dividing the input image into a grid and processing it as a whole. This global context consideration not only enhances the model's understanding of spatial relationships, but also reduces the risk of misclassification, particularly in complex scenes with multiple objects. Each bounding box prediction includes coordinates ( $x, y$ ) for the center of the box, width, height, and confidence score indicating the likelihood of containing an object. Additionally, class probabilities are estimated for each bounding box to determine the object category. YOLO employs a loss function that penalizes localization errors, confidence errors, and classification errors. This loss function is optimized during training using labeled datasets to learn accurate object representations. Moreover, YOLO adopts anchor boxes to improve localization accuracy and handle scale variations of objects within the image.

The evolution of YOLO over successive versions underscores its adaptability to diverse use cases and computational environments. While early iterations prioritized speed, subsequent iterations like YOLOv4 and YOLOv5 aim to enhance accuracy without compromising real-time performance [36]. This flexibility in the model selection empowers users to tailor YOLO to their specific requirements, whether it be for surveillance systems demanding rapid detection or autonomous vehicles requiring a precise object localization.

Compared to the traditional object detection methodologies such as region-based convolutional neural networks (R-CNN) [37] and single-shot detectors (SSD), YOLO stands out for its simplicity and efficiency. By eliminating the need for complex post-processing steps and leveraging a unified architecture for object detection (see Figure 4.3 for YOLO architecture), YOLO achieves a fine balance between speed and accuracy.

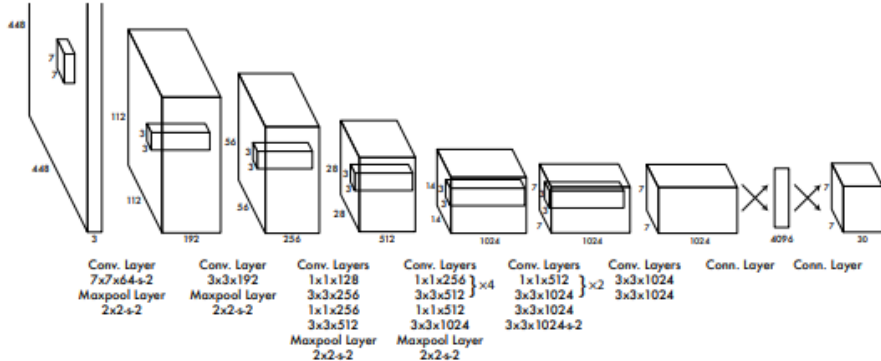


**Figure 4.3** Yolo architecture proposed in [35] has 24 convolutional layers followed by 2 fully connected layers. Convolutional layers were pretrained on the ImageNet classifier at half resolution ( $224 \times 224$  input image) and the doubled the resolution for detection. (Source [35].)

This versatility extends YOLO's applicability across a myriad of domains including, but not limited to, autonomous driving, industrial automation, healthcare imaging, and augmented reality.

## 4.2 Image segmentation

Image segmentation, a fundamental technique in computer vision, involves dividing a digital image into distinct pixel groups called segments. By breaking down the visual data into manageable segments, the image segmentation facilitates more efficient and sophisticated image processing.

The methods employed for the image segmentation vary from straightforward heuristic approaches to cutting-edge deep learning techniques. Traditional algorithms typically analyze basic visual attributes such as color and brightness to delineate object boundaries and background regions. Machine learning plays a pivotal role in this domain by training models on labeled datasets, allowing them to accurately classify objects and regions within images.

With its versatility and practical applications, image segmentation finds widespread use across artificial intelligence scenarios. Its applications span from assisting medical diagnoses through imaging to enabling automation in robotics and self-driving vehicles. Furthermore, it plays a crucial role in tasks such as identifying objects within satellite imagery.

There are three main task types in image segmentation [38]: semantic segmentation [39], instance segmentation [13] and panoptic segmentation [40]. The distinction between various types of image segmentation tasks hinges on how they handle semantic classes, which are specific categories assigned to individual pixels within an image.

In the realm of computer vision, semantic classes are broadly categorized into two types, each requiring distinct segmentation techniques for accurate results.

■ *Items* represent classes of objects characterized by identifiable shapes, such as a car,

a tree, or a person. These classes typically consist of discrete instances with consistent sizes and distinguishable constituent parts. For instance, all cars have wheels, which are distinct from the car itself.

- *Background* refers to semantic classes with amorphous shapes and variable sizes, like sky, water, or grass. Unlike *items*, *background* lacks clearly defined, countable individual instances and does not possess distinct parts. For example, both a single blade of grass and an entire field of grass fall under the category of grass.

In certain image contexts, some classes can straddle the line between being considered *items* or *background*. For instance, a large gathering of people might be interpreted either as multiple people – each being a clearly shaped, countable object, or as a singular, indistinct person.

While much of the focus in object detection typically centers on *items* classes, it is crucial to recognize that *background*, such as sky, walls, floors, and ground constitutes the bulk of our visual environment. *Background* serves as a crucial contextual information for identifying *items*. For instance, a metallic object on the road is likely a car, while a blue background behind an object is indicative of water, if it is a boat, or sky, if it is a plane. This interplay between *background* and *items* holds a particular significance for deep learning models.

### 4.2.1 Semantic segmentation

Semantic segmentation represents the most straightforward form of the image segmentation. In this approach, a semantic segmentation model assigns a semantic class to every pixel in an image, without providing an additional context or information, such as the identification of specific objects.

Unlike more nuanced segmentation techniques, semantic segmentation treats all pixels uniformly as *background* without distinguishing between *background* and *items*. This means that it does not differentiate between different types of objects within the same class.

For instance, imagine a semantic segmentation model trained to analyze urban scenes. It would generate segmentation masks outlining the boundaries of various classes of *items* and *background*. However, it would not differentiate between the individual instances of the same class. For example, if there are multiple trees in a forest, the model would likely treat them as a one continuous tree segment rather than recognizing each individual tree separately.

### 4.2.2 Instance segmentation

Instance segmentation represents a departure from the approach of semantic segmentation. While semantic segmentation focuses solely on assigning semantic classes to each pixel without distinguishing between individual instances, the instance segmentation precisely outlines the shape of each separate object instance within an image.

In essence, instance segmentation segregates *items* from *background*, disregarding the latter, and can be viewed as a more sophisticated version of object detection. Instead of

providing rough bounding boxes, instance segmentation furnishes precise segmentation masks for each object instance.

This task possesses greater challenges compared to semantic segmentation. Even when the instances of the same class overlap or touch each other, instance segmentation models must accurately separate and delineate the shape of each instance. In contrast, semantic segmentation models may simply group them together.

Instance segmentation algorithms typically adopt either a two-stage or a one-shot methodology to address the task.

Two-stage models, exemplified by Region-Based Convolutional Neural Networks [41], initially conduct conventional object detection to produce bounding boxes for each potential instance. Subsequently, they refine segmentation and classification within these bounding boxes to precisely delineate each object instance.

Conversely, one-shot models, such as YOLO, streamline the process by simultaneously performing object detection, classification, and segmentation. This approach enables a real-time instance segmentation.

While one-shot methods boast faster processing speeds, they often sacrifice some accuracy. On the other hand, two -stage approaches prioritize accuracy, but may be slower due to the additional refinement steps.

### 4.2.3 Panoptic segmentation

Panoptic segmentation represents a synthesis of semantic and instance segmentation methodologies, offering a comprehensive understanding of an image.

In panoptic segmentation, each pixel receives both a semantic label and an instance ID. Pixels with the same label and ID are assigned to the same object instance. For *background* pixels, the instance ID is disregarded.

This approach provides computer vision systems with a complete and cohesive interpretation of an image, combining the benefits of both semantic and instance segmentation. However, achieving panoptic segmentation consistently and efficiently presents significant computational challenges. Despite its evident appeal, realizing panoptic segmentation in a manner that balances accuracy and computational efficiency remains a formidable task.

The challenge in achieving panoptic segmentation lies in reconciling the conflicting approaches of semantic and instance segmentation models. Semantic segmentation treats all pixels uniformly as *background*, disregarding individual instances of objects, while instance segmentation focuses solely on isolating individual objects, ignoring the *background*. Integrating these methodologies can pose a challenge as neither of the models can effectively take on the responsibilities of the other.

Early attempts at panoptic segmentation involved combining separate semantic and instance segmentation models, followed by a post-processing phase to merge their outputs. However, these attempts encountered two significant drawbacks: It demanded substantial computational resources and struggled with inconsistencies between the data produced by the semantic segmentation network and those produced by the instance segmentation network.

Recent advancements in panoptic segmentation architectures aim to overcome these

limitations through a more unified deep learning approach. Many of these architectures utilize a common backbone network, such as a feature pyramid network (FPN) [42], to extract features from the input image. These features are then fed into parallel branches, such as a foreground branch and a background branch, or a semantic head and an instance head. The outputs from each branch are merged using a weighted system to produce the final segmentation. Notable proposed architectures include EfficientPS [40], OANet [43], PanopticFPN [44], UPSNet [45], SOGNet [46], BGRNet [47], AUNet [48], and others.

#### 4.2.4 Traditional image segmentation

Traditional image segmentation techniques leverage pixel color values and related characteristics, such as brightness, contrast, or intensity, for feature extraction. These methods are often trained with simple machine learning algorithms and are particularly useful for tasks like semantic classification. Despite their limitations in precision compared to deep learning-based approaches, traditional methods offer advantages in terms of lower cost and computational demands, allowing them to efficiently solve certain problems.

Some common traditional image segmentation techniques include:

1. **Thresholding:** Thresholding methods create binary images by classifying pixels based on whether their intensity exceeds or falls below a predetermined threshold value. Otsu's method is frequently used to identify the threshold value that minimizes intra-class variation [49].
2. **Histograms:** Histograms plot the frequency of specific pixel values in an image and are often employed to define thresholds. For instance, histograms can infer background pixel values, aiding in the isolation of object pixels.
3. **Edge detection:** Edge detection techniques identify object boundaries or classes by detecting abrupt changes in brightness or contrast [50].
4. **Watersheds:** Watershed algorithms [51] convert images to grayscale and generate a topographic map where each pixel's elevation is determined by its brightness. Regions, boundaries, and objects can be inferred from the formation of valleys, ridges, and catchment basins.
5. **Region-based segmentation:** Region-growing algorithms [52] initiate segmentation with one or more seed pixels, progressively grouping neighboring pixels with similar characteristics. These algorithms can be either agglomerative or divisive.
6. **Clustering-based segmentation:** Clustering algorithms [53], an unsupervised learning technique, split visual data into clusters of pixels with similar values. One popular variant is the k-means clustering, where  $k$  represents the number of clusters. In this method, pixel values are treated as data points, and  $k$  random points are selected as the centroids of clusters. Each pixel is then assigned to the nearest centroid based on similarity. Centroids are iteratively relocated to the mean of each cluster until convergence, resulting in stabilized clusters.

### 4.2.5 Deep learning image segmentation

Trained on meticulously annotated datasets, deep learning image segmentation models harness the power of neural networks to uncover underlying patterns within visual data. These models discern salient features crucial for tasks such as classification, detection, and segmentation.

Despite their higher computational requirements and longer training times, deep learning models consistently outperform traditional approaches, serving as the cornerstone for ongoing advancements in computer vision.

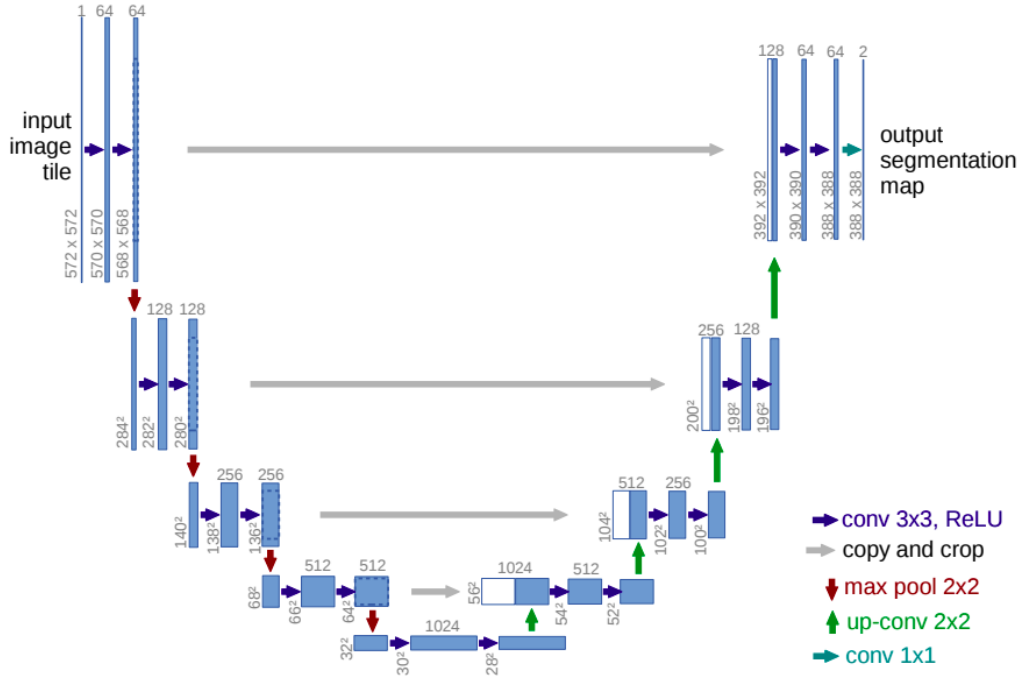
Some prominent deep learning models utilized in image segmentation include:

1. **Fully Convolutional Networks:** FCNs [54], commonly employed for semantic segmentation, are a variant of convolutional neural networks characterized by flexible layers. In FCNs, an encoder network processes a visual input through convolutional layers to extract pertinent features for segmentation or classification. The compressed feature data are then passed through decoder layers to upsample and reconstruct the input image along with segmentation masks.
2. **U-Nets:** U-Nets [55] adapt the FCN architecture to mitigate data loss during down-sampling by incorporating skip connections. These connections enable the preservation of finer details by selectively bypassing certain convolutional layers as information propagates through the network. The name U-Net derives from the shape of diagrams illustrating its layered arrangement (see Figure 4.4).
3. **Deeplab:** Similar to U-Nets, Deeplab modifies the FCN architecture [56]. In addition to utilizing skip connections, Deeplab employs dilated convolution to produce larger output maps without requiring additional computational resources.
4. **Mask R-CNNs:** Mask R-CNNs stand out as a leading model for instance segmentation [37]. These models integrate a region proposal network (RPN), responsible for generating bounding boxes for potential instances, with an FCN-based "mask head" that produces segmentation masks within each confirmed bounding box.
5. **Transformers:** Inspired by the success of transformer models [57] in natural language processing, newer models like the Vision Transformer (ViT) employ attention mechanisms in lieu of convolutional layers. These models have demonstrated comparable or superior performance to CNNs for various computer vision tasks.

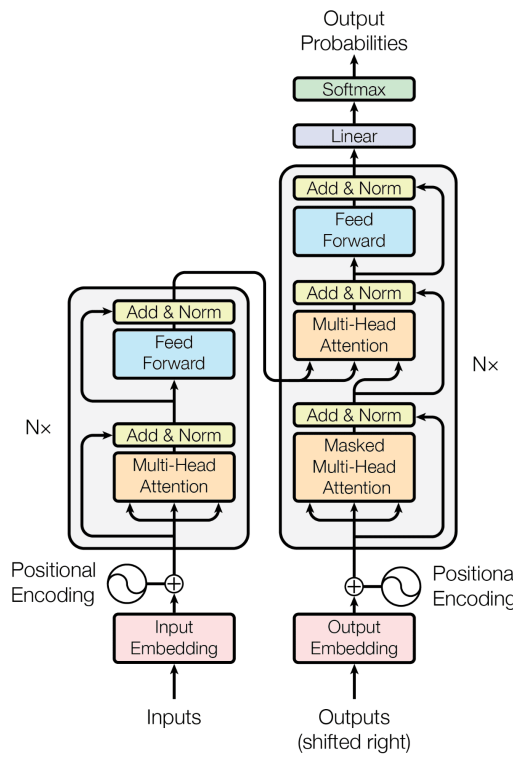
#### 4.2.5.1 Transformers

As we use the Transformer model in this work, we briefly demonstrate theirs architecture and how they work. Transformers consist of a stack of identical layers, typically comprising an encoder and a decoder (Figure 4.5). The encoder processes the input sequence, while the decoder generates the output sequence.

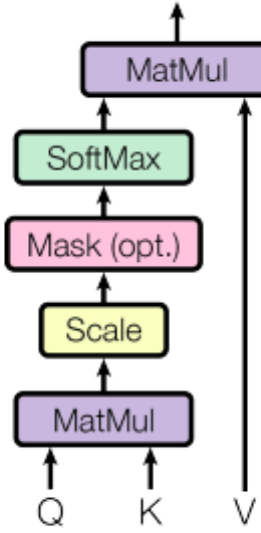
- **Encoder:** The encoder is composed of a stack of  $N = 6$  identical layers. Each layer has two sub-layers. The first is a multi-head self-attention mechanism (Figure 4.6), and the second is a position-wise fully connected feed-forward network. There is



■ **Figure 4.4** U-net architecture (example for 32x32 pixels in the lowest resolution). (Source [55])



■ **Figure 4.5** Transformer architecture. (Source [57])



■ **Figure 4.6** Multi-head attention. (Source [57])

a residual connection [58] around each of two sub-layers, followed by normalization [59]: the output of each sub-layer is  $\text{LayerNorm}(x + \text{Sublayer}(x))$ , where  $\text{Sublayer}(x)$  is the function implemented by the sub-layer itself.

- **Decoder:** The decoder is also composed of a stack of  $N = 6$  identical layers. In addition to the two sub-layers in each encoder layer, the decoder inserts a third sub-layer, which performs multi-head attention over the output of the encoder stack. Similar to the encoder, there are residual connections around each of the sub-layers, followed by layer normalization.

The core of the Transformer architecture lies in its self-attention mechanism [57]. This mechanism enables each token in the input sequence to attend to every other token, learning contextual relationships and dependencies. By computing attention scores between all pairs of tokens and taking weighted sums of their embeddings, the Transformer can effectively capture long-range dependencies and dependencies between distant tokens.

To enhance the expressiveness of self-attention, Transformers employ multi-head attention mechanisms. Instead of computing attention once, the multi-head attention computes it multiple times in parallel, each with its set of learnable parameters. This allows the model to attend to different aspects of the input sequence simultaneously, facilitating richer representations and improved performance.

Unlike sequential models, Transformers do not inherently encode the positional information of tokens. To address this limitation, positional encoding is added to the input embeddings to convey the position of each token in the sequence. This positional information is crucial for the Transformer to distinguish between tokens with the same content, but different positions within the sequence.

In addition to self-attention layers, Transformers incorporate feedforward neural networks within each layer. These FNNs consist of multiple fully connected layers with non-linear activation functions, enabling the model to capture complex interactions and transformations within the input data

$$FFN(x) = \max(0, xW_1 + b_1)W_2 + b_2, \quad (4.1)$$

where  $W$  are weights and  $b$  stands for bias.

To stabilize training and facilitate the gradient flow, Transformers employ a layer normalization and residual connections within each layer. Layer normalization normalizes the activations across feature dimensions, while residual connections enable the direct flow of gradients through the network, mitigating the vanishing gradient problem.

During training, Transformers are optimized using backpropagation and gradient-based optimization algorithms, such as Adam [60] or SGD [61], to minimize a predefined loss function. By iteratively updating the parameters of the model based on the disparity between the predicted outputs and the ground truth labels, Transformers learn to encode and generate meaningful representations of input sequences. That enables them to excel in various NLP tasks and, more recently, in image processing tasks.

#### 4.2.6 Segment Anything

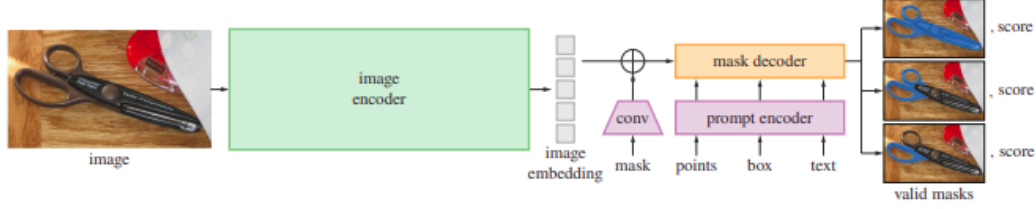
To get the state-of-the-art results in the practical part of this thesis, it is necessary to use a powerful, yet fast image segmentation model. The Segment Anything (SAM) model represents a significant advancement in image segmentation, introducing an innovative approach to tackle the challenges in this field [62]. SAM is designed to address the need for efficient and effective segmentation models that can generalize to diverse tasks and data distributions, even in zero-shot scenarios.

The SAM project introduces a new task, model, and dataset for image segmentation. It leverages a promptable model architecture to achieve an almost flawless zero-shot performance on diverse segmentation tasks. This task involves generating valid segmentation masks given any segmentation prompt. A prompt can include spatial or textual information indicating what to segment in an image. SAM ensures that the output mask is reasonable for at least one interpretation of the prompt, handling the ambiguity effectively.

SAM's architecture comprises three main components: an image encoder, a prompt encoder, and a mask decoder (Figure 4.7). The image encoder processes input images using a Vision Transformer, while the prompt encoder handles various types of prompts, including points, boxes, and text. The mask decoder efficiently generates segmentation masks based on the input image and prompt embeddings. SAM is designed for a real-time performance, enabling an interactive use with low latency.

SAM addresses ambiguity by predicting multiple output masks for a single prompt. It efficiently ranks these masks based on confidence scores, allowing it to produce accurate segmentations even in complex scenarios.

Efficiency is a core consideration in SAM's design. The model's components are optimized for a fast execution, enabling it to run in a web browser on CPU with a runtime



■ **Figure 4.7** SAM architecture (Source [62])

of approximately 50ms. This real-time performance facilitates a seamless interaction with the model for prompt-based segmentation tasks.

SAM is trained using the linear combination of the focal loss [63] and the dice loss [64], tailored for the promptable segmentation task. It simulates an interactive setup during training, sampling prompts to ensure robustness and adaptability.

SAM's contributions include the development of a promptable segmentation task, a novel model architecture optimized for a real-time performance, and a large-scale dataset (SA-1B) comprising over 1 billion masks and 11 million images. The model's zero-shot capabilities and an efficient design make it a valuable tool for various segmentation tasks, with potential applications across diverse domains. The example of segmented images are shown in Figure 4.8.



■ **Figure 4.8** The demonstration of SAM's performance. These masks were annotated fully automatically by SAM and are part of the SA-1B dataset. (Source [62])

### 4.2.7 Grounded Segment Anything

Even though the SAM model with text prompt was not released yet, many other projects have recently occurred, combining other models with SAM. One of such projects is Grounded Segment Anything [65]. This project connects image processing models,

Grounding DINO [66] as an open-set object detector, and SAM [62] as an object segmentation model. Moreover, to enhance to performance and usability of Grounded SAM, other deep-learning models are used.

- **BLIP:** BLIP is a Vision-Language Pre-training (VLP) framework which transfers flexibly to both vision -language understanding and generation tasks [67]. VLP frameworks aim to improve the performance of downstream vision and language tasks by pretraining the model on large-scale image-text pairs.
- **Recognize Anything:** Recognize Anything Model (RAM) is a string foundation model for image tagging [68]. RAM makes a substantial step for large models in computer vision, demonstrating the zero-shot ability to recognize any common category with high accuracy.
- **Stable-Diffusion:** Stable-Diffusion is a latent text-to-image diffusion model (LDMs) [69]. LDMs enhance the efficiency and flexibility of diffusion models (DMs) by training them in the latent space of pretrained autoencoders. By leveraging powerful denoising autoencoders, LDMs achieve state-of-the-art results in tasks such as image inpainting, class-conditional image synthesis, or super-resolution, while significantly reducing computational requirements.
- **OSX:** OSX is a one-stage pipeline for an expressive whole-body mesh recovery from single images [70]. OSX employs a Component Aware Transformer (CAT) consisting of a global body encoder and a local face/hand decoder. By leveraging the feature-level upsample-crop scheme and the keypoint-guided deformable attention, OSX achieves a precise estimation of face and hand parameters while maintaining connection coherence.

Grounded SAM also offers cooperation of SAM and other models: Visual ChatGPT [71], RAM++ [72], VoxelNeXt [73], and more.

## Chapter 5

# Dynamic time and state varying detection probability

As stated in the Introduction, this work focuses on tracking objects in frame sequence using target tracking methods and object detection and segmentation algorithms. Object detectors, which were discussed in the previous section, are essential for getting measurements from an image.

Note, that in all target tracking algorithms for cluttered environments and targets birth and dead possibilities, there is a parameter called the detection probability ( $p_D$ ). As its name suggests, this parameter expresses a probability that the target is detected in a particular time. It is also commonly used as a time- and state-independent scalar. The desired outcome is to enhance the performance of multi-target algorithms in scenarios where the targets may be hidden by an obstacle and reduce impacts of a misdetection of a sensor. Therefore, it is appropriate to have a dynamic time- and state-varying detection probability.

### 5.1 Problem definition

In the practical part of this thesis, three different settings of object detection and segmentation can be found. We choose Probability Hypothesis Density filter as a multi-target tracking algorithm, as it is a simpler RFS-based method. PHD filter is computationally very effective in comparison with filters such as the CPHD or the PMBM filter, which may seem as a more appropriate option for this task. However, these more complicated filters have high computational demands, which are not adequate when used in video streams. Provided settings are:

- 1. S1: YOLO + PHD** – Yolo itself can produce an object segmentation mask with lower accuracy, but with greater speed. This setting is suitable when using CPU only.
- 2. S2: YOLO + SAM + PHD** – As SAM cannot annotate labels to objects, it requires another object detector before segmentation. In this setting, we use YOLO as an object detector and SAM for mask segmentation of detected objects. This procedure requires GPU for faster computation.

- 3. S3: Grounded SAM + PHD** – Grounded SAM is the most universal approach, as it can detect objects based on a text input and uses SAM for segmentation. This setting also requires GPU for faster computation.

### 5.1.1 The modified GM-PHD filter

To modify the GM-PHD filter for our use case, a few assumptions have to be introduced. These assumptions are very similar to those of the PHD filter and the GM-PHD filter in Section 3.4.2 and 3.4.2.2.

1. Each target evolves and generates observations independently of each other.
2. Clutter is Poisson and independent of target-originated measurements.
3. The predicted multi-target RFS governed by  $p_{k|k-1}$  is Poisson.
4. Each target follows a linear Gaussian dynamical model and the sensor has a linear Gaussian measurement model, i.e.,

$$f_{k|k-1}(x|\xi) = \mathcal{N}(x; F_{k-1}\xi, Q_{k-1}), \quad (5.1)$$

$$g_k(z|x) = \mathcal{N}(z; H_k x, R_k), \quad (5.2)$$

where  $\mathcal{N}(\cdot; \cdot, \cdot)$  is a Gaussian density,  $Q_{k-1}$  is the process noise covariance,  $H_k$  is the observation matrix and  $R_k$  is the observation noise covariance.

5. The survival probability is state-independent, i.e.,

$$p_{S,k}(x) = p_{S,k}. \quad (5.3)$$

6. The detection probability is state-dependent, i.e.,

$$p_{D,k}(x) = \begin{cases} p_{D,k} & \text{if detected for the first time,} \\ p_{D,k}(x) & \text{otherwise.} \end{cases} \quad (5.4)$$

7. The intensity of the birth RFS is a Gaussian mixture of the form

$$\gamma_k(x) = \sum_{i=1}^{J_{\gamma,k}} w_{\gamma,k}^{(i)} \mathcal{N}\left(x; m_{\gamma,k}^{(i)}, P_{\gamma,k}^{(i)}\right). \quad (5.5)$$

Note, that the assumption 1 may be questionable, as the states of each of the targets are often dependently evolving. Imagine, for example, a common traffic scenario. If one of the cars immediately stops, the following vehicles have to stop as well. Meaning, they are affected by another target. The assumption 2 is reasonable, especially if we consider that the clutter rate should be very low in our scenarios. The survival probability is state-independent as in the GM-PHD filter and should be set high, as the targets are

expected to survive to the next time step. The detection probability is state-dependent and equal to  $p_{D,k}$ , i.e., a predefined threshold, in situation when the target is detected for the first time. Otherwise, if the target has evolved from the previous state  $\xi$ , the detection probability is calculated according to Section 5.2. Assumption 7 contains only intensity of the birth RFS, the spawn intensity RFS is left out. Nevertheless, it still can be easily added to the assumption and equations afterwards.

### 5.1.1.1 The modified PHD recursions

Let us assume a target state  $x$  described by an intensity function  $\nu(x)$ . At time  $k$ , the prediction of the prior intensity  $\nu_{k|k-1}(x)$  is given by

$$\nu_{k|k-1}(x) = \int p_{S,k}(\xi) \phi_{k|k-1}(x|\xi) \nu_{k-1}(\xi) d\xi + \nu_{\gamma,k}(x), \quad (5.6)$$

where  $p_{S,k}(\cdot)$  is the probability of target survival,  $\phi_{k|k-1}(\cdot|\cdot)$  is the target state transition density, and  $\nu_{\gamma,k}(\cdot)$  denotes the prior PHD of the targets birth at time  $k$ . The predicted intensity  $\nu_{k|k-1}$  is then updated by the measurement set  $Z_k$  given by sensors at time  $k$  according to the Bayesian update

$$\begin{aligned} \nu_k(x) &= [1 - p_{D,k}(x)] \nu_{k|k-1}(x) \\ &+ \sum_{z \in Z_k} \frac{p_{D,k}(x) g_k(z|x) \nu_{k|k-1}(x)}{\kappa_k(z) + \int p_{D,k}(\xi) g_k(z|\xi) \nu_{k|k-1}(\xi) d\xi}, \end{aligned} \quad (5.7)$$

where  $g_k(\cdot|\cdot)$  is the likelihood function,  $p_{D,k}(\cdot)$  is the probability of detection, and  $\kappa_k(\cdot)$  is the clutter density.

### 5.1.1.2 The modified GM-PHD recursion

In the context of the linear Gaussian multiple-target model, the PHD recursion equations (5.6) and (5.7) attain analytical solution [9]. Suppose that the posterior intensity at time  $k-1$  is a Gaussian mixture of the form

$$\nu(x) = \sum_{i=1}^{J_{\gamma,k}} w_{\gamma,k}^{(i)} \mathcal{N}(x; m_{\gamma,k}^{(i)}, P_{\gamma,k}^{(i)}). \quad (5.8)$$

The predicted intensity for time  $k$  is also a Gaussian mixture of the form

$$\nu_{S,k|k-1}(x) = \nu_{S,k|k-1}(x) + \gamma_k(x), \quad (5.9)$$

where  $\gamma_k(x)$  is given in Formula (5.5). This yields

$$\nu_{S,k|k-1}(x) = p_{S,k} \sum_{j=1}^{J_{k-1}} w_{k-1}^{(j)} \mathcal{N}(x; m_{S,k|k-1}^{(j)}, P_{S,k|k-1}^{(j)}), \quad (5.10)$$

$$m_{S,k|k-1}^{(j)} = F_{k-1} m_{k-1}^{(j)}, \quad (5.11)$$

$$P_{S,k|k-1}^{(j)} = Q_{k-1} + F_{k-1} P_{k-1}^{(j)} F_{k-1}^T. \quad (5.12)$$

Thus the predicted intensity at the time  $k$  is a Gaussian mixture

$$\nu_{k|k-1}(x) = \sum_{i=1}^{J_{k|k-1}} w_{k|k-1}^{(i)} \mathcal{N}(x; m_{k|k-1}^{(i)}, P_{k|k-1}^{(i)}), \quad (5.13)$$

and the posterior intensity at time  $k$  is also Gaussian mixture,

$$\begin{aligned} \nu_k(x) &= \sum_{i=1}^{J_{k|k-1}} [1 - p_{D,k}^{(i)}(x)] w_{k|k-1}^{(i)} \mathcal{N}(x; m_{k|k-1}^{(i)}, P_{k|k-1}^{(i)}) \\ &\quad + \sum_{z \in Z_k} \nu_{D,k}(x; z), \end{aligned} \quad (5.14)$$

where

$$\nu_{D,k}(x; z) = \sum_{j=1}^{J_{k|k-1}} w_k^{(j)}(z) \mathcal{N}(x; m_{k|k}^{(j)}(z), P_{k|k}^{(j)}), \quad (5.15)$$

$$w_k^{(j)}(z) = \frac{p_{D,k}^{(j)}(x; z) w_{k|k-1}^{(j)} q_k^{(j)}(z)}{\kappa_k(z) + p_{D,k}^{(j)}(x; z) \sum_{l=1}^{J_{k|k-1}} w_{k|k-1}^{(l)} q_k^{(l)}(z)}, \quad (5.16)$$

$$m_{k|k}^{(j)}(z) = m_{k|k-1}^{(j)} + K_k^{(j)}(z - H_k m_{k|k-1}^{(j)}), \quad (5.17)$$

$$P_{k|k}^{(j)}(z) = [I - K_k^{(j)} H_k] P_{k|k-1}^{(j)}, \quad (5.18)$$

$$\kappa_k^{(j)}(z) = P_k^{(j)} H_k^T (H_k P_{k|k-1}^{(j)} H_k^T + R_k)^{-1}. \quad (5.19)$$

The dynamically estimated detection probability in (5.14) follows from one of two possible scenarios described in Section 5.2.

### 5.1.2 S1: YOLO + PHD

It is possible to fine-tune YOLO model on personalised datasets to either improve the performance in the detection of pretrained classes, or to train the model for detecting other classes. With over 70 pretrained class instances, it is not necessary to fine tune our YOLO model for the experiments in this work. The model also detects all class instances it is trained for, that appear in a scene. For testing purposes, we filter only objects we want to detect and get measurements from. The YOLO itself is able to produce a segmentation mask in real-time, but with less accuracy and precision. This is caused by a reduced image resolution which is 640x640 pixels. To fit the YOLO output to our frame, this output needs to be resized back to our desired frame size. This resizing causes some imperfections. However, the precision to pixel level is not always necessary in our scenarios, thus this setting is, in most cases, sufficient enough. The advantage of this approach is that it runs quickly enough with CPU only. The example of object segmentation YOLO model is shown in the Figure 5.1.

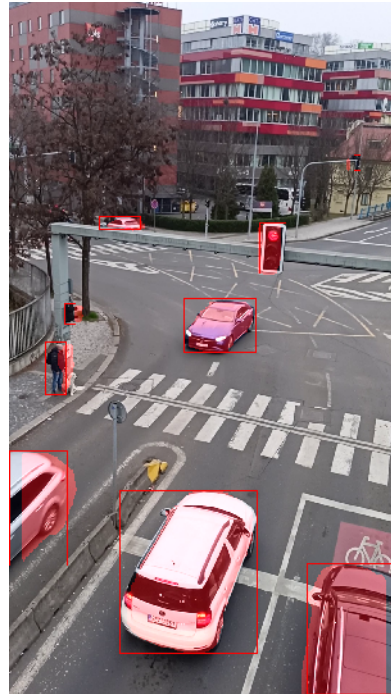


**Figure 5.1** YOLO segmentation example. This picture shows all detected objects the YOLO model is trained for and also the segmented objects' masks. These masks are imperfect, but often sufficient enough. (Kartouzská street, Prague)

### 5.1.3 S2: YOLO + SAM + PHD

The SAM model architecture in [62] is prepared to first process a text input and then segment objects based on the input. However, this feature is not available yet in the original implementation, and, for our purposes, we need an object detector before the segmentation process can be performed. The SAM model is able to segment a desired object based on one of two provided inputs with high precision and accuracy. The first possible input is a bounding box around the required object, which can be provided by an output of the YOLO model. The second option is to provide a rough center point of an object, which can also be the center of a bounding box provided by the YOLO model.

However, for our purposes, it is not recommended to use the combination of both inputs, as SAM is able to produce multiple masks for an object. For example, if we denote that we want to segment a whole person by a bounding box, one of the output masks can be just his jacket, as it makes a valid segmentation mask. Combining these two inputs can, therefore, produce this undesirable output. Another example of such behavior is shown in the Figure 5.2

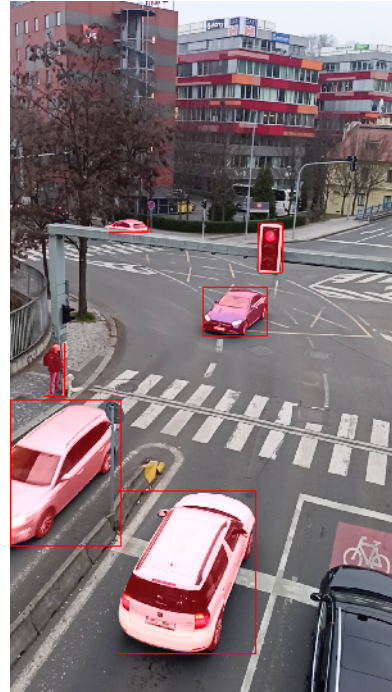
The combination of the SAM model with an object detector can segment an object with high precision and accuracy. The cooperation of these two models is demonstrated in Figure 5.3.



**(a)** By defining an object by a bounding box, SAM is able to make a segmented masks of this object and choose the most probable one.

**(b)** If we use a bounding box together with a point, we receive a different result. Here, just the truck's tire, instead of the entire wheel, is selected.

■ **Figure 5.2** Comparison of using only a bounding box vs combination of a bounding box and a point as an input for SAM.



■ **Figure 5.3** The cooperation of YOLO and SAM models. The YOLO provides bounding boxes of objects, which are inputs to SAM. The SAM model then makes segmented masks of these objects. (Kartouzská street, Prague)

#### 5.1.4 S3: Grounded SAM + PHD

Grounding DINO is an object detector that denotes objects in an image, based on a given text prompt. This feature allows us to potentially track all the required objects without the need to fine tune every class instance to a model. Moreover, this model is able to mark objects based on an ambiguous text input. Despite this universality, in cases where the model is not confident enough that the desired object appears in a scene, different results can be received with the same input every time the model is executed. This

brings uncertainty in situations with ambiguous text inputs and we should be aware of it in practical scenarios.

For a segmentation task, Grounding DINO's output serves as an input to the SAM model, as it produces bounding boxes of the detected objects. SAM uses these bounding boxes to segment objects and creates segmentation binary masks. The cooperation of these models is demonstrated in Figure 5.4.

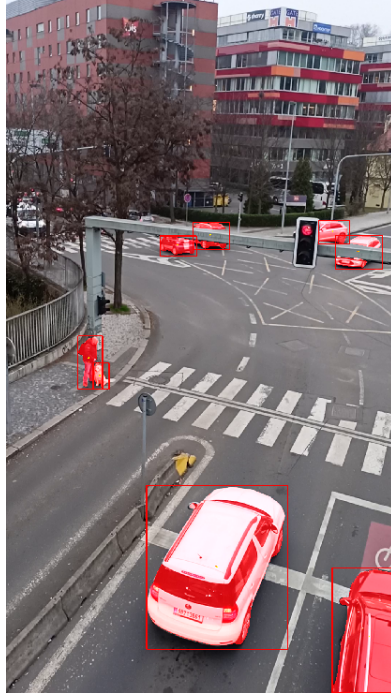


**Figure 5.4** The result of the Grounded SAM model. Grounding DINO marks objects with bounding boxes and SAM segments objects inside these bboxes. Marked objects are founded by Grounding DINO with text input *person*, *car*. (Kartouzská street, Prague)

## 5.2 Dynamic detection probability in video data

To model the dynamic state- and time-dependent detection probability  $p_{D,k}(x)$ , we propose to base the current point estimate of  $p_D(x)$  at time  $k$  on the similarity of the subsequent frame properties,

$$p_{D,k}(x) = \frac{\sum_{\sigma_j \in S_{sim}} \sum_{i=1}^{|H|} \sigma_j [h_i(M(x; k|k-1) \circ D_k), h_i(M(x; k-1) \circ D_k)]}{\|S_c\| \cdot \|H\|}, \quad (5.20)$$

where  $D_k$  is the frame in the given color spectrum,  $h_i(\cdot)$  is a color histogram made from given color spectrum,  $A \circ B$  is the Hadamard product,  $M(\cdot, \cdot)$  is the object binary mask, and  $\sigma_j[\cdot, \cdot]$  is the given similarity of two vectors.  $\|\cdot\|$  denotes the set size. The whole fraction is, in fact, the mean value across all color spectra and similarity functions.

There are many color spectra to consider, each providing certain benefits and downsides. The list of color spectra used in this work is as follows.

- **RGB** – The RGB (Red, Green, Blue) color model is ubiquitous in electronic displays, digital cameras, and computer graphics. It defines colors by their intensities of red, green, and blue components. One of its primary advantages lies in its widespread use and an intuitive representation for additive color mixing. However, RGB lacks direct perceptual relevance to human vision, as it does not inherently represent attributes like brightness or hue.
- **XYZ** – In contrast, the XYZ color space, established by the International Commission on Illumination (CIE), serves as a standard for quantifying colors in scientific and industrial applications. Even though it offers a device-independent color representation and facilitates color matching and conversion, it is not as perceptually intuitive and can be complex to work with practically.
- **HSV** – HSV (Hue, Saturation, Value) is favored in graphics software and image editing for its intuitive representation of color. It aligns better with human perception compared to RGB, allowing independent adjustment of hue, saturation, and brightness. It lacks the widespread hardware and software support enjoyed by RGB and may not be as straightforward for certain color manipulation tasks.
- **LAB** – LAB (CIELAB color space), another CIE-defined model. Unlike XYZ, it aims for perceptual uniformity. Widely used in color correction, image editing, and color management, LAB offers uniform changes in perceived color with uniform changes in LAB values. Despite its perceptual accuracy, it can be complex to comprehend and lacks universal software and hardware support compared to simpler models like RGB or HSV.
- **HLS** – HLS (Hue, Lightness, Saturation) finds its place in computer graphics and image editing applications. Similar to HSV but with lightness instead of value, HLS provides an intuitive representation for color adjustment tasks. Unfortunately, its support may not be as widespread as RGB or HSV, and it may lack the perceptual accuracy of LAB in certain color correction scenarios.

We apply a range of similarity functions, each with its unique advantages and limitations. These functions include cosine similarity, intersection, and correlation.

- **Cosine similarity** – Cosine similarity, a widely used metric, determines the cosine of the angle between two vectors in a multi-dimensional space. It is insensitive to vector magnitudes, focusing more on their orientation, which proves valuable when the absolute magnitude of vectors is less crucial than their relative orientations. However, cosine similarity does not take into account the distribution of data points. Cosine similarity is defined as

$$S_{cos}[A, B] = \frac{A \cdot B}{\|A\| \|B\|} = \frac{\sum_{i=1}^n A_i B_i}{\sqrt{\sum_{i=1}^n A_i^2} \cdot \sqrt{\sum_{i=1}^n B_i^2}}, \quad (5.21)$$

where the sums run over all elements of the arguments.

- **Intersection** – Intersection similarity, on the other hand, calculates the overlap between two sets. This metric is commonly employed in applications like document

retrieval and collaborative filtering. Its simplicity and intuitiveness make it ideal for comparing binary data or sets, where the presence or absence of elements is more significant than their values. Additionally, it treats all elements equally, disregarding their magnitudes, which can be a limitation in certain contexts. The intersection is formulated

$$S_{inter}[A, B] = \frac{\sum_{i=1}^{\|A\|} \min(A_i, B_i)}{\sum_{i=1}^{\|B\|} B_i}, \quad (5.22)$$

where  $\|\cdot\|$  denotes the set size.

- **Pearson correlation coefficient** – Correlation measures the linear relationship between two variables and is frequently used in statistics, finance, and signal processing. It captures both the strength and direction of the relationship between variables, making it valuable for identifying patterns and dependencies in data. Moreover, correlation assumes a linear relationship between variables, which may not always hold true, and it is susceptible to outliers and non-linear relationships, potentially affecting its reliability in certain scenarios. In this work, we calculate the correlation between corresponding elements in sets  $A, B$  as

$$S_{corr}[A, B] = \frac{\text{cov}(A, B)}{\sigma_A \sigma_B}, \quad (5.23)$$

where  $\text{cov}$  is the covariance and  $\sigma_{(\cdot)}$  is the standard deviation,

For simplicity, let us denote the fraction in (5.20) as  $S_c$ . This value represents the "average" similarity across all used color spectra and similarity functions.

As mentioned in Section 5.1.1.2, the dynamically estimated detection probability in (5.14) follows from one of two possible scenarios. First, there is no current measurement at time  $k$ , hence the current mask results from its predicted position,

$$p_{D,k}^{(i)}(x) = \begin{cases} S_c^{(i)} \left[ h(M_{k|k-1}^{(i)}(x) \circ D_k), h_{0,k}^{(i)} \right] & \text{if } h_{0,k}^{(i)} \text{ exists,} \\ p_{D,k}^{(i)} & \text{otherwise,} \end{cases} \quad (5.24)$$

and where the histogram from the last detection  $h_{0,k}^{(i)} \equiv h_{0,k-1}^{(i)}$  is used in the first scenario. A user-preset value  $p_{D,k}^{(i)}$  is used for targets undetected so far. The mask is obtained via

$$M_{k|k-1}^{(i)}(x) = \begin{cases} M_{k-1}^{(i)}(x)[m - v_x, n - v_y] & \text{if } m \geq v_x, n \geq v_y, \\ \mathbf{0} & \text{otherwise,} \end{cases} \quad (5.25)$$

where  $m, n$  are indices of the binary mask  $M$  and  $v_x, v_y$  are x- and y-direction velocities of the target.  $\mathbf{0}$  is a zero vector of the same size as the mask. The second scenario takes the current measurement  $z$  into account. The detection probability is modified according to

$$p_{D,k}^{(j)}(x; z) = S_c \left[ h(M_k^{(j)}(z) \circ D_k), h_{0,k}^{(j)} \right], \quad (5.26)$$

where  $h_{0,k}^{(j)}$  is the histogram resulting from the last detection,

$$h_{0,k}^{(j)} = \begin{cases} h(M_{k-1}^{(j)}(z) \circ D_{k-1}) & \text{if } h(M_{k-1}^{(j)}(z)) \text{ exists,} \\ h_{0,k-1} & \text{otherwise.} \end{cases} \quad (5.27)$$

The histogram  $h(M_{k-1}^{(j)}(z) \circ D_{k-1})$  stands for the previously detected target, and  $h_{0,k-1}$  is the histogram from the time step when the target was detected the last time.

### 5.3 Modified pruning for GM-PHD filter

As the PHD filter propagates the posterior intensity, the number of potential hypotheses exponentially increases. This leads to an enormous increase in memory and computational demands. Pruning techniques become indispensable in mitigating this computational load by selectively discarding less likely hypotheses, allowing for a more focused and efficient tracking process. These pruning mechanisms, guided by predefined thresholds or heuristics, ensure that the computational resources are allocated judiciously, striking a balance between accuracy and computational efficiency in multi-target tracking applications.

Recall that sensors in our work are represented by cameras. Naturally, the detecting algorithms are unable to recognize an object hidden by an obstacle. These obstacles may differ not only in size but also in color. In situations where the color of an obstacle closely matches the surrounding scene, the likelihood of detection remains sufficiently high, increasing the risk that the target may not survive even though it is only hidden. In order to suppress this phenomenon, we introduce a method for modified pruning along with the standard pruning and merging techniques [9].

The most deployed generic method for pruning consists of removing targets with weights below some predefined threshold. Nonetheless, as mentioned before, targets with some history may only be hidden, and it is not desired to remove these targets from the scene. To overcome this issue, we assign each target a tag that represents the state in which the target is likely to occur,

$$S = \{\text{detected, hidden, dead}\}.$$

This tag is modeled by a discrete-time Markov chain with the transition matrix

$$P = \begin{bmatrix} p_{D,k} & 1 - p_{D,k} & 0 \\ p_{D,k} & (1 - p_{H,k}^{T_H}) \cdot (1 - p_{D,k}) & p_{H,k}^{T_H} \cdot (1 - p_{D,k}) \\ p_{D,k} & (1 - p_{H,k}^{T_H}) \cdot (1 - p_{D,k}) & p_{H,k}^{T_H} \cdot (1 - p_{D,k}) \end{bmatrix}, \quad (5.28)$$

where  $p_{D,k}$  is a generic detection probability, and  $T_H$  is an exponent for controlling probabilities that is set higher in scenarios, where the target color mask is similar to the color mask of the obstacle, or may be set lower otherwise.  $p_{H,k}$  is the probability that the target is removed. This probability is the result of (5.31), where the bounding boxes of the object detector are used. If we denote by  $B_{P,k}^{(j)}$  the bounding box predicted  $T_c$  steps

ahead and by  $B_{S,k}^{(j)}$  the bounding box of the last step  $k$  when the object was detected, then

$$B_{P,k}^{(j)} = B_{P,k-1}^{(j)} + n_k^{(j)} \cdot [v_{x,k}^{(j)}, v_{y,k}^{(j)}, v_{x,k}^{(j)}, v_{y,k}^{(j)}], \quad (5.29)$$

$$B_{S,k}^{(j)} = B_{S,k-1}^{(j)}, \quad (5.30)$$

$$p_{H,k} = S_c \left[ D_k(B_{P,k}^{(j)}), D_k(B_{S,k}^{(j)}) \right], \quad (5.31)$$

where

$$n_k^{(j)} = \begin{cases} T_c & \text{if } k \bmod T_c = 0, \\ 0 & \text{otherwise.} \end{cases} \quad (5.32)$$

$D_k(\cdot)$  is a part of a frame within the bounding box given by  $B(\cdot)$ . With this approach, when a target is most likely in the *hidden* state, the pruning threshold is heuristically lowered to prevent the target removal.

In summary, first we define a birth place in a scene. We call this birth place a spawn point (SP). It is possible to define more spawn points in a scene, depending on the situation. If a target appears at this spawn point, it is initialized, and since it is the first time the target has been seen, the detection probability is a predefined constant. In the next time step, suppose that the target is detected and there is one measurement (originating from this target) in the validation region. Due to the GM-PHD recursion, two new targets arise from the previous target with the state  $\xi$ . One originates from the misdetection possibility and one from the measurement. As we first predict the target's position and covariance matrix, we move the target's mask detected at time  $k - 1$  to  $k$  by its velocity (in case of the CVM model). Then the predicted mask color properties are compared to the mask made from the new measurement from time  $k$ . If nothing unpredictable happens, both masks should occur on a very similar position, thus the color masks' properties should be very similar. In such case, the detection probability is very likely to be high, lowering the weight of the misdetection-born target. As the weight is small, the target is likely to be removed during the pruning step.

If the previously detected target is hidden behind an obstacle and the object detector does not provide any measurement, only misdetection-born target arises. In such case, the mask from the time when the target was lastly detected is compared to the predicted mask that now also contains the obstacle's color properties. Due to using a camera as a sensor, frames at high frame rate are produced. To prevent the loss of significant information, lowering the fps to a minimal rate is not desirable. We lower the fps to 10-30 fps to enhance the dynamics of the scene. However, in a such short time period, the target, e.g. a car, does not move enough. The predicted mask then intersects with the lastly detected target's mask by a considerably huge amount. That is why we define a probability of the target to be hidden (*hidden probability*,  $p_{H,k}$ ) and modify the pruning of components. As the masks are likely to intersect, the detection probability is likely to be high in the first couple of frames, where the target is hidden. It is essential for the target to survive through this time period. The hidden probability is based on the color properties of bounding boxes from the time the target was lastly detected and from the bounding box that is moved  $T_c$  time steps ahead in the direction of the target's velocity.

The moved bounding box reveals the color properties of the obstacle, that are likely to be different from those assigned to the target when it was lastly detected. Then, the hidden probability should be low and the target's state should be in a hidden state, based on (5.28), therefore the pruning threshold is lowered. After the target overtakes the obstacle, it should appear in a scene and be detected again. If it does not and the color properties of a scene given by the moving bounding box differ from the ones captured when the target was lastly detected, the hidden probability is high and the target is in a dead state. The pruning threshold is not lowered and the detection probability is low, so the target is removed during the pruning step.

## 5.4 Merging in GM-PHD filter with dynamic detection probability

Another way to lower the computational demands and to potentially increase the robustness of a filter is through merging of the targets that appear in the same neighbourhood. This procedure is especially useful in situations when many measurements occur in a validation region of a target. If at least some of these measurements originate from clutter, the target count increases rapidly due to the GM-PHD recursion, increasing the computational requirements. To prevent this issue, the target merging technique is necessary. In the GM-PHD filter, each target carries three variables: the target's weight  $w$ , mean  $m$  and a covariance matrix  $P$ . Merging these values of multiple filters is straightforward and is described in [9] and Section 3.4.2.4. However, in our modified GM-PHD filter, each target also holds these information:

- **Current bounding box position:** The bbox in  $xyxy$  format determines current position of an object. This bbox is determined by a bbox given by a measurement  $z$  in the current time step  $k$  in an update step. The target's bbox is shifted in the prediction step in (5.29), thus the target must have been initialized in the past in order to have the current bbox.
- **Current mask:** The current binary mask is given by a measurement  $z$  in the current time step  $k$  in the update step. In order to initialize current mask, it must have been initialized by a measurement in the past. The mask is shifted according to (5.25).
- **Object Stats:** Every new target born in the update step of the GM-PHD filter by a measurement  $z$  from a target with a previous state  $\xi$ , contains a data structure *Object Stats*. This structure is composed of many variables determining the target's history. These variable arise in the update step from a measurement and are useful for calculating the dynamic detection probability in Equations (5.24) - (5.31).
  - **Bounding box position:** This variable in *Object stats* represents a bounding box from the time the target was lastly detected. To calculate  $p_{H,k}$  in (5.31), this and the current bbox are compared.
  - **Mask:** This variable represents the target's mask from the time the target was lastly detected. In (5.24) and (5.26) this mask is compared to the current mask resulting from the prediction step of a target with the previous state  $\xi$ .
  - **Frame:** To compare the color histograms in (5.24) and (5.26), each target contains a frame from the time  $k$  in which it was born.

- **Time stamp:** This is a variable to save the time  $k$  the target was born.
- **Data structure Markov Chain:** This data structure determines the target's state. As the distribution determined by a transition matrix in (5.28) is not stationary, it is necessary to calculate the resulting distribution in every time step.
- **Initial distribution:** To get the target's state, an initial distribution needs to be defined first.
- **Result matrix:** The result matrix is an ongoing outcome of a previous result matrix and a transition matrix, i.e., the result matrix  $R_k = R_{k-1}P^{k-k_0}$ , where  $k_0$  is the time the target was born,  $R_0 = I_3$  and  $I_n$  is the identity matrix of the shape  $n \times n$ .

The merging procedure of the previous information is inspired by the original GM-PHD merging procedure in [9].

The current bounding box merging is straightforward as  $(x_1, y_1)$  and  $(x_2, y_2)$  coordinates defining the bbox are averaged using the targets' weight. Let us define a set  $L$ , which represents a subset of targets to merge into a single target. Then a resulting target's bbox

$$\tilde{B}_k^{(l)} = \frac{\sum_{i \in L} B_k^{(i)} \cdot w_k^{(i)}}{\sum_{i \in L} w_k^{(i)}}, \quad (5.33)$$

where  $w_k^{(i)}$ , is the weight of a target  $i$  is the weighted mean of targets in subset  $L$ . The same procedure is applied to the bounding box in *Object Stats*, i.e., the previous bbox.

The merging of masks is slightly complicated, as we merge targets' masks into a single "average" mask. First, binary masks of targets in the subset  $L$  are converted into *float* data type, then multiplied with targets' weight and divided by the sum of these weights. To get the resulting binary mask, each element of mask

$$\tilde{M}_k^{(l)} = \frac{\sum_{i \in L} M_k^{(i)} \cdot w_k^{(i)}}{\sum_{i \in L} w_k^{(i)}} \quad (5.34)$$

is rounded either to zero or one and the mask is converted to the binary data type.

We have not experimented with complicated merging of frames and time stamps, only argument maxima is used for both values, i.e,

$$\tilde{t}_k^{(l)} = \max_{i \in L} t_k^{(i)}, \quad (5.35)$$

$$\tilde{D}_k^{(l)} = D_k^{(\tilde{t}_k^{(l)})}. \quad (5.36)$$

As the initial distribution is the same for every target, the resulting merged target's initial distribution is only a copy of any target in  $L$ .

The result matrix merging procedure is similar to the bounding box distribution. The resulting matrix

$$\tilde{N}_k^{(l)} = \frac{\sum_{i \in L} N_k^{(i)} \cdot w_k^{(i)}}{\sum_{i \in L} w_k^{(i)}} \quad (5.37)$$

is the "average" result matrix of targets in subset  $L$ .

The pseudo-code algorithm of modified pruning in GM-PHD filter is shown in Algorithm 5.

---

**Algorithm 5** Pseudo-algorithm for pruning in the GM-PHD filter

---

**Require:**  $\{w_k^{(i)}, m_k^{(i)}, P_k^{(i)}, B_k^{(i)}, M_k^{(i)}, B_{OS,k}^{(i)}, M_{OS,k}^{(i)}, t_{OS,k}^{(i)}, D_k^{(i)}, G_{OS,k}^{(i)}, N_{OS,k}^{(i)}\}_{i=1}^{J_k}$ , a truncation threshold  $T$ , a merging threshold  $U$  and a maximum number of allowed Gaussian terms  $J_{max}$ . Set  $l = 0$ , and  $I = \{i = 1, \dots, J_k | w_k^{(i)} > T\}$ .

- 1: **procedure** MERGING OF TARGETS
- 2:   **while**  $I \neq \emptyset$  **do**
- 3:      $l := l + 1$
- 4:      $j := \text{argmax}_{i \in I} w_k(i)$ ,
- 5:      $L := \left\{ i \in I | (m_k^{(i)} - m_k^{(j)})^T (P_k(i))^{-1} (m_k^{(i)} - m_k^{(j)}) \leq U \right\}$ ,
- 6:      $\tilde{w}_k^{(l)} = \sum_{i \in L} w_k^{(i)}$ ,
- 7:      $\tilde{m}_k^{(l)} = \frac{1}{\tilde{w}_k^{(l)}} \sum_{i \in L} w_k(i) x_k^{(i)}$ ,
- 8:      $\tilde{P}_k^{(l)} = \frac{1}{\tilde{w}_k^{(l)}} \sum_{i \in L} w_k^{(i)} (P_k^{(i)} + (m_k^{(l)} - m_k^{(i)}) (m_k^{(l)} - m_k^{(i)})^T)$ ,
- 9:      $\tilde{B}_k^{(l)} = \frac{1}{\tilde{w}_k^{(l)}} \sum_{i \in L} B_k^{(i)} * w_k^{(i)}$
- 10:     $\tilde{M}_k^{(l)} = \text{round}(\frac{1}{\tilde{w}_k^{(l)}} \sum_{i \in L} M_k^{(i)} * w_k^{(i)})$
- 11:     $\tilde{B}_{OS,k}^{(l)} = \frac{1}{\tilde{w}_k^{(l)}} \sum_{i \in L} B_{OS,k}^{(i)} * w_k^{(i)}$  ▷ OS stands for Object Stats
- 12:     $\tilde{M}_{OS,k}^{(l)} = \text{round}(\frac{1}{\tilde{w}_k^{(l)}} \sum_{i \in L} M_{OS,k}^{(i)} * w_k^{(i)})$
- 13:     $\tilde{t}_{OS,k}^{(l)} = \max_{i \in L} t_{OS,k}^{(i)}$
- 14:     $\tilde{D}_{OS,k}^{(l)} = D_k^{(\tilde{t}_{OS,k}^{(l)})}$
- 15:     $\tilde{G}_{OS,k}^{(l)} = G_{OS,k}^{(j)}$  ▷ Initial distribution of Markov process
- 16:     $\tilde{N}_{OS,k}^{(l)} = \frac{1}{\tilde{w}_k^{(l)}} \sum_{i \in L} N_{OS,k}^{(i)} * w_k^{(i)}$
- 17:     $I := I / L$ .
- 18:   **end while**
- 19: **end procedure**
- 20:
- 21: If  $l > J_{max}$  then replace  $\{\tilde{w}_k^{(i)}, \tilde{m}_k^{(i)}, \tilde{P}_k^{(i)}, \tilde{B}_k^{(i)}, \tilde{M}_k^{(i)}, \tilde{B}_{OS,k}^{(i)}, \tilde{M}_{OS,k}^{(i)}, \tilde{t}_{OS,k}^{(i)}, \tilde{D}_{OS,k}^{(i)}, \tilde{G}_{OS,k}^{(i)}, \tilde{N}_{OS,k}^{(i)}\}_{i=1}^l$  by those of the  $J_{max}$  Gaussians with largest weights.
- 22:
- 23: Output:  $\{\tilde{w}_k^{(i)}, \tilde{m}_k^{(i)}, \tilde{P}_k^{(i)}, \tilde{B}_k^{(i)}, \tilde{M}_k^{(i)}, \tilde{B}_{OS,k}^{(i)}, \tilde{M}_{OS,k}^{(i)}, \tilde{t}_{OS,k}^{(i)}, \tilde{D}_{OS,k}^{(i)}, \tilde{G}_{OS,k}^{(i)}, \tilde{N}_{OS,k}^{(i)}\}_{i=1}^l$  as pruned Gaussian components.

---

# Chapter 6

## Experiments

In order to demonstrate the efficacy of the proposed method for estimating the detection probability, numerous experiments were conducted. This section meticulously examines each of these experiments, delineating the selected parameters and conducting a comparative analysis against the GM-PHD filter with constant detection probability. Experiments were performed using three video footages.

- **V1:** This video shot by a camera from a highway was downloaded from YouTube. The link of this video: youtube.com
- **V2:** The source of the next video is YouTube as well. It captures a common traffic. The link of this video: youtube.com
- **V3:** To get a video of a traffic with an obstacle in the view of the camera, we recorded our own video. This video has been taken in Kartouzská street, Prague.

The CVM model is used as a state-space model in all experiments, i.e., the state  $x_k = [p_{x,k}, p_{y,k}, v_{x,k}, v_{y,k}]^T$  of each target consists of two-dimensional position ( $p_{x,k}, p_{y,k}$ ) and velocity ( $v_{x,k}, v_{y,k}$ ). The measurement is the center of the mask of the detected object, which is typically noisy. The survival probability of the targets  $p_{S,k} = 0.99$ . The state evolution model (3.33) is employed with

$$F_k = \begin{bmatrix} I_2 & \Delta I_2 \\ 0_2 & I_2 \end{bmatrix}, \quad Q_k = \sigma_v^2 [\Delta I_4], \quad (6.1)$$

where  $I_n$  and  $0_n$  denote the  $n \times n$  identity and zero matrices respectively and  $\Delta = 1$  is the sampling period. For every experiment, different parameters for the model have to be applied. Parameters like  $P, \sigma_v$  are displayed in the corresponding tables.

The measurement follows the observation model (3.34) with  $H_k = [I_2, 0_2]$ ,  $R_k = \sigma_\epsilon^2 I_2$ , where  $\sigma_\epsilon$  is the standard deviation of the measurement noise.  $I_2$  and  $0_2$  stand for the  $2 \times 2$  identity and zero matrices, respectively. The standard deviation  $\sigma_\epsilon$  is displayed in the tables as well.

Since the experiments compare the proposed method for estimating the dynamic detection probability with the constant detection probability, each table contains additional

information about the necessary parameters. For experiments that use the constant detection probability, the tables carry the value of the probability. For the dynamic detection probability, the values of  $T_H, T_C$  from Equation (5.24), and initial  $p_{D,k}(x)$  are provided.

The pruning thresholds are the same for both GM-PHD filters, however, in the experiments that apply a filter with the dynamic detection probability, the tables include the second pruning threshold for pruning targets with a *detected* or a *hidden* state. The basic pruning threshold is covered in the tables as  $T_p$ , the lowered pruning threshold as  $T_l$ .

In addition, the object detectors' results are dependent on the thresholds as well. The YOLO model requires the confidence threshold  $T_{YOLO}$  for objects visualization. The Grounding DINO model requires two thresholds as it detects objects based on a text input. The text input threshold  $T_{text}$  and the bounding box (bbox) threshold  $T_{bbox}$  for the given experiment are included in corresponding parameter settings tables.

The labels above the targets in the figures are the numerical representations of the state targets: 0 = detected, 1 = hidden, 2 = dead. The means of the birth places are roughly in the middle of the traffic lines and its confidence ellipses of the size of three standard deviations are bounded by the blue ellipses. The red bounding boxes in the figures represent the bounding boxes given by an object detection model. The red ellipses are the covariance matrices of the targets.

## 6.1 E1: Traffic without any obstacle

The first experiment focuses on the comparison of the GM-PHD filter with the constant detection probability and the GM-PHD filter with the dynamic detection probability with different settings explained in Section 5.1. To analyze if our proposed method works in common scenarios, videos do not include any obstacle, thus the targets are constantly visible.

### 6.1.1 V1

The video *V1* is recorded at 29 fps. For simplicity, only the detections of the right side of the traffic lanes are taken into the account. Figures in Experiments E1-V1 – E1-V3 show frames 36-79 of the video *V1*, as they include some interesting situations.

### 6.1.2 V1 – GM-PHD with the constant detection probability

The measurements for the GM-PHD filter with the constant detection probability are obtained by the YOLO object detection model. The parameters' values are displayed in Table 6.1.

$P_D$	$P$	$\sigma_v$	$\sigma_\epsilon$	$T_p$	$T_{YOLO}$
0.9	diag(600, 600, 600, 600)	0.1	150	0.1	0.3

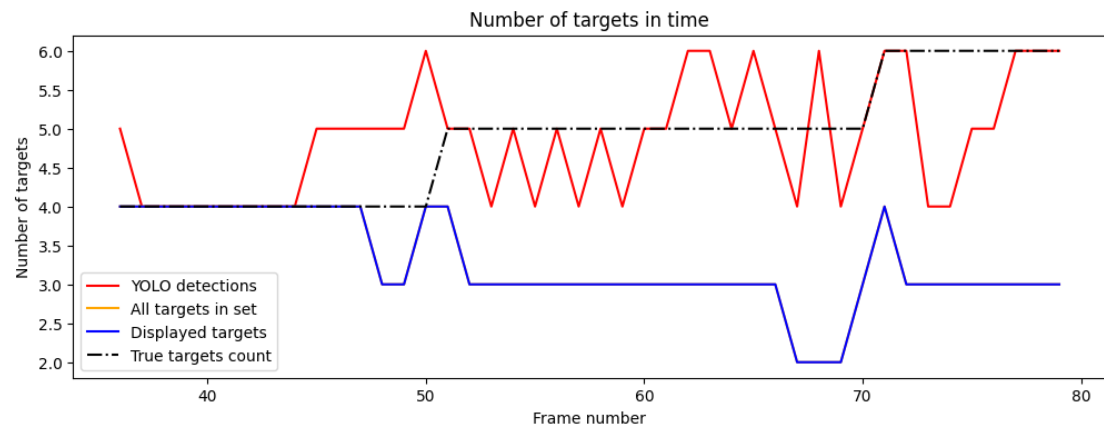
■ **Table 6.1** The parameter settings for Experiment E1-V1 with the constant detection probability.

Figure 6.2 shows some highlights of the GM-PHD filter with the constant detection probability.

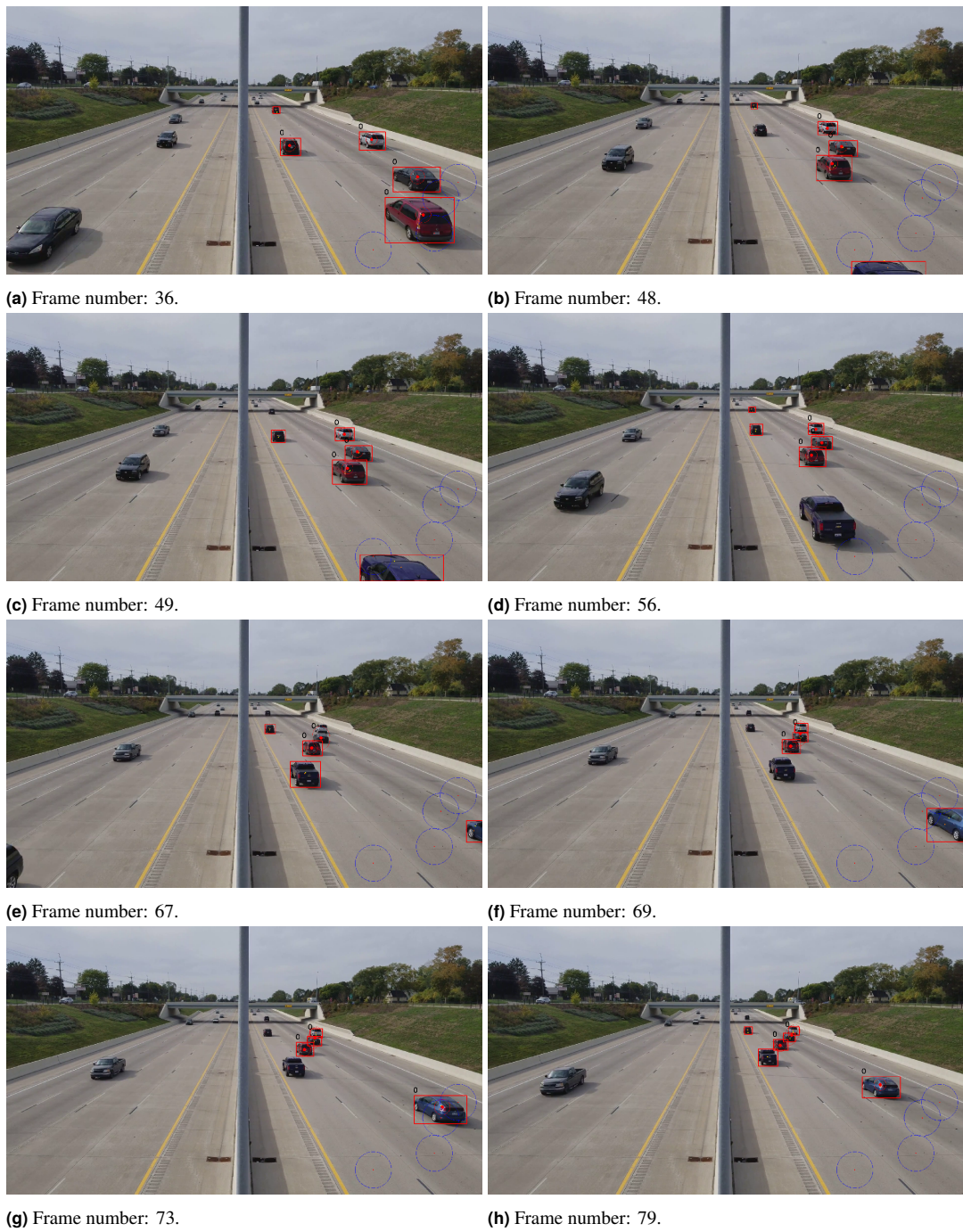
- **6.2a:** This frame marks the initial state, where four cars have been previously identified, thus representing our observed targets. In the distance, YOLO detects another car which, however, has not yet crossed any spawning point, so it is not included in the observed targets set.
- **6.2b:** A new car approaches the scene and is expected to be initialized soon. The YOLO model, although overall reliable, occasionally misses certain objects, as demonstrated here with the car on the left. With a detection probability of 0.9, this target is pruned from the set and considered lost.
- **6.2c:** The previously lost car is, once again, detected. However, it no longer falls within the set of observed targets.
- **6.2d:** Even though the newly arrived car has crossed the spawning point, the YOLO model consistently fails to detect it over several frames, resulting in its complete absence from tracking.
- **6.2e:** The two cars on the right evade the detection. On this occasion, one of the targets manages to persist, allowing for continued tracking of at least one car.
- **6.2f:** The previously undetected cars reappear in the frame. Both cars are successfully tracked once again.
- **6.2g:** Another car enters the scene and is promptly detected and initialized.
- **6.2h:** Despite YOLO detecting all the six cars, only three targets are visible in the scene. One of the targets encompasses two cars simultaneously, indicating that the GM-PHD filter effectively covers four out of the six targets.

In Figure 6.1 it is clearly seen that even though the number of targets is increasing, the misdetection of the YOLO model causes the targets' loss. The "All targets in set" line is fully covered by the blue line, thus the targets are permanently lost and can not be reborn by a measurement.

This experiment shows that the GM-PHD filter is able to accurately track the position of objects. With the detection probability  $p_D = 0.9$  and without the modified pruning technique, the filter is very sensitive to the capability of the object detector and if YOLO is not able to detect all the desired objects, targets can be easily lost.



■ **Figure 6.1** Development chart of number of detected targets, targets in the filter's queue, displayed targets and the true targets' count.



■ **Figure 6.2** Image sequence of tracked objects using the GM-PHD filter with the constant detection probability.

### 6.1.3 V1 – GM-PHD with the dynamic detection probability

The following experiments test the GM-PHD filter with the dynamic detection probability and the modified pruning in the video *V1*.

### 6.1.3.1 S1 – YOLO + YOLO

This experiment enhances settings  $S1$ , i.e., the YOLO model provides both object detection bboxes and segmentation masks. The parameter settings are shown in Table 6.2.

$P_{D,k}(x)$	$P$	$\sigma_v$	$\sigma_\epsilon$	$T_H$	$T_d$	$T_p$	$T_l$	$T_{YOLO}$
0.3	diag(600, 600, 600, 600)	0.1	150	1	3	0.1	0.01	0.3

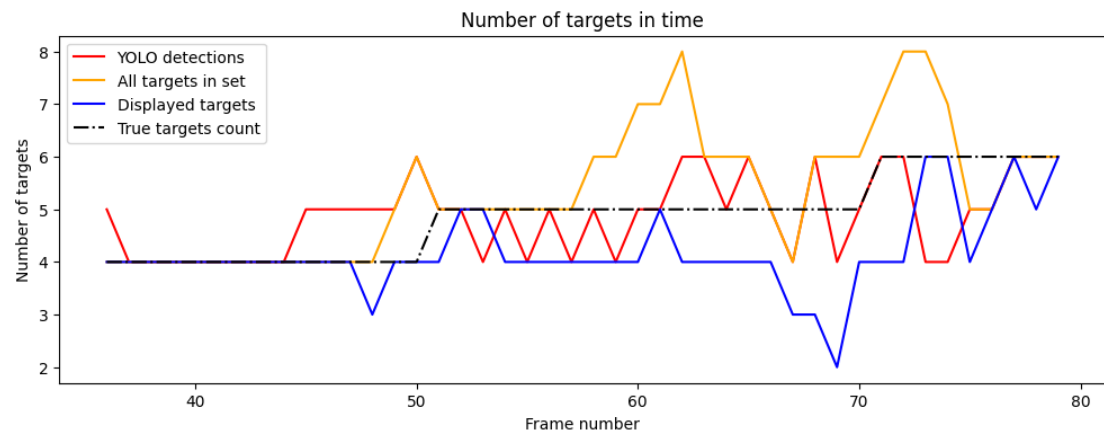
■ **Table 6.2** The parameter settings for Experiment E1-V1-S1 with the dynamic detection probability.

Figure 6.4 illustrates the performance of the GM-PHD filter under the dynamic detection probability and settings  $S1$ .

- **6.4a:** Similarly as in the previous experiment, the initial frame presents four previously detected cars. Although a distant car is detected, it remains uninitialized since it has not crossed any spawning point.
- **6.4b:** By frame 48, the car on the left, which was undetected in the previous experiment, remains so. However, due to the elevated detection probability and adjusted pruning, the target manages to persist.
- **6.4c:** Despite the previous misdetections, the previously undetected car is once again identified, and the target successfully survives.
- **6.4d:** A new car crosses the spawning point, yet the YOLO model consistently fails to detect it over numerous consecutive frames, resulting in its non-initialization.
- **6.4e:** Two cars on the right evade the detection, yet their respective targets remain.
- **6.4f:** The previously undetected cars are once again identified, and both targets receive measurements, augmenting their weights.
- **6.4g:** Another car enters the scene and is successfully initialized.
- **6.4h:** The previously undetected car on the left merges with other targets. Consequently, this target is initialized despite the previous frequent misdetections. As a result, six true targets and six tracked targets are present.

The graph presented in Figure 6.3 shows the enhanced performance of the GM-PHD filter. While all targets do not immediately appear in the scene upon detection, they often still exist in the queue of targets whose weights have not reached a threshold for display. However, upon receiving measurements, these targets' weights increase, leading to their reappearance in the scene.

This improvement is notable not only in the alignment of displayed targets with the true target count, but also in the queue of potential targets exceeding the true count. Consequently, we gain awareness of potential targets that may manifest in the scene.



■ **Figure 6.3** Development chart of the number of detected targets, targets in the filter's queue, displayed targets and the true targets' count.

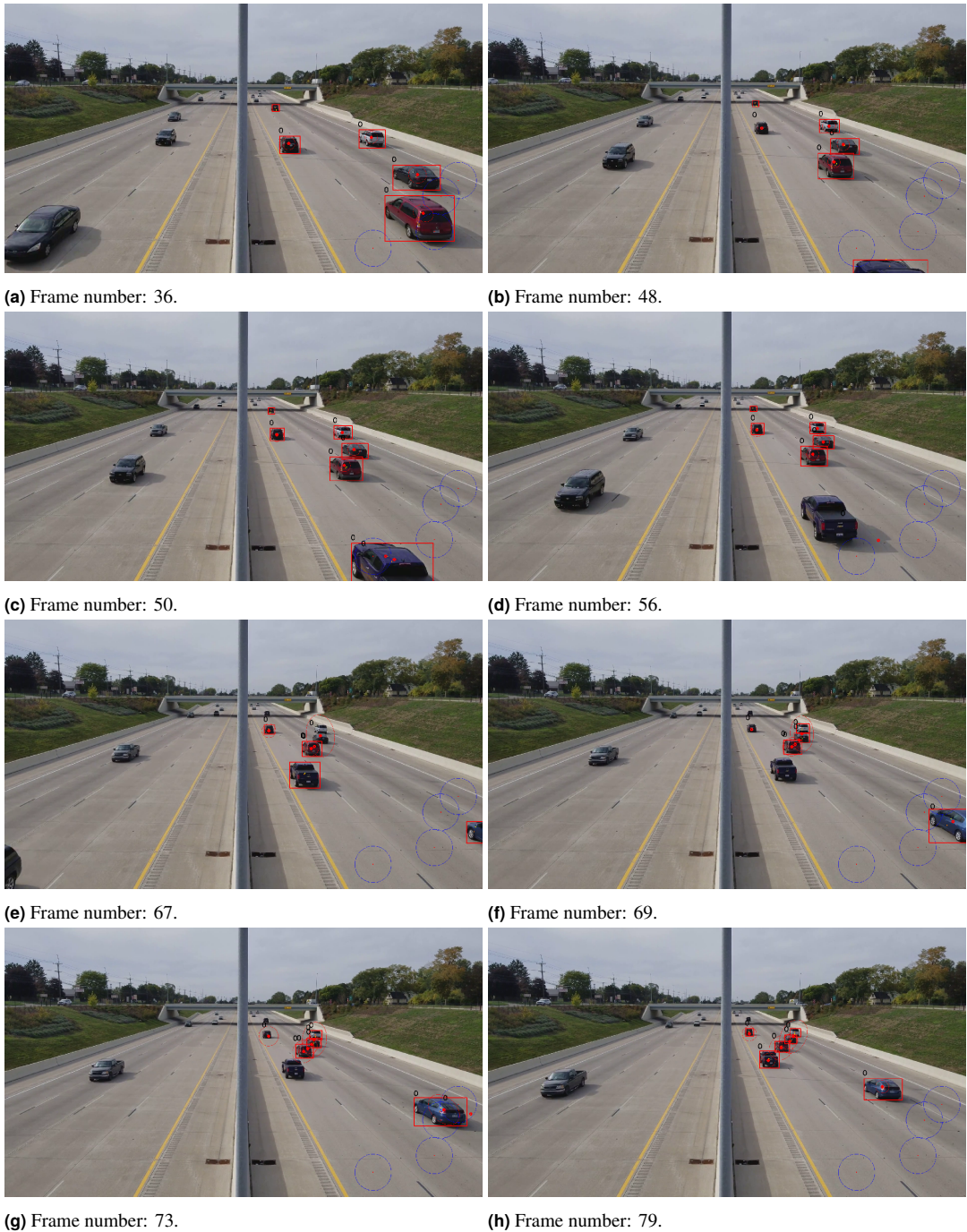


**Figure 6.4** Image sequence of tracked objects using the GM-PHD filter with the dynamic detection probability and YOLO only.

### 6.1.3.2 S2 – YOLO + SAM

This experiment employs configuration *S2*, wherein the YOLO model furnishes objects' bounding boxes and the SAM model furnishes segmentation masks. The parameter configurations can be found in Table 6.3.

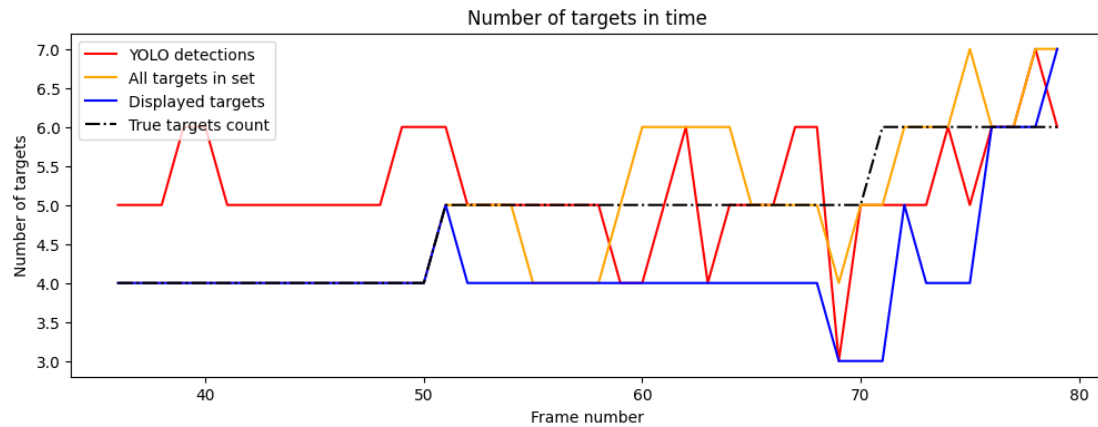
$P_{D,k}(x)$	$P$	$\sigma_v$	$\sigma_\epsilon$	$T_H$	$T_d$	$T_p$	$T_l$	$T_{YOLO}$
0.3	diag(600, 600, 600, 600)	0.1	150	1	3	0.1	0.01	0.3

■ **Table 6.3** The parameter settings for Experiment E1-V1-S2 with the dynamic detection probability.

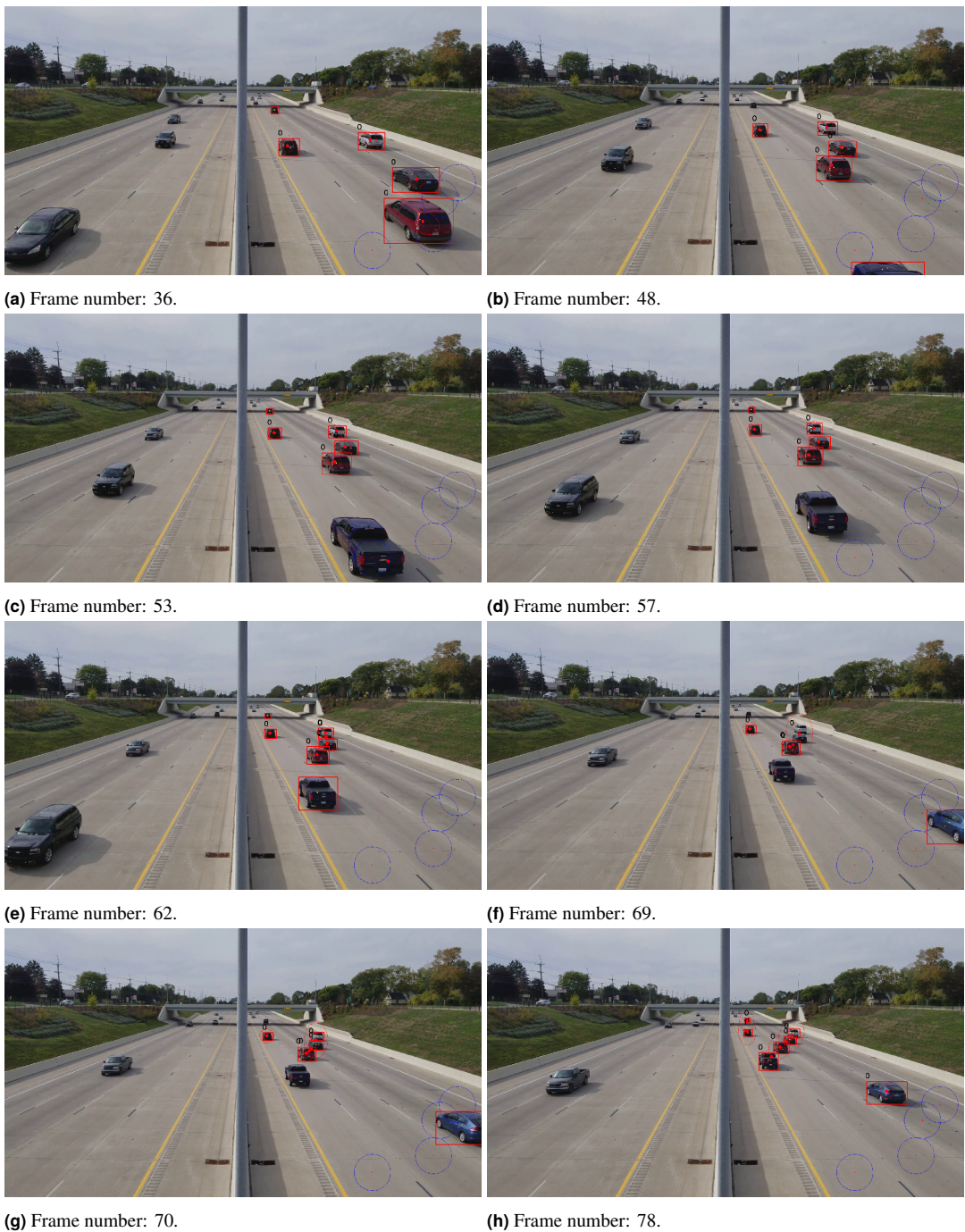
Figure 6.6 illustrates the GM-PHD filter's performance with the dynamic detection probability, employing settings *S2*. This sequence is very similar to the previous experiment. There are four targets at the beginning and they are tracked successfully the whole time. In the frame 6.6f two of the targets are not detected, but both survive. The YOLO model is not able to detect the fifth car, but it is initialized later due to the other target.

Figure 6.5 shows a better stability in keeping the number of tracked targets. This might be caused by the fact, that the object detection YOLO model gives slightly different results than the object detection YOLO model with segmentation capabilities. Furthermore, the "All targets in set" orange line, representing the number of targets in the filter's queue, is more accurate to the true count, deflecting only by one target at maximum.

Settings *S2* perform manage a slightly better performance than settings *S1*. The number of tracked objects is closer to the true count.



■ **Figure 6.5** Development chart of the number of detected targets, targets in the filter's queue, displayed targets and the true targets' count.



**Figure 6.6** Image sequence of tracked objects using the GM-PHD filter with the dynamic detection probability, the YOLO object detector and the SAM image segmentation model.

### 6.1.3.3 S3 – Grounded SAM

The experiment with settings *S3* uses Grounding DINO object detector and the SAM image segmentation model. All used parameters are included in Table 6.4.

$P_{D,k}(x)$	$P$	$\sigma_v$	$\sigma_\epsilon$	$T_H$	$T_d$	$T_p$	$T_l$	$T_{text}$	$T_{bbox}$
0.3	diag(600, 600, 600, 600)	0.1	150	1	3	0.1	0.01	0.3	0.3

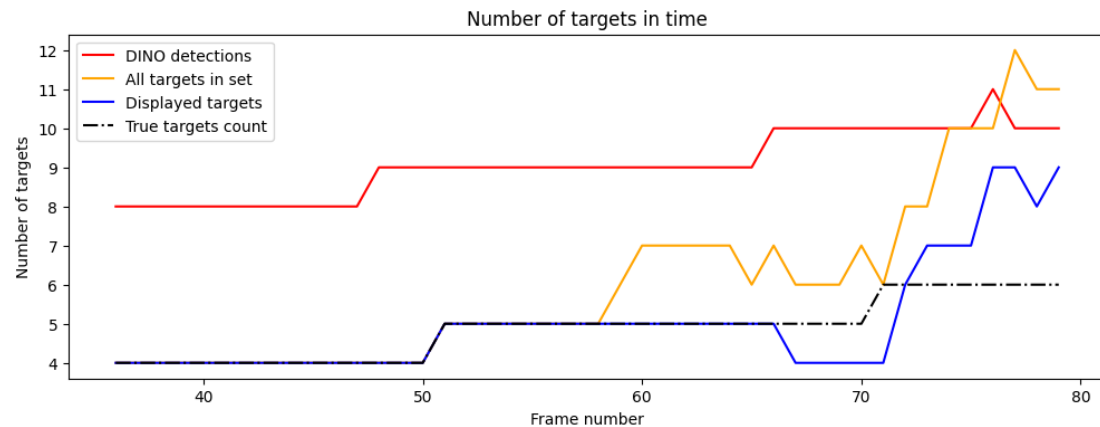
■ **Table 6.4** The parameter settings for Experiment E1-V1-S3 with the dynamic detection probability.

Figure 6.8 shows the performance of the GM-PHD filter with the dynamic detection probability with settings S3.

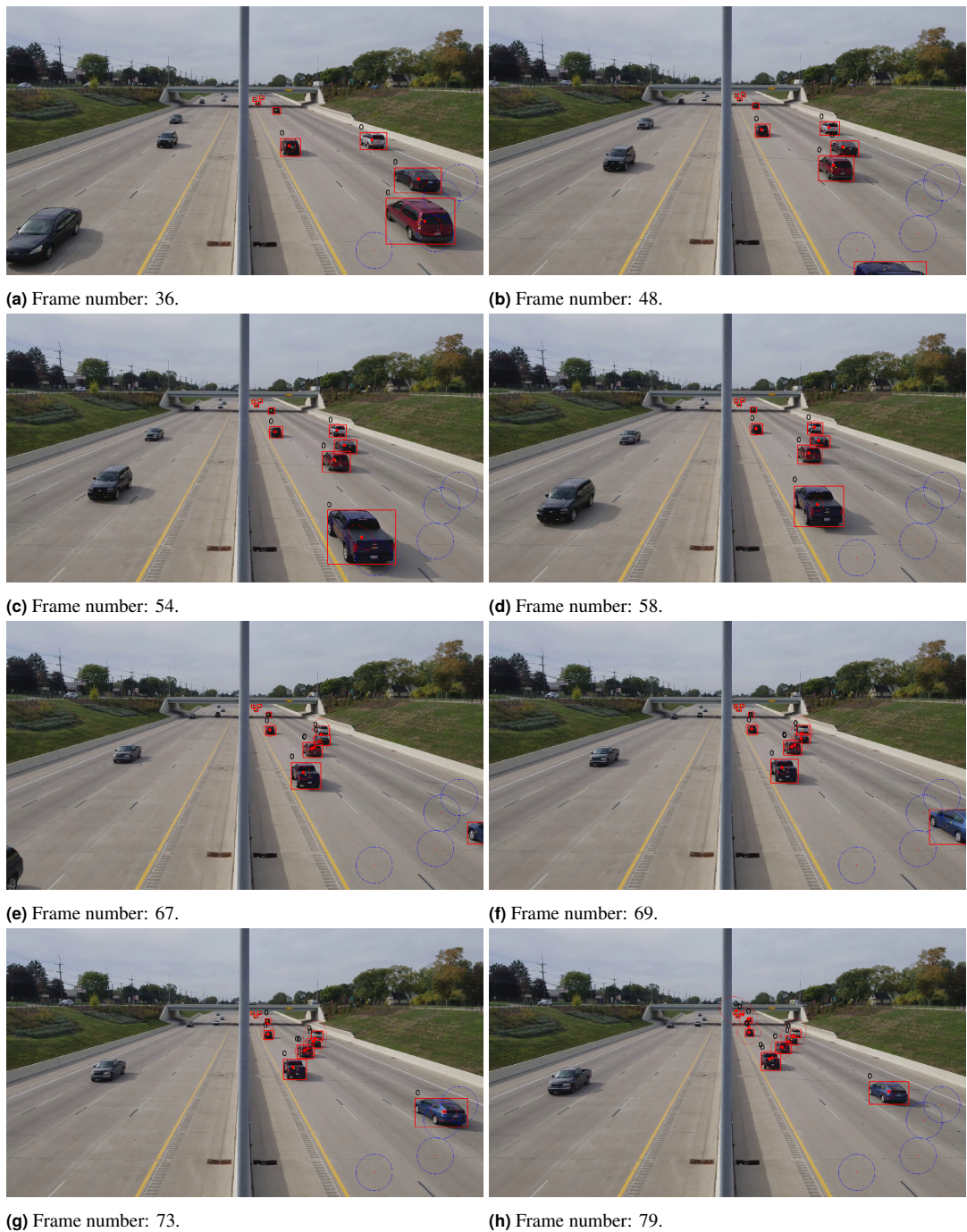
- **6.8a:** The utilization of a distinct object detection model results in an increased number of cars detected within the scene. However, only the four cars in the front have driven through the spawn points thus are considered within the true count.
- **6.8b:** All targets are effectively tracked without any issues.
- **6.8c:** Unlike YOLO, Grounding DINO successfully detects the arrival of a new car.
- In **6.8d, 6.8e, 6.8f** no events of greater importance occur.
- **6.8g:** Subsequently, the following arriving car is promptly detected and initialized.
- **6.8h:** This frame presents new challenges. Given the decreased distance between the cars and their proximity to each other, coupled with the model's ability to detect all of the cars, an excess of new targets emerges. To address this issue, adjustments to the motion noise are necessary. Additionally, for such scenarios, the implementation of the dynamic motion noise and the observation noise could offer a viable solution.

Figure 6.7 shows, that the number of detected objects is far beyond the true count. Nevertheless, the number of displayed targets is almost on spot till the frame 66. As the targets get closer to each other, the number of targets grows rapidly, causing errors to the number of tracked objects.

This setting outperforms the other settings. The performance of Grounding DINO brings another problems arising from characteristics of the video. The video is taken from an angle, which makes the cars smaller as they carry on. These dynamics align poorly with the static motion and the observation noise.



■ **Figure 6.7** Development chart of the number of detected targets, targets in the filter's queue, displayed targets and the true targets' count.



**Figure 6.8** Image sequence of tracked objects using the GM-PHD filter with the dynamic detection probability and the Grounded SAM model.

#### 6.1.4 V2

Video V2 is recorded at 29 fps. Only the cars driving from the left to the right are detected and tracked. In the following experiments frames 83-109 of the video V2 are analyzed.

### 6.1.5 V2 – GM-PHD with the constant detection probability

The measurements for the GM-PHD filter with the constant detection probability are obtained by the YOLO object detection model. The parameters' values are displayed in Table 6.5.

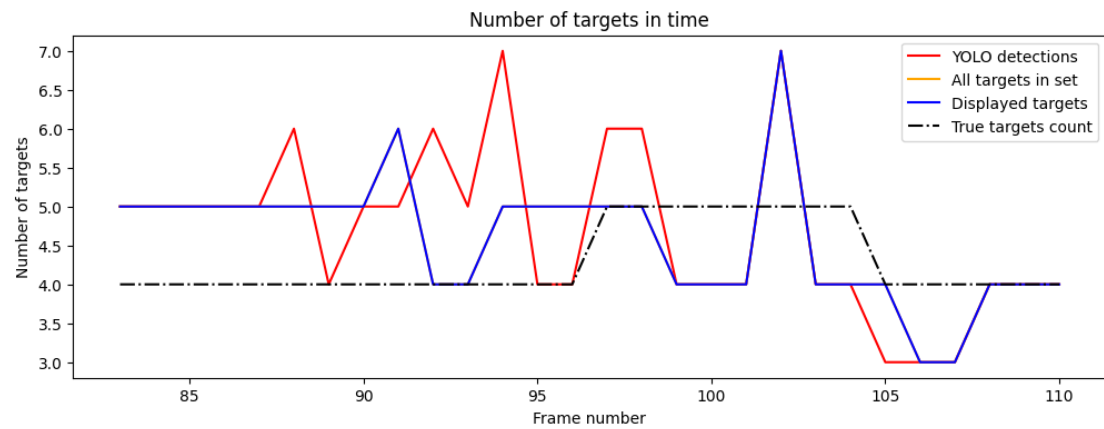
$P_D$	$P$	$\sigma_v$	$\sigma_\epsilon$	$T_p$	$T_{YOLO}$
0.9	diag(100, 100, 100, 100)	0.1	30	0.1	0.3

■ **Table 6.5** The parameter settings for Experiment E1-V2 with the constant detection probability.

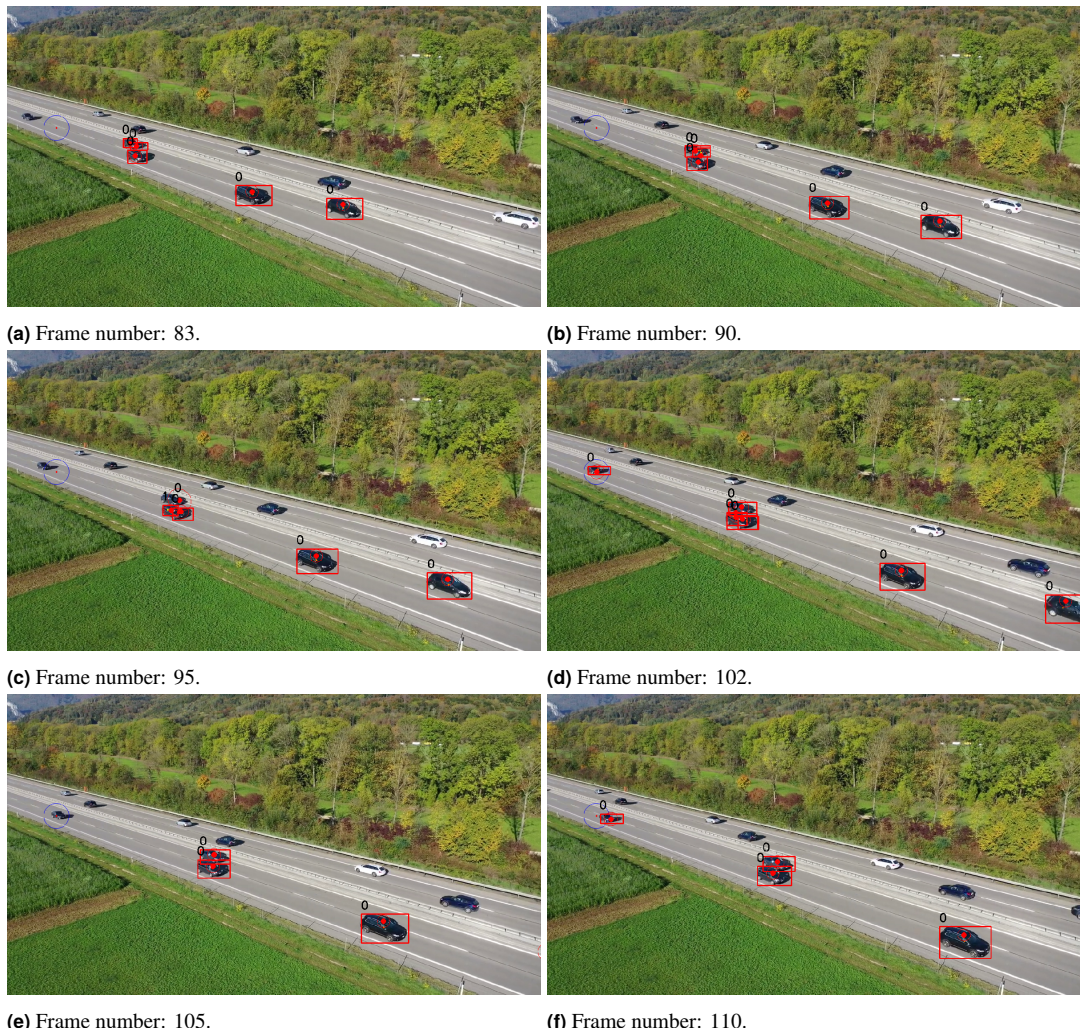
Figure 6.10 displays the performance of the GM-PHD filter with the constant detection probability.

- **6.10a:** The sequence begins with the frame number 83, wherein four targets have already been initialized and successfully detected.
- **6.10b:** Notably, the objects appear relatively small in comparison to the overall frame size. This size discrepancy contributes to a phenomenon where targets in a close proximity share measurements, resulting in the appearance of additional targets in the scene.
- **6.10c:** Despite the YOLO model failing to detect the fourth car, the target persists within the tracking system.
- **6.10d:** The previously undetected car is successfully identified once more, and the tracking of the target continues. Additionally, another car approaches the spawning point.
- **6.10e:** Regrettably, the car within the spawning area remains undetected and has not survived, probably due to its weight being insufficient to ensure survival. Concurrently, the first car exits the scene.
- **6.10f:** Subsequently, the car at the spawning point is detected once again and remains sufficiently close to be initialized as a target. The scene concludes with four true objects and four accurately tracked targets.

The GM-PHD filter with the constant detection probability is accurate in scenarios, where the object detector does not miss detections regularly. Figure 6.9 shows that the number of displayed targets is close enough to the true count. Even false detections created by YOLO did not mislead the filter.



■ **Figure 6.9** Development chart of the number of detected targets, targets in the filter's queue, displayed targets and the true targets' count.



■ **Figure 6.10** Image sequence of tracked objects using the GM-PHD filter with the constant detection probability.

### 6.1.6 V2 – GM-PHD with the dynamic detection probability

Experiments carried out on the video V2 using the GM-PHD filter with the dynamic detection probability and different settings are demonstrated in following sections.

#### 6.1.6.1 S1 – YOLO + YOLO

This experiment uses settings *S1*, where the YOLO model provides both object detection bboxes and segmentation masks. The parameter settings are shown in Table 6.6.

$P_{D,k}(x)$	$P$	$\sigma_v$	$\sigma_\epsilon$	$T_H$	$T_d$	$T_p$	$T_l$	$T_{YOLO}$
0.3	diag(600, 600, 600, 600)	0.1	30	1	3	0.1	0.01	0.3

■ **Table 6.6** The parameter settings for Experiment E1-V2-S1 with the dynamic detection probability.

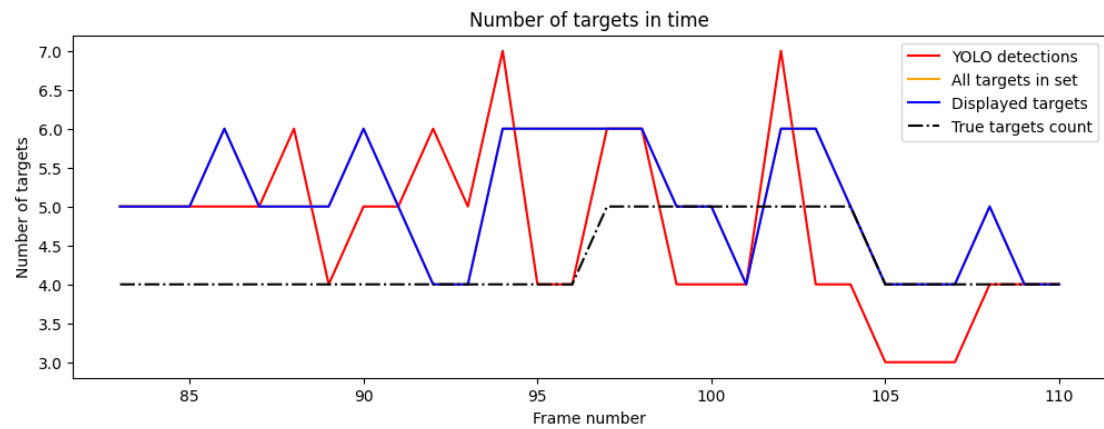
Figure 6.12 shows the performance of the GM-PHD filter with the dynamic detection probability with settings *S1*.

- **6.12a:** Analogously to the previous analysis, four targets have surpassed the spawning point and are tracked by the GM-PHD filter. The targets' presence in the close proximity results in an additional false targets' existence.
- **6.12b:** The problem of targets' neighboring persists.
- **6.12c:** Moreover, the YOLO model classifies the targets' shadows as another cars, causing the initialization of extra targets.
- **6.12d:** A new car crosses the spawning point, yet the YOLO model fails to detect it.
- **6.12e:** The new car has been previously detected and initialized. The two neighbouring cars still generate additional false targets.
- **6.12f:** Finally, there appear only two targets representing the two cars. The other two cars are tracked properly.

Figure 6.11 depicts a similar performance of the GM-PHD filter with the dynamic detection probability as the GM-PHD filter with the constant detection probability. The number of displayed targets exceeds the true number of targets due to already presented reasons.

The improved ability of the target's survival resulted in a slightly decreased the overall tracking performance. The YOLO model has been able to detect tracked objects flawlessly, which leads to needlessness of the dynamic detection probability and modified pruning method enabling enhanced targets' ability to survive.

However, the goal of this experiment is to examine the tracking capability of the GM-PHD filter with the proposed dynamic detection probability in common flawless scenarios. This experiment verifies the method to be sufficient.



■ **Figure 6.11** Development chart of the number of detected targets, targets in the filter's queue, displayed targets and the true targets' count.

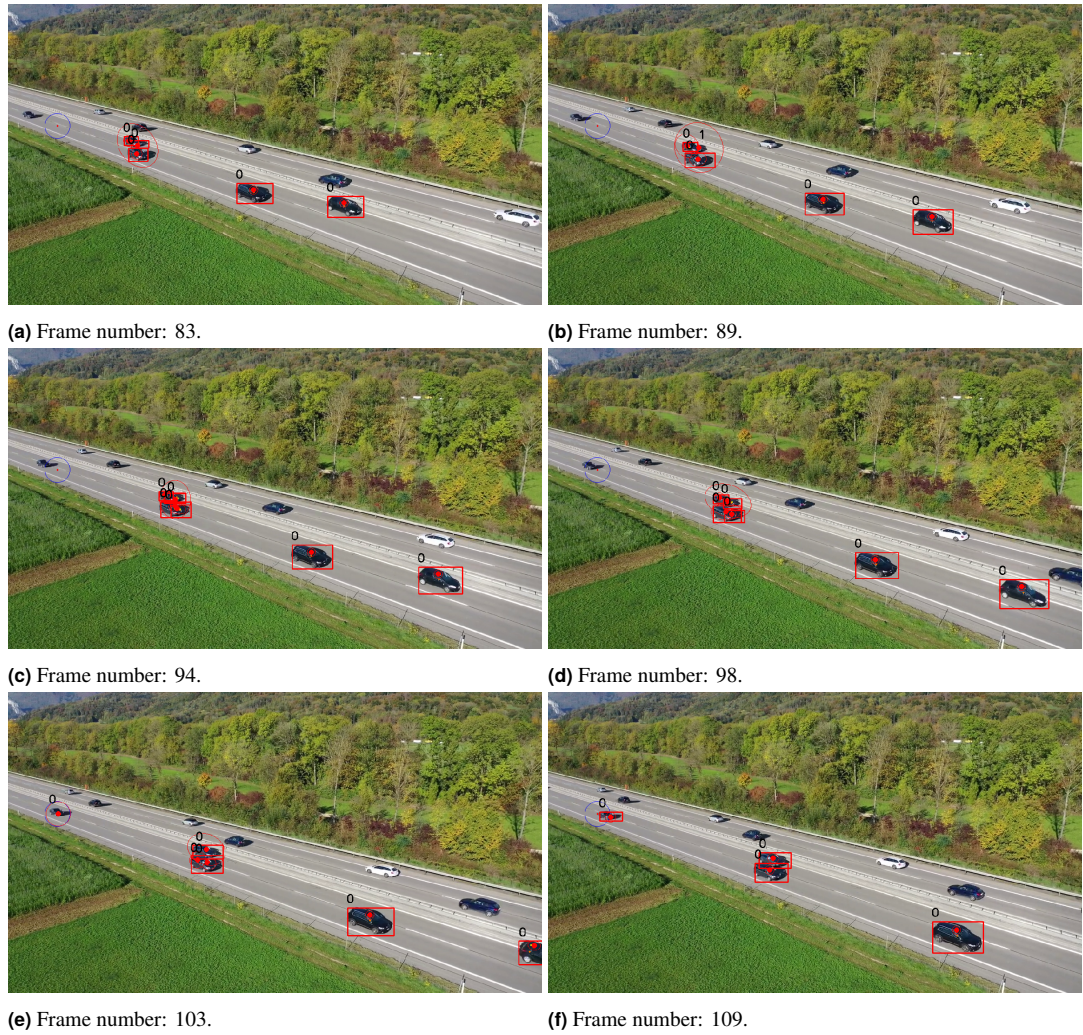


**Figure 6.12** Image sequence of tracked objects using the GM-PHD filter with the dynamic detection probability and YOLO only.

### 6.1.6.2 S2 – YOLO + SAM

As in experiment *E1*, the next settings employs *S2* with the YOLO object detector and the SAM segmentation model. All parameters are included in Table 6.7.

$P_{D,k}(x)$	$P$	$\sigma_v$	$\sigma_\epsilon$	$T_H$	$T_d$	$T_p$	$T_l$	$T_{YOLO}$
0.3	diag(100, 100, 100, 100)	0.1	30	1	3	0.1	0.01	0.3

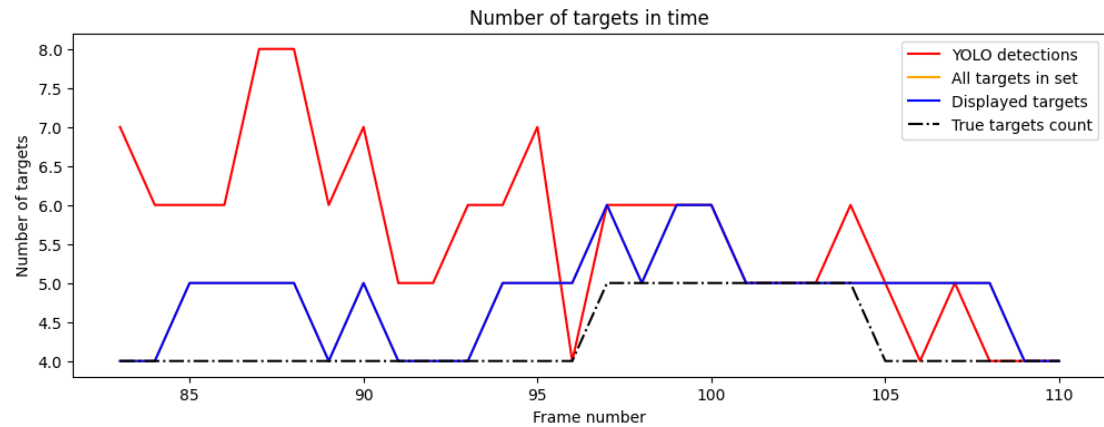
**Table 6.7** The parameter settings for Experiment E1-V2-S2 with the dynamic detection probability.

The situation resembles the situation with settings *S1*. Four targets occur in Figure 6.14a. They continue in their path while all targets are tracked successfully with one exception. No additional targets appear in the subsequent frames. The YOLO model detects a car's shadow and classifies it as another car, which makes the added target in Figure 6.14c. Due to the merging step, this false target does not survive to the subsequent

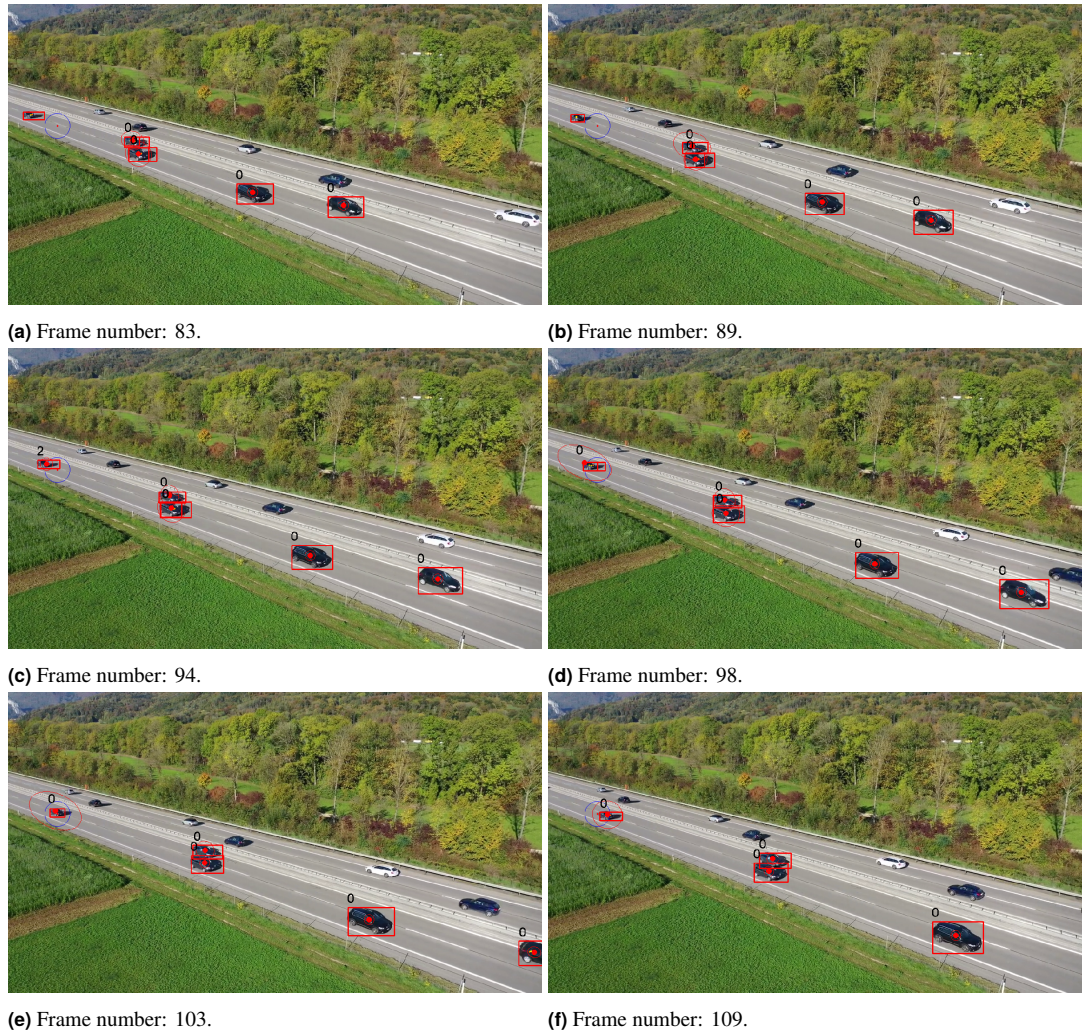
frames. A new car is initialized in Figure 6.14d. All targets are tracked in the last frames.

The number of displayed targets is close to the true number of targets in Figure 6.13. The number of detected targets exceeds the number of true targets for majority of the time, due to the presence of false detections.

Settings *S2* exhibit a slight improvement over settings *S1*, which is reflected in the reduced error between the number of displayed targets and the true count.



■ **Figure 6.13** Development chart of the number of detected targets, targets in the filter's queue, displayed targets and true targets' count.



■ **Figure 6.14** Image sequence of tracked objects using the GM-PHD filter with the dynamic detection probability, the YOLO object detector and the SAM image segmentation model.

### 6.1.6.3 S3 – Grounded SAM

The combination of Grounding DINO and SAM is tested using the video V2 as well. Used parameteres are given in Table 6.8.

$P_{D,k}(x)$	$P$	$\sigma_v$	$\sigma_\epsilon$	$T_H$	$T_d$	$T_p$	$T_l$	$T_{text}$	$T_{bbox}$
0.3	diag(100, 100, 100, 100)	0.1	30	1	3	0.1	0.01	0.3	0.3

■ **Table 6.8** The parameter settings for Experiment E1-V2-S3 with the dynamic detection probability.

Figure 6.16 reveals a better object detection. As a result, the tracking of objects is more precise than in the other settings.

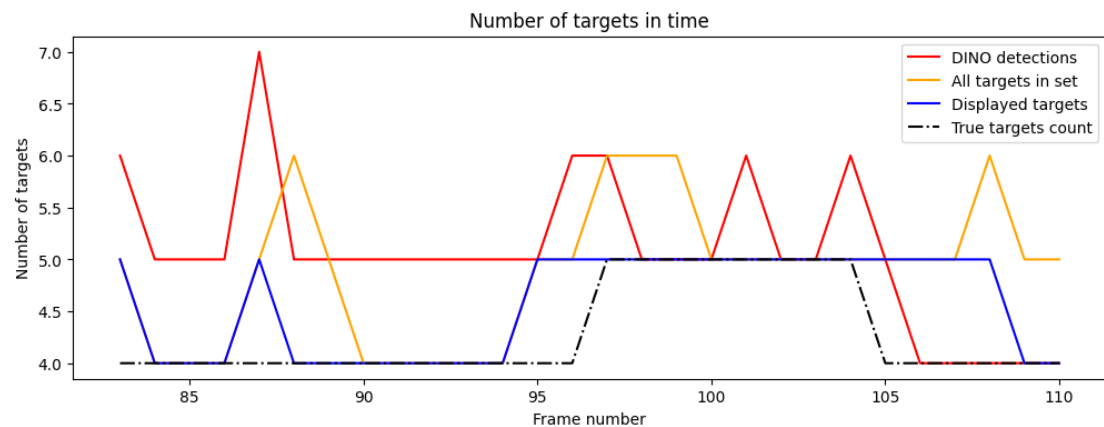
- **6.16a:** Starting with four tracked targets in frame no. 83.
- **6.16b:** As in Experiment E1-V1, the motion and observation noise covariances seem

to be too large for this scenario. The third and the fourth car's measurement reaches the validation region of each other. This situation creates new undesired targets.

- **6.16c:** The exact same situation happens in this frame.
- **6.16d:** Another car reaches the spawning point.
- **6.16e:** Five targets appear in the scene, all of them correctly tracked.
- **6.16f:** The scenario ends with four properly detected and tracked objects.

Even though the two cars driving side by side cause the filter with given parameters a few modest problems, the merging and the pruning steps can usually deal with such situations, as seen in Figure 6.15. The line showing the number of displayed targets almost copies the line showing the true counts. The figure also shows the problem of two neighbouring targets and the problem of false detections. The peaks in the red line show these false detections, the filter remains unaffected and holds the true number of targets.

As in Experiment *E1-VI*, this setting outperform the other settings variations. Moreover, due to the more precise object detection, the filter is able to deal with problems such as two targets appearing in the same neighbourhood or false detections. However, settings *S3* is very sensitive to motion and observation noise parametrization, thus these covariance matrices have to be set carefully.



■ **Figure 6.15** Development chart of the number of detected targets, targets in the filter's queue, displayed targets and true targets' count.

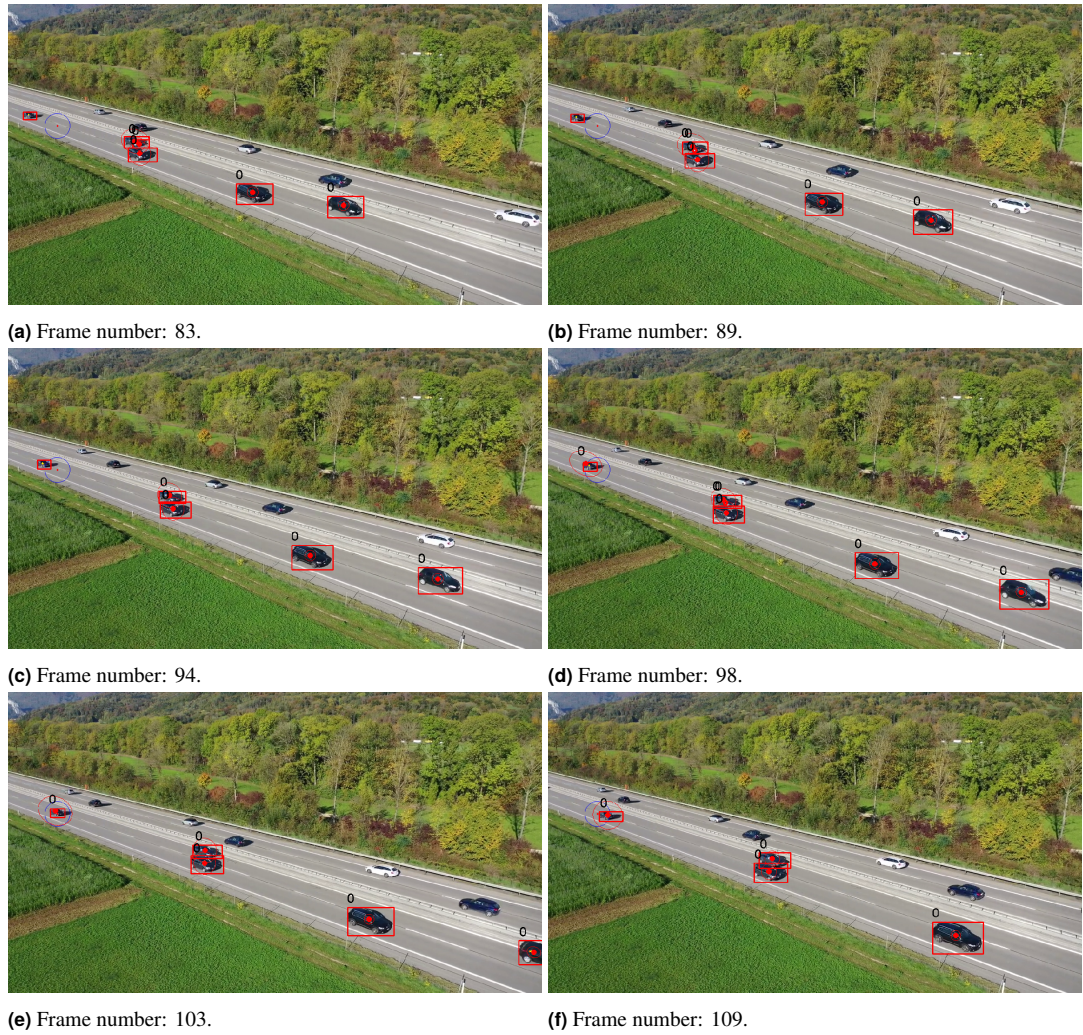


**Figure 6.16** Image sequence of tracked objects using the GM-PHD filter with the dynamic detection probability, the DINO object detector and the SAM image segmentation model.

## 6.2 E2: Traffic with an obstacle

The previous experiment demonstrated the performance of our proposed GM-PHD filter method, which incorporated the dynamic detection probability and the modified pruning. Our method has proven superior to the standard GM-PHD filter with the constant detection probability. Nevertheless, our method was primarily designed to excel in situations where obstacles obscure camera views. To assess its effectiveness in such scenarios, we propose Experiment *E2*.

### 6.2.1 V3

In the video *V3* a light pole is in the camera's view, preventing the object detector to detect hidden objects. The frame rate of this video is set to 10 fps.

### 6.2.2 V3 - GM-PHD with the constant detection probability

The targets cannot persist beyond a certain number of time steps without being measured, resulting in their loss once they surpass an obstacle. To avert a permanent loss, a new spawning point is introduced immediately after the obstacle to revive the lost target. However, this approach comes with a drawback: the revived target starts afresh without retaining its previous history.

Parameter settings are embodied in Table 6.9.

$P_D$	$P$	$\sigma_v$	$\sigma_\epsilon$	$T_p$	$T_{YOLO}$
0.9	diag(500, 500, 500, 500)	0.1	100	0.1	0.3

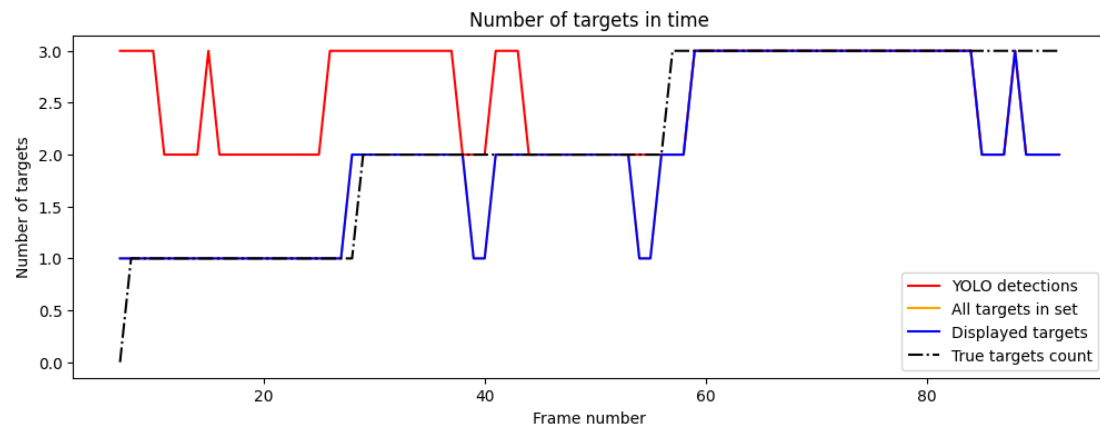
■ **Table 6.9** The parameter settings for Experiment E2-V3 with the constant detection probability.

Figure 6.18 shows some highlights of the GM-PHD filter with the constant detection probability.

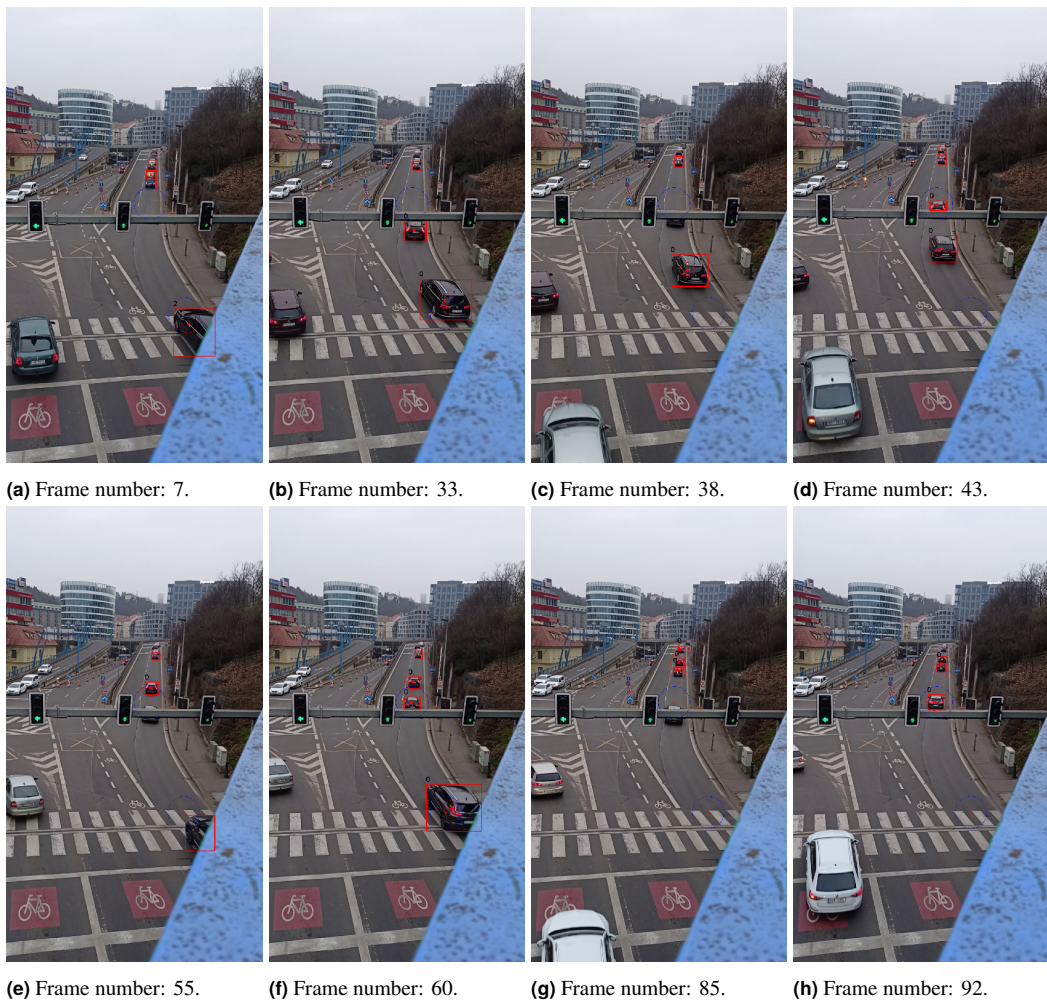
- **6.18a:** The sequence starts with frame no. 7. The first car is initialized by the spawning point.
- **6.18b:** The first car arrives to an obstacle. Meanwhile, the second car arrives.
- **6.18c:** The YOLO object detector is not able to detect the hidden car. The target is removed.
- **6.18d:** The previously lost target is detected and initialized due to the second spawning point. Nevertheless, the history of this target is still lost. Moreover, the target has not been tracked for five consecutive frames.
- **6.18e:** The second car is not detected due to the obstacle. The track of the target is lost.
- **6.18f:** The target is once again initialized by the second spawning point. The third car approaches the first spawning point.
- **6.18g:** The last car is also not detected behind the obstacle, thus its track is lost.
- **6.18h:** Even though the target is reborn, the track of this target has not been available for 6 frames in a row. The other two cars are further away and appear to be in the same neighbourhood. The filter merged these two targets into a single one.

According to Figure 6.17, the filter is able to successfully track the targets. However, the figure also shows the weakness of this approach. The peaks displaying the target's loss are clearly present.

With the second spawn point enabling targets to reborn, the GM-PHD filter is able to track all the targets accurately. The weakness of this approach is definite – if a target is reborn, it is a whole new target without any history.



■ **Figure 6.17** Development chart of the number of detected targets, targets in the filter's queue, displayed targets and true targets' count.



■ **Figure 6.18** Image sequence of tracked objects using the GM-PHD filter with the constant detection probability.

### 6.2.3 V3 – GM-PHD with the dynamic detection probability

Experiments using the video V3 utilizing the GM-PHD filter with the dynamic detection probability and settings  $S1$ ,  $S2$ ,  $S3$  are demonstrated in following sections.

#### 6.2.3.1 S1 – YOLO + YOLO

This experiment uses settings  $S1$ , where the YOLO model provides both object detection bboxes and segmentation masks. The parameter settings are shown in Table 6.10.

$P_{D,k}(x)$	$P$	$\sigma_v$	$\sigma_\epsilon$	$T_H$	$T_d$	$T_p$	$T_l$	$T_{YOLO}$
0.3	diag(500, 500, 500, 500)	0.1	100	2	3	0.1	0.0001	0.3

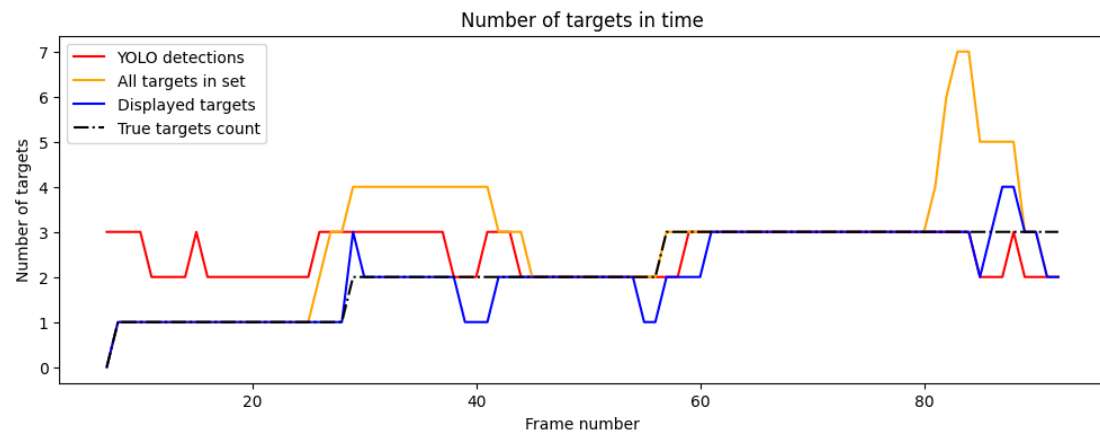
■ **Table 6.10** The parameter settings for Experiment E2-V3-S1 with the dynamic detection probability.

Figure 6.20 shows the performance of the GM-PHD filter with the dynamic detection probability with settings  $S1$ .

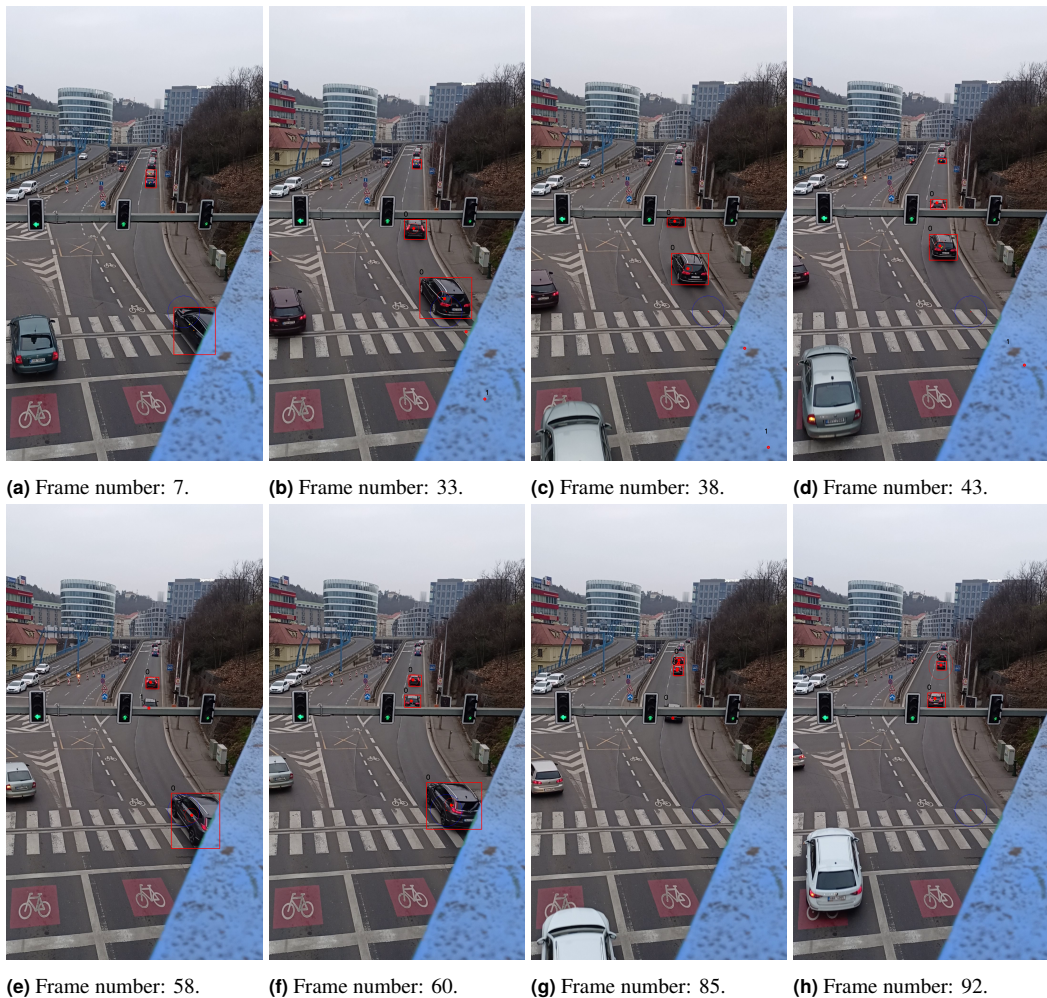
- **6.20a:** The tracking starts with frame no. 7. The first target approaches the spawning point.
- **6.20b:** The first car reaches the light pole. The second car appears in the scene.
- **6.20c:** The first car is detected by YOLO for the last time before temporarily disappearing behind the obstacle.
- **6.20d:** Even though the first car has not been detected for 5 frames, it is able to survive without the second spawning point.
- **6.20e:** In this frame, an example of the *hidden* target's state can be seen. The second car is annotated with number 1, i.e., it is considered as hidden.
- **6.20f:** The second car overcomes the obstacle and continues in its path. This target was able to survive for 6 consecutive time steps.
- **6.20g:** As the two cars appear close to each other, more measurements appear in the validation region of the targets. The third car is not detected behind the light pole, but is still tracked.
- **6.20h:** The first two cars' targets are merged together, due to the long distance from the camera, static motion and observation noises. The third target also survives the misdetection period.

The displayed targets line in Figure 6.19 is almost the same as in previous experiment. However, the orange line shows, that the filter is still informed about all potential targets. As seen in Figure 6.20, the hidden targets are not lost, their weights are just too small to be displayed.

The performance of the GM-PHD filter with the dynamic detection probability might seem to be very similar to the constant detection probability at first glance. But the targets are not removed when hidden. Moreover, the targets' track history is not lost.



■ **Figure 6.19** Development chart of the number of detected targets, targets in the filter's queue, displayed targets and true targets' count.



■ **Figure 6.20** Image sequence of tracked objects using the GM-PHD filter with the dynamic detection probability and YOLO only.

### 6.2.3.2 S2 – YOLO + SAM

The next settings employs settings *S2* with the YOLO object detector and the SAM segmentation model on the video *V3*. All parameters are included in Table 6.11.

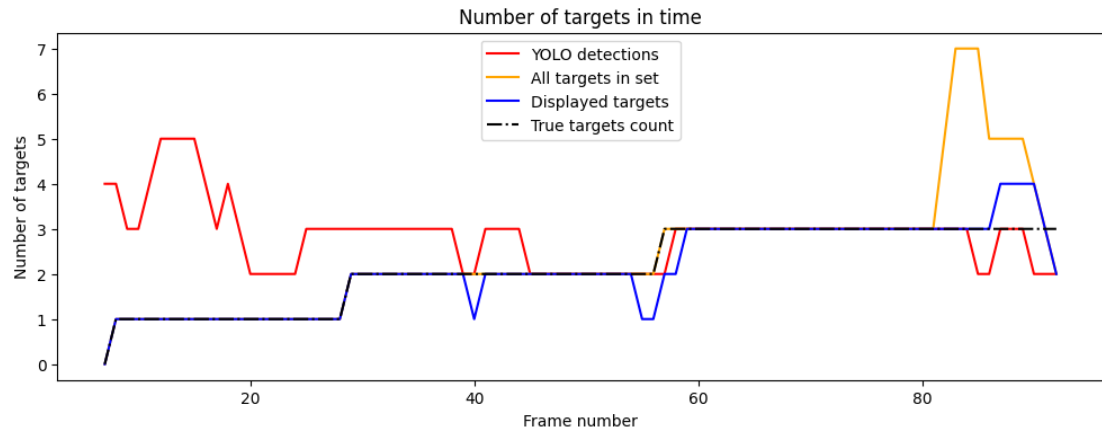
$P_{D,k}(x)$	$P$	$\sigma_v$	$\sigma_\epsilon$	$T_H$	$T_d$	$T_p$	$T_l$	$T_{YOLO}$
0.3	diag(500, 500, 500, 500)	0.1	100	2	3	0.1	0.0001	0.3

■ **Table 6.11** The parameter settings for Experiment E2-V3-S2 with the dynamic detection probability.

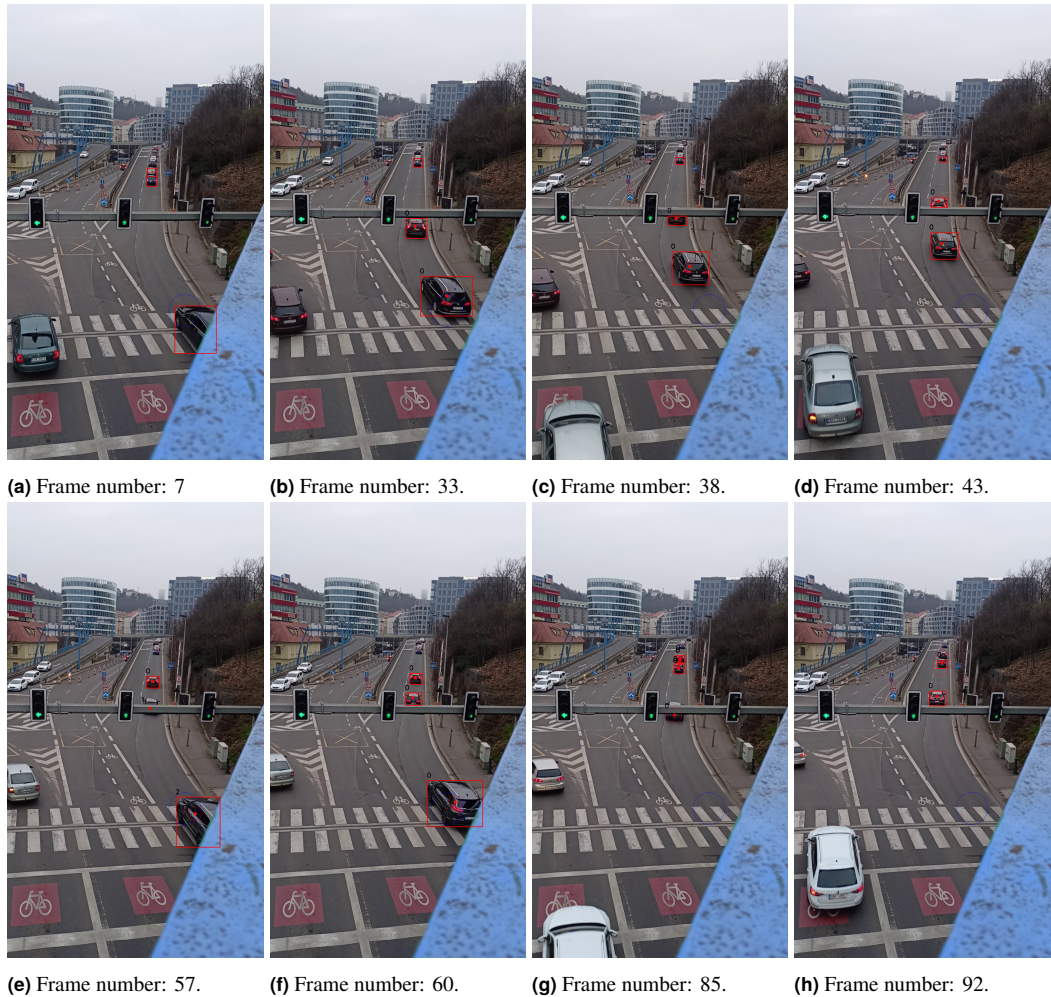
The scenario in Figure 6.22 is nearly identical as in the experiment with settings *S1*. All targets are tracked properly and none of them is lost.

Figure 6.21 shows the true difference between settings *S1* and *S2*. The blue line deflects less from the true count. In situation where the targets are hidden, the number of the targets in the filters' queue (orange line) copies the true count line. Only from the frame no. 80, the orange line shows some errors, due to the targets' appearance in the same neighborhood.

The settings *S2* again shows a slightly improved performance over settings *S1*. The overall performance can be seen in Figure 6.21.



■ **Figure 6.21** Development chart of the number of detected targets, targets in the filter's queue, displayed targets and true targets' count.



■ **Figure 6.22** Image sequence of tracked objects using the GM-PHD filter with the dynamic detection probability, the YOLO object detector and the SAM image segmentation model.

### 6.2.3.3 S3 – Grounded SAM

The combination of Grounding DINO and SAM is also evaluated on the video V3. The utilized parameters are outlined in Table 6.12.

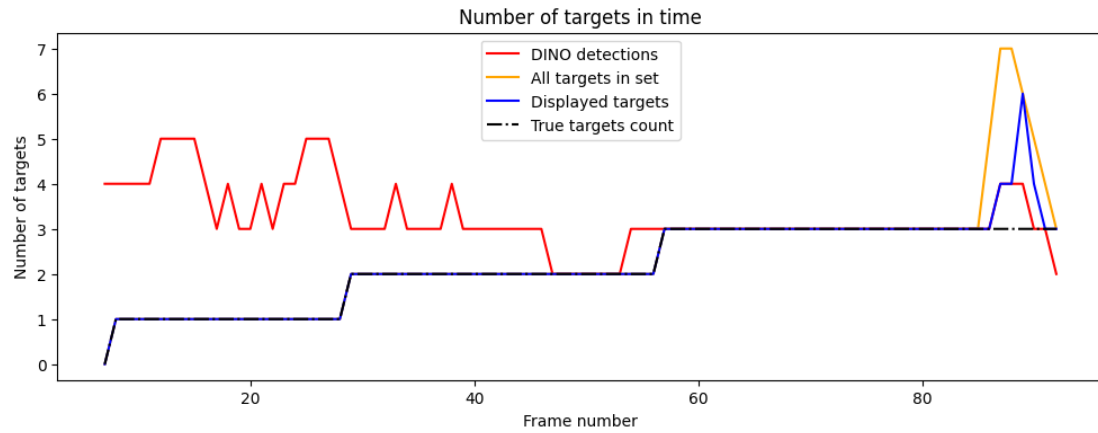
$P_{D,k}(x)$	$P$	$\sigma_v$	$\sigma_\epsilon$	$T_H$	$T_d$	$T_p$	$T_l$	$T_{text}$	$T_{bbox}$
0.3	$diag(500, 500, 500, 500)$	0.1	80	2	3	0.1	0.01	0.3	0.3

■ **Table 6.12** The parameter settings for Experiment E2-V3-S3 with the dynamic detection probability.

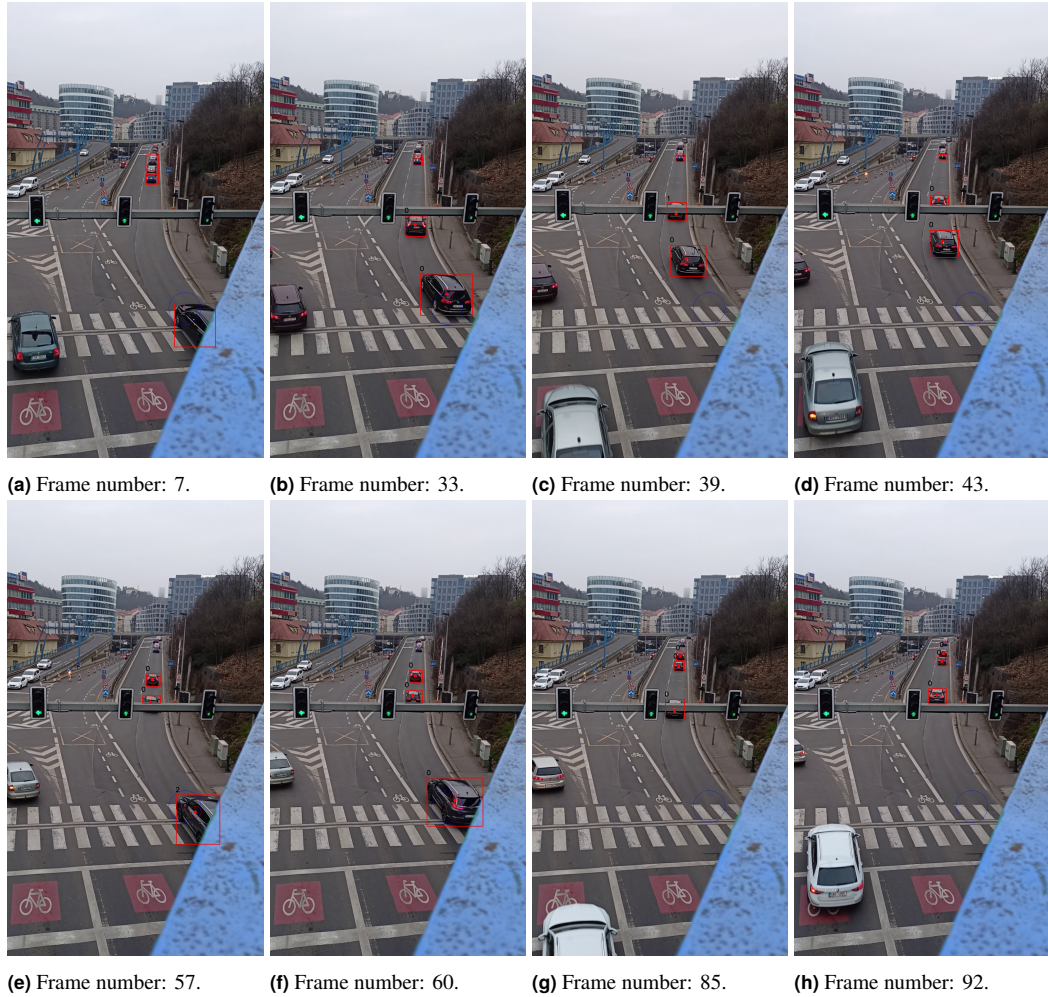
As seen in Figures 6.24c, 6.24e and 6.24g, Grounding DINO is able to detect the hidden objects behind the light pole, thus the advantage of the dynamic detection probability is not apparent. All targets are tracked precisely and no misdetection is present.

Till the frame no. 85, the number of displayed targets (blue line) and the number of targets in filter's queue (orange line) exactly copies the true number of target's line in Figure 6.23. It is, of course, influenced by the employment of the enhanced object

detector, which has managed to detect semi-hidden targets. The increasing and decreasing number of targets after the frame 85 is due to the targets being close to each other.



■ **Figure 6.23** Development chart of the number of detected targets, targets in the filter's queue, displayed targets and true targets' count.



■ **Figure 6.24** Image sequence of tracked objects using the GM-PHD filter with the dynamic detection probability, the DINO object detector and the SAM image segmentation model.

#### 6.2.4 V2a

In this experiment, we have a camera recording of traffic, but the view is obstructed by a significant obstacle, disposing any object detection system of the capability to capture targets. To simulate this situation, we artificially add a road crossing the main highway line in the video V2. Although it is evident that the added road does not belong to the scene, its color characteristics closely resemble those of the natural highway line. Furthermore, the video playback frame rate is decreased to 10 fps.

#### 6.2.5 V2a – GM-PHD with the dynamic detection probability

Based on the prior experiments, it is deemed unproductive to assess the GM-PHD filter under the constant detection probability. If the adapted GM-PHD filter demonstrates the capability to track objects even in areas lacking measurements, the forthcoming experiment, designated as setting *S1*, is suggested.

### 6.2.5.1 S1 – YOLO + YOLO

This experiment employs settings *S1* on the video *V2*, which includes an additional obstacle. The parameter settings are shown in Table 6.13.

$P_{D,k}(x)$	$P$	$\sigma_v$	$\sigma_\epsilon$	$T_H$	$T_d$	$T_p$	$T_l$	$T_{YOLO}$
0.3	diag(40, 40, 40, 40)	0.04	120	0.5	3	0.1	0.001	0.3

■ **Table 6.13** The parameter settings for Experiment E2-V2a-S1 with the dynamic detection probability.

In Figure 6.25 we can see the tracking performance of the GM-PHD filter with settings *S1* on the traffic situation with an added obstacle. For this experiment, two additional bounding boxes are displayed. The blue bbox represents the place, the target has been lastly detected in. The black bbox is the moving bbox from Equation (5.29). The color characteristics of the scene given by these two bounding boxes are compared to calculate  $p_{H,k}$  in (5.31).

- **6.25a:** The tracking starts with frame no. 47. There are two cars next to each other. At this moment, the cars are coming close to the obstacle.
- **6.25b:** The targets are obscured and remain undetected, with their state labeled as *hidden*.
- **6.25c:** Given the characteristics of the scene, the targets' positions lag slightly behind their true positions.
- **6.25d:** The cars are detected again and, due to the large covariance, the targets get their measurements.
- **6.25e:** Nevertheless, one false target still falls behind the true targets.
- **6.25f:** Even though the true targets continue in their path with correct measurements, the false target persists.
- **6.25g:** Due to the similar characteristics of the added road with the actual highway road, the false target is considered as hidden.
- **6.25h:** Finally the false target is removed, not due to exceeding the lowered threshold  $T_l$ , but due to the change of its state to *dead*.

In this experiment, we demonstrated that with the GM-PHD filter with the dynamic detection probability it is possible to overcome an obstacle blocking the view of the camera. However, another problem arises. If the obstacle has similar color characteristics as the background around the target, the predicted false target survives for too long.

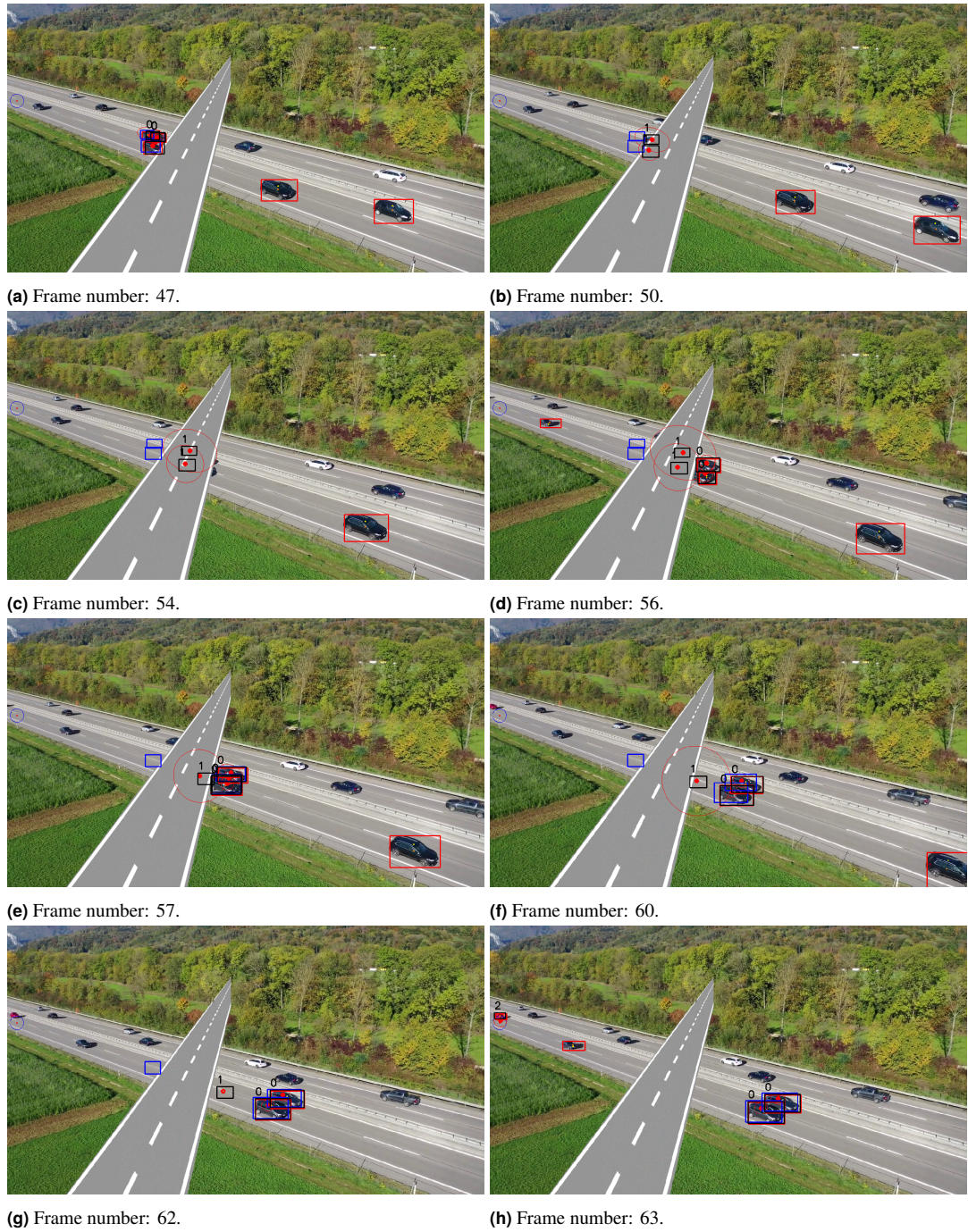


**Figure 6.25** Image sequence of the tracked objects using the GM-PHD filter with the dynamic detection probability and YOLO only.

### 6.2.6 V2b

The preceding experiment evaluates the performance of the GM-PHD filter with the dynamic detection probability under settings *S1* on a video featuring an added obstacle with color characteristics similar to the surrounding scene. In this experiment, the

obstacle possesses slightly different color characteristics. The primary objective of this experiment is to assess the efficacy of the modified pruning step influenced by the Markov process.

### 6.2.7 V2b – GM-PHD with the dynamic detection probability

The conditions of this experiment remain the same as in Experiment 6.2.4, i.e., the YOLO object detector and segmentation model is used.

#### 6.2.7.1 S1 – YOLO + YOLO

For fair comparison, the parameter settings included in Table 6.14 are left the same.

$P_{D,k}(x)$	$P$	$\sigma_v$	$\sigma_\epsilon$	$T_H$	$T_d$	$T_p$	$T_l$	$T_{YOLO}$
0.3	diag(40, 40, 40, 40)	0.04	120	0.5	3	0.1	0.001	0.3

■ **Table 6.14** The parameter settings for Experiment E2-V2b-S1 with the dynamic detection probability.

In Figure 6.26 we can see the tracking performance of the GM-PHD filter with settings *S1* on traffic situation with an added obstacle.

- **6.26a:** This sequence starts with frame no. 44. Due to the targets' close positions, more than 2 targets appear in the place where only two true targets are present.
- **6.26b:** The targets move underneath the obstacle.
- **6.26c:** This is the first frame with misdected objects. The targets are in the *hidden* state.
- **6.26d:** The targets' predicted positions are already behind the true targets' positions.
- **6.26e:** As the predicted covariance grows, the targets merge into a single one. The cars are clearly seen, but the YOLO model does not detect them.
- **6.26f:** The cars are detected and initialized as targets. The predicted black bounding box of false target still interferes with the added obstacle, thus the target is considered as hidden.
- **6.26g:** In this frame, the predicted black bounding box of false target moves to the area with natural traffic line. The false target is in *dead* state and is removed immediately.
- **6.26h:** The targets continue in their paths with correct positions.

In this experiment, we have demonstrated, that if an obstacle differs from the targets' background scene, the pruning given by the Markov process works exceptionally well. The downside of this approach lies in the additional settings of further parameters.

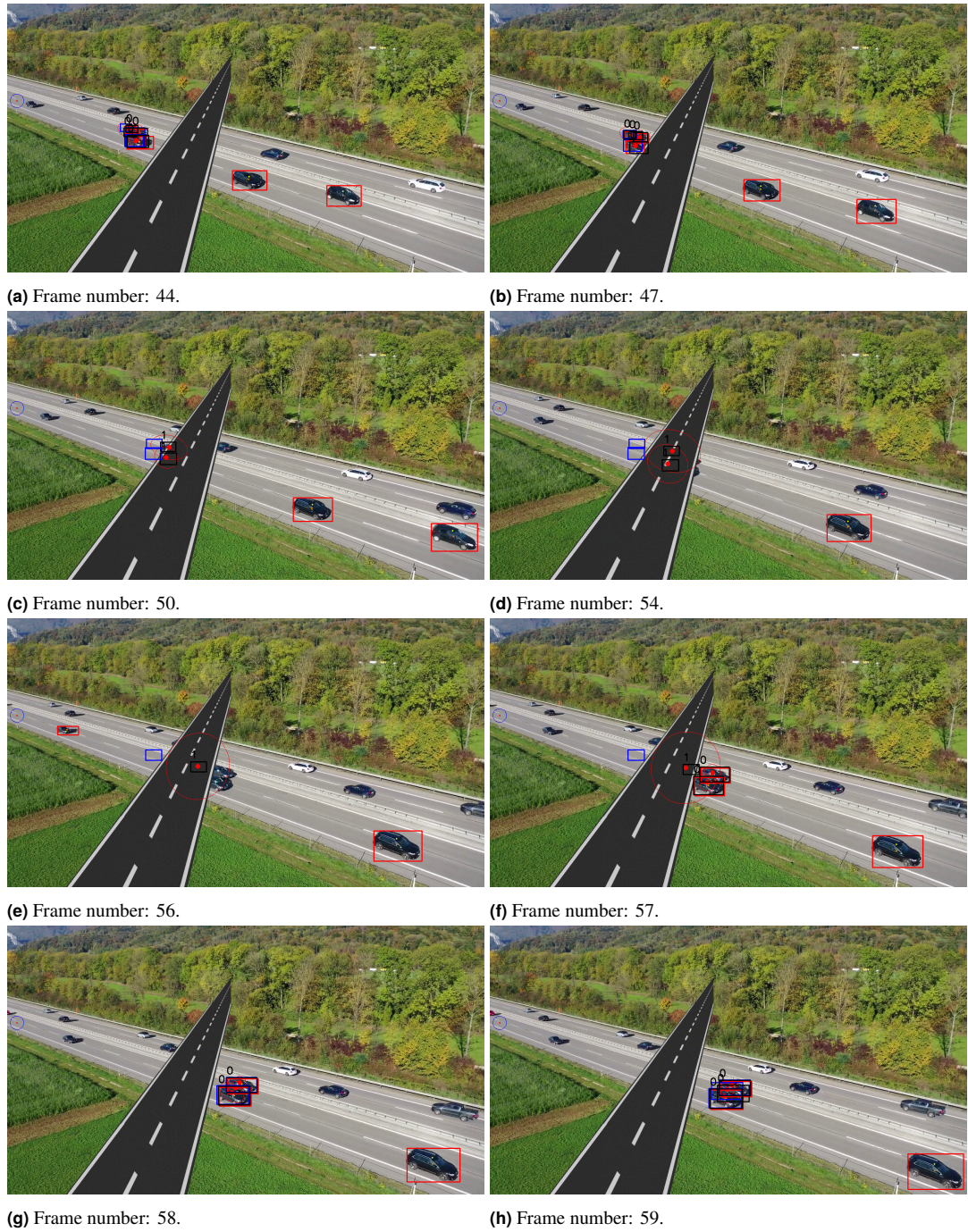


**Figure 6.26** Image sequence of tracked objects using the GM-PHD filter with the dynamic detection probability and YOLO only.

### 6.3 E3: Changing the model

Up to this point, all experiments have employed the observation and state-space models outlined in the introduction of the Experiments section (see Section 6). However,

using these models in scenarios presented by videos  $V1$ ,  $V2$ ,  $V3$  comes with several disadvantages. The state-space model assumes an uniform position uncertainty in all directions for targets. Additionally, the videos are not captured from a bird's-eye point of view, but from an angled perspective. This camera angle causes the detected targets to appear smaller when they are further away, and larger when they are closer to the camera. Consequently, this effect alters the actual movement model of the targets, which our current model does not account for.

Considering the videos utilized in this study, we can leverage prior knowledge regarding the movement patterns of the potential targets. It is established that cars are inclined to move in the direction of the road rather than backwards or sideways.

### 6.3.1 V2

For this experiment, the video  $V2$  with the added crossing road as an obstacle is used. The video is observed at the rate 14 fps.

The state space CVM model is employed with the transition matrix

$$F_k = \begin{bmatrix} 1 & 0 & 2\Delta & 0 \\ 0 & 1 & 0 & \Delta \\ 0 & 0 & 1.1 & 0 \\ 0 & 0 & 0 & 1.1 \end{bmatrix}, \quad (6.2)$$

where  $\Delta = 1$ , and process covariance matrix

$$Q_k = \begin{bmatrix} 2 & 0.5 & 0 & 0 \\ 0.5 & 1 & 0 & 0 \\ 0 & 0 & 1 & 0 \\ 0 & 0 & 0 & 1 \end{bmatrix} \cdot 0.003. \quad (6.3)$$

The observation covariance matrix is reformulated as

$$R_k = \begin{bmatrix} 2 & 0.5 \\ 0.5 & 1 \end{bmatrix} \cdot 20. \quad (6.4)$$

The spawning point providing nearby targets with initial covariance matrix  $P$  is established as

$$P_k = \begin{bmatrix} 80 & 20 & 0 & 0 \\ 20 & 40 & 0 & 0 \\ 0 & 0 & 40 & 0 \\ 0 & 0 & 0 & 40 \end{bmatrix}. \quad (6.5)$$

These model formulations ensure that the target's covariance takes an ellipsoidal shape rather than a circular one. These ellipses are oriented in the direction of the road, indicating that uncertainty increases more in alignment with the road's direction. This implies a lower probability of a car being positioned next to the road in the subsequent time step.

### 6.3.2 V2b – GM-PHD with the dynamic detection probability

The GM-PHD filter with the dynamic detection probability is analysed only in this experiment. The best performing settings are used - *S3*, i.e., grounded SAM.

#### 6.3.2.1 S3 – Grounded SAM

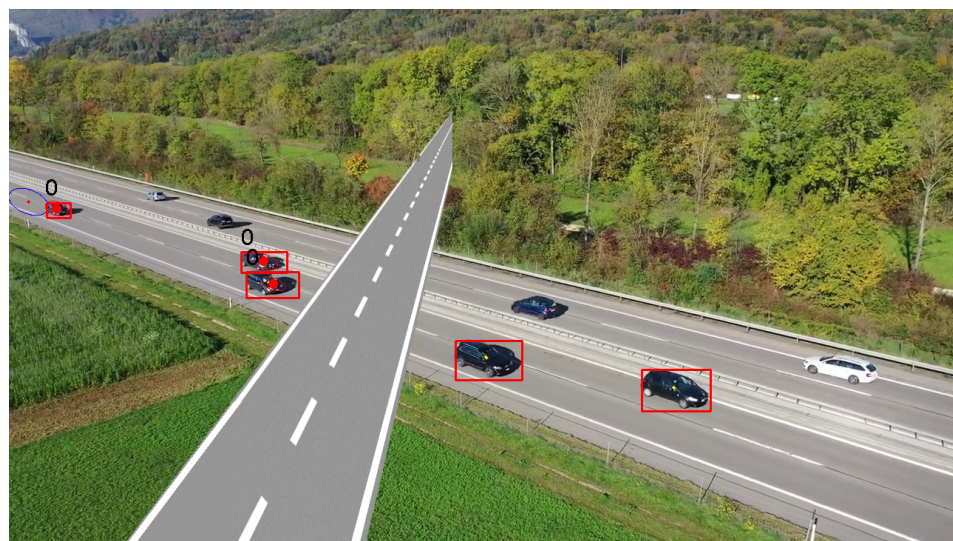
In Table 6.15, note that the standard pruning threshold  $T_p$  is the same as the lowered pruning threshold  $T_l$ . Due to the better model settings and the dynamic detection probability, it is not necessary to lower the pruning threshold for targets in *detected* and *hidden* state.

$P_{D,k}(x)$	$P$	$\sigma_v$	$\sigma_\epsilon$	$T_H$	$T_d$	$T_p$	$T_l$	$T_{text}$	$T_{bbox}$
0.3	see Eq. 6.5	see Eq. 6.3	see Eq. 6.4	0.6	3	0.1	0.1	0.3	0.3

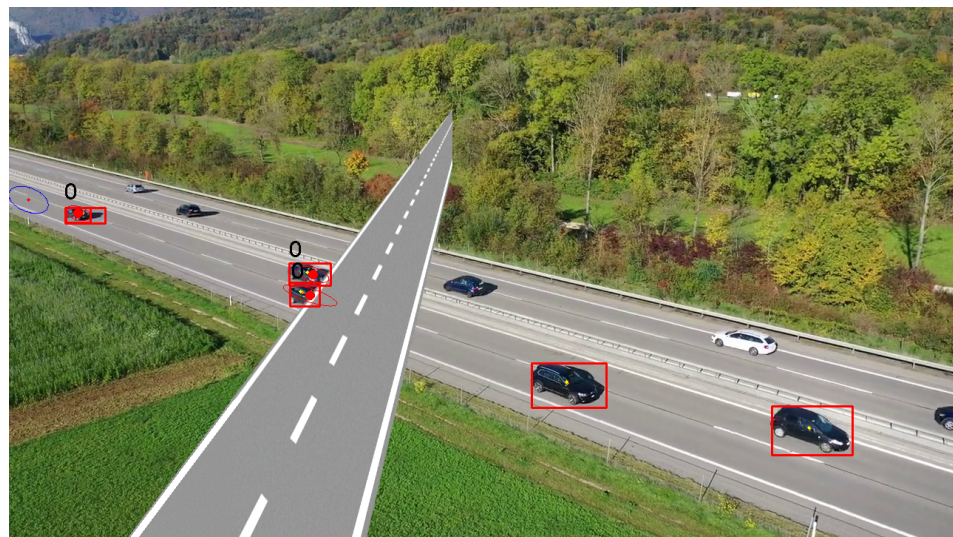
■ **Table 6.15** The parameter settings for Experiment E3-V2-S3 with the dynamic detection probability.

The adjusted models project in Figures 6.27 and 6.28. The spawning point, as well as the covariances given by the covariance matrix  $P$ , has an ellipsoidal shape showing the uncertainty. Two cars are observed in the sequence. Let us call the car driving in the right highway line in the direction of travel  $C_R$  and the left car as  $C_L$ .

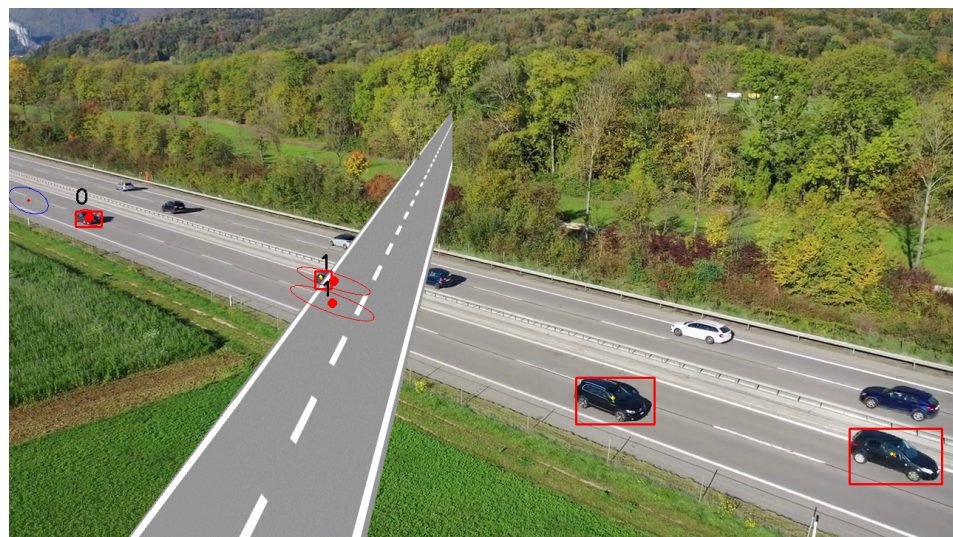
- **6.27a:** Two targets approach the obstacle. Both cars are successfully detected and initialized.
- **6.27b:** Target  $C_R$  is detected for the final time before reaching the obstacle.
- **6.27c:** The object detector still manages to detect  $C_L$ , but its position is now beneath the obstacle, resulting in both targets being classified as *hidden*.
- **6.28a:** Both targets remain hidden, showcasing the effect of the altered models. Notably, the covariances are elongated in the direction of travel and do not extend beyond the traffic line.
- **6.28b:** Despite minimal fine-tuning of the model parameters for this experiment, the predicted mean positions are nearly accurate. Both cars are detected once more, allowing the filter to obtain measurements.
- **6.28c:** The additional false target is removed and both targets are tracked with small ellipsoidal covariances.



(a) Frame number: 44.

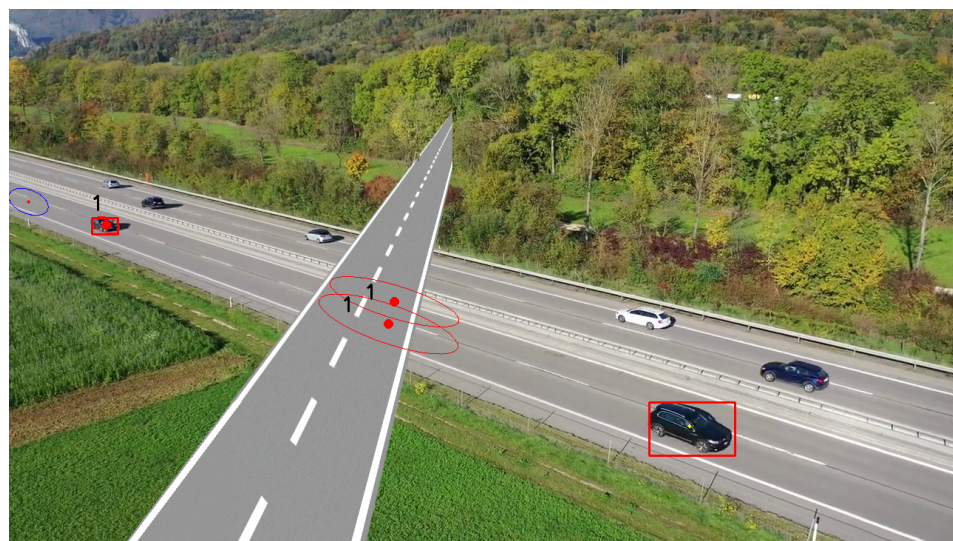


(b) Frame number: 48.

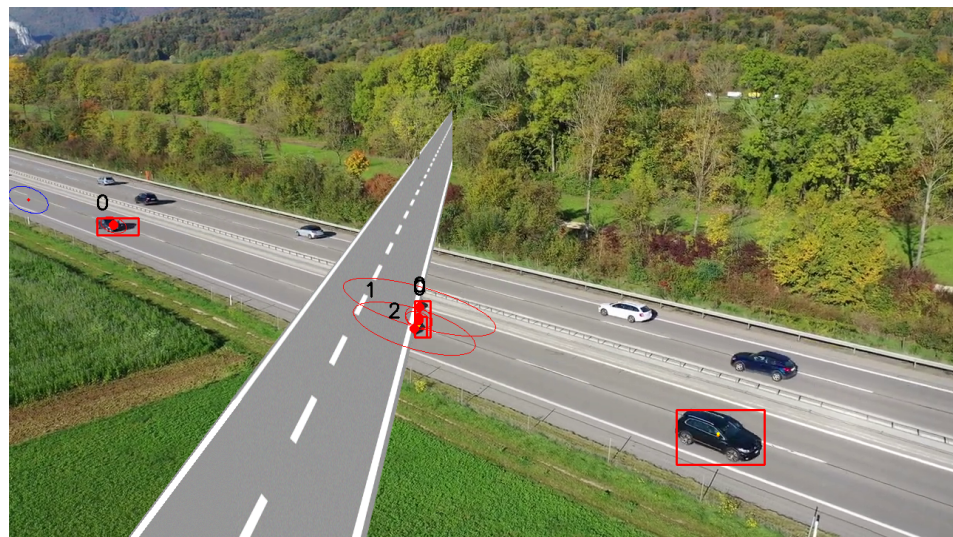


(c) Frame number: 50.

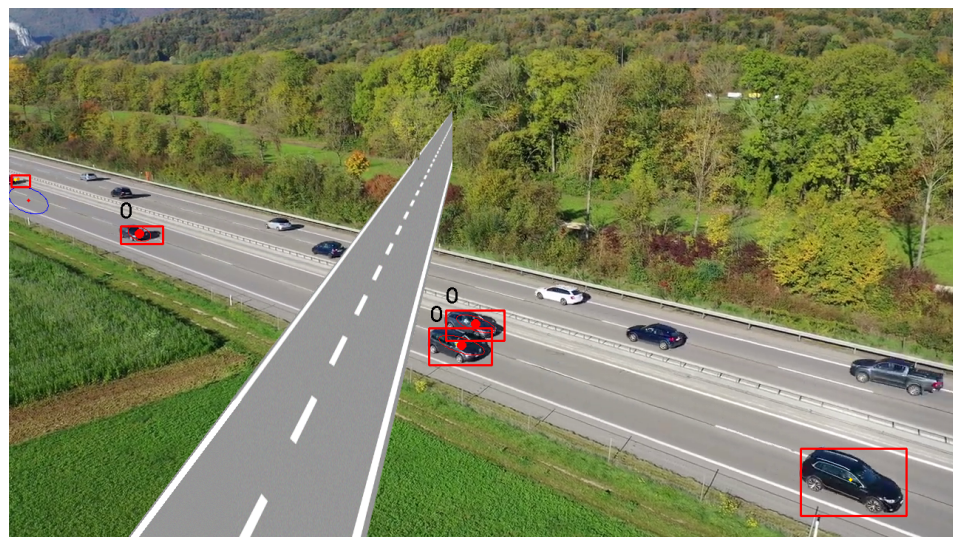
■ **Figure 6.27** Image sequence of tracked objects using the GM-PHD filter with the dynamic detection probability, Grounded SAM and adjusted models – part 1.



(a) Frame number: 53.



(b) Frame number: 54.



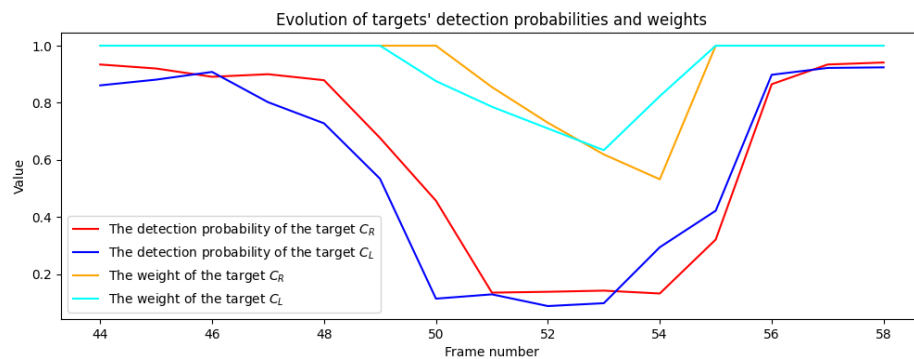
(c) Frame number: 58.

■ **Figure 6.28** Image sequence of tracked objects using the GM-PHD filter with the dynamic detection probability, Grounded SAM and adjusted models – part 2.

Table 6.16 and Figure 6.29 display the values of the detection probabilities of targets  $C_L$  and  $C_R$  in corresponding frames. If the targets are visible in the scene, the detection probability is large. Once the targets are hidden behind the obstacle, the detection probability rapidly drops. The value of the probability is about 0.1 from frame 50 to 54. The effect of this low detection probability is projected in Table 6.16 and Figure 6.29 as well. The targets' weights are slowly decreasing, sustaining the targets' existence in period without any measurement.

Frame number	Detection probabilities		Targets' weights	
	$p_{D,k}(C_L)$	$p_{D,k}(C_R)$	$w_k(C_L)$	$w_k(C_R)$
44	0.934	0.861	1	1
45	0.920	0.881	1	1
46	0.891	0.908	1	1
47	0.900	0.802	1	1
48	0.879	0.728	1	1
49	0.677	0.534	1	1
50	0.457	0.114	1	0.876
51	0.135	0.129	0.855	0.786
52	0.138	0.088	0.730	0.710
53	0.142	0.098	0.619	0.634
54	0.132	0.294	0.532	0.823
55	0.321	0.422	1	1
56	0.865	0.898	1	1
57	0.934	0.922	1	1
58	0.941	0.924	1	1

■ **Table 6.16** The evolution of detection probabilities and weights of targets  $C_L$  and  $C_R$ .



■ **Figure 6.29** The evolution of targets' detection probabilities and weights.

This experiment illustrates that even in scenarios with challenging conditions, such as angled recordings, it is possible to configure the model using prior scene knowledge in a manner that enables the filter to effectively handle obstacles obstructing the camera view. Moreover, these model settings are capable of addressing the necessity for dynamically setting the noise covariances. Table 6.16 and Figure 6.29 demonstrate the effect of the dynamic detection probability on targets' weights. Note that targets in Figures

6.27 and 6.28 are correctly in *hidden* state. Thus, if the obstacle would be larger, due to possibility of changing the pruning threshold for targets in *detected* and *hidden* state, the targets might survive even longer. This additional threshold possibility does not allow the creation of other false targets that would appear if the standard pruning threshold was lowered.

## Chapter 7

# Conclusion

In this thesis, we have delved into the realm of Bayesian filtering and its profound impact on multi-target tracking systems. Real-world scenarios pose significant challenges, as tracking systems must grapple with non-linear and non-Gaussian models, as well as contend with noisy measurements and cluttered environments. Negotiating such complexities necessitates fine-tuning of additional parameters within tracking systems tailored to the specific environmental conditions. In order to eventually simulate target movement patterns and treat the problems that stem from sensor measurement uncertainties more accurately, researchers continually explore innovative methodologies to ascertain or estimate these parameters.

This work introduces an innovative approach aimed at estimating one of the key parameters crucial to tracking systems – the detection probability. This probability is profoundly influential in the survivability of tracked objects, making its accurate estimation paramount. Leveraging advanced deep-learning image processing techniques, we propose a method to estimate the detection probability for each target at every time step within video footage. Furthermore, we address the possibility of the target misdetection, a common occurrence when obstacles obstruct the camera's view. To endorse the resilience of targets during extended periods without detection, we refine the pruning method of the GM-PHD filter.

The experiments demonstrate the effectiveness of the proposed method, particularly in scenarios where tracked objects are undetectable. However, they also reveal certain weaknesses that warrant further investigation in future research endeavors.

# Bibliography

- [1] Y. Bar-Shalom and X. Li, *Multitarget-Multisensor Tracking: Principles and Techniques*. Yaakov Bar-Shalom, 1995, ISBN: 9780964831209.
- [2] R. E. Kalman, “A New Approach to Linear Filtering and Prediction Problems,” *Journal of Basic Engineering*, 82, pp. 35–45, 1960.
- [3] M. Arulampalam, S. Maskell, N. Gordon, and T. Clapp, “A tutorial on particle filters for online nonlinear/non-Gaussian Bayesian tracking,” *IEEE Transactions on Signal Processing*, 50, no. 2, pp. 174–188, 2002. doi: [10.1109/78.978374](https://doi.org/10.1109/78.978374).
- [4] E. Brekke, *Fundamentals of Sensor Fusion*. Norwegian University of Science and Technology, 2020.
- [5] R. Mahler, “Multitarget Bayes filtering via first-order multitarget moments,” *IEEE Transactions on Aerospace and Electronic Systems*, 39, no. 4, pp. 1152–1178, 2003. doi: [10.1109/TAES.2003.1261119](https://doi.org/10.1109/TAES.2003.1261119).
- [6] A. Jazwinski, *Stochastic Processes and Filtering Theory*, Dover Books on Electrical Engineering Series. Dover Publications, 2007, ISBN: 9780486462745.
- [7] S. Julier and J. Uhlmann, “Unscented filtering and nonlinear estimation,” *Proceedings of the IEEE*, 92, no. 3, pp. 401–422, 2004. doi: [10.1109/JPROC.2003.823141](https://doi.org/10.1109/JPROC.2003.823141).
- [8] D. Reid, “An algorithm for tracking multiple targets,” *IEEE Transactions on Automatic Control*, 24, no. 6, pp. 843–854, Dec. 1979.
- [9] B.-N. Vo and W.-K. Ma, “The Gaussian mixture probability hypothesis density filter,” *IEEE Transactions on Signal Processing*, 54, no. 11, pp. 4091–4104, 2006. doi: [10.1109/TSP.2006.881190](https://doi.org/10.1109/TSP.2006.881190).
- [10] R. P. S. Mahler, B.-T. Vo, and B.-N. Vo, “CPHD filtering with unknown clutter rate and detection profile,” *IEEE Transactions on Signal Processing*, 59, no. 8, pp. 3497–3513, 2011. doi: [10.1109/TSP.2011.2128316](https://doi.org/10.1109/TSP.2011.2128316).
- [11] Á. F. García-Fernández, J. L. Williams, K. Granström, and L. Svensson, “Poisson multi-Bernoulli mixture filter: Direct derivation and implementation,” *IEEE Transactions on Aerospace and Electronic Systems*, 54, no. 4, pp. 1883–1901, 2018. doi: [10.1109/TAES.2018.2805153](https://doi.org/10.1109/TAES.2018.2805153).
- [12] A. Milan, L. Leal-Taixé, I. Reid, S. Roth, and K. Schindler, “Mot16: A benchmark for multi-object tracking,” *arXiv preprint arXiv:1603.00831*, 2016.
- [13] S. Yan, Y. Fu, W. Zhang, W. Yang, R. Yu, and F. Zhang, “Multi-target instance segmentation and tracking using YOLOV8 and BoT-SORT for video SAR,” in *2023 5th International Conference on Electronic Engineering and Informatics (EEI)*, 2023, pp. 506–510. doi: [10.1109/EEI59236.2023.10212903](https://doi.org/10.1109/EEI59236.2023.10212903).

- [14] G. Hendeby and R. Karlsson, "Gaussian mixture PHD filtering with variable probability of detection," in *17th International Conference on Information Fusion (FUSION)*, 2014, pp. 1–7.
- [15] B.-T. Vo, B.-N. Vo, R. Hoseinnezhad, and R. P. S. Mahler, "Robust multi-Bernoulli filtering," *IEEE Journal of Selected Topics in Signal Processing*, 7, no. 3, pp. 399–409, 2013. doi: [10.1109/JSTSP.2013.2252325](https://doi.org/10.1109/JSTSP.2013.2252325).
- [16] G. Li, L. Kong, W. Yi, and X. Li, "Robust Poisson multi-Bernoulli mixture filter with unknown detection probability," *IEEE Transactions on Vehicular Technology*, 70, no. 1, pp. 886–899, 2021. doi: [10.1109/TVT.2020.3047107](https://doi.org/10.1109/TVT.2020.3047107).
- [17] C. Li, W. Wang, T. Kirubarajan, J. Sun, and P. Lei, "PHD and CPHD filtering with unknown detection probability," *IEEE Transactions on Signal Processing*, 66, no. 14, pp. 3784–3798, 2018. doi: [10.1109/TSP.2018.2835398](https://doi.org/10.1109/TSP.2018.2835398).
- [18] J. Wei, F. Luo, J. Qi, and L. Ruan, "A modified BGM-PHD filter with unknown detection probability," in *2023 6th International Conference on Information Communication and Signal Processing (ICICSP)*, 2023, pp. 492–496. doi: [10.1109/ICICSP59554.2023.10390615](https://doi.org/10.1109/ICICSP59554.2023.10390615).
- [19] E. Hanusa and D. W. Krout, "Track state augmentation for estimation of probability of detection in multistatic sonar data," in *2013 Asilomar Conference on Signals, Systems and Computers*, 2013, pp. 1733–1737. doi: [10.1109/ACSSC.2013.6810598](https://doi.org/10.1109/ACSSC.2013.6810598).
- [20] S. Horn, "Near real time estimation of surveillance gaps," in *Proceedings of the 16th International Conference on Information Fusion*, 2013, pp. 1871–1877.
- [21] S. Wei, B. Zhang, and W. Yi, "Trajectory PHD and CPHD filters with unknown detection profile," *IEEE Transactions on Vehicular Technology*, 71, no. 8, pp. 8042–8058, 2022. doi: [10.1109/TVT.2022.3174055](https://doi.org/10.1109/TVT.2022.3174055).
- [22] Y. Bulut, D. Vines-Cavanaugh, and D. Bernal, "Process and measurement noise estimation for Kalman filtering," *Conference Proceedings of the Society for Experimental Mechanics Series*, 3, May 2011. doi: [10.1007/978-1-4419-9834-7\\_36](https://doi.org/10.1007/978-1-4419-9834-7_36).
- [23] U. Hadar and H. messer, "High-order hidden markov models - estimation and implementation," in *2009 IEEE/SP 15th Workshop on Statistical Signal Processing*, 2009, pp. 249–252. doi: [10.1109/SSP.2009.5278591](https://doi.org/10.1109/SSP.2009.5278591).
- [24] K. Dedecius and P. M. Djurić, "Sequential estimation and diffusion of information over networks: A Bayesian approach with exponential family of distributions," *IEEE Transactions on Signal Processing*, 65, no. 7, pp. 1795–1809, 2017. doi: [10.1109/TSP.2016.2641380](https://doi.org/10.1109/TSP.2016.2641380).
- [25] Y. Bar-Shalom, F. Daum, and J. Huang, "The probabilistic data association filter," *IEEE Control Systems Magazine*, 29, no. 6, pp. 82–100, 2009.
- [26] Z. Khan, T. Balch, and F. Dellaert, "MCMC-based particle filtering for tracking a variable number of interacting targets," *IEEE Transactions on Pattern Analysis and Machine Intelligence*, 27, no. 11, pp. 1805–1819, 2005. doi: [10.1109/TPAMI.2005.223](https://doi.org/10.1109/TPAMI.2005.223).
- [27] F. Gustafsson, F. Gunnarsson, N. Bergman, U. Forssell, J. Jansson, R. Karlsson, and P.-J. Nordlund, "Particle filters for positioning, navigation, and tracking," *IEEE Transactions on Signal Processing*, 50, no. 2, pp. 425–437, 2002. doi: [10.1109/78.978396](https://doi.org/10.1109/78.978396).
- [28] A. Doucet, N. Gordon, and V. Krishnamurthy, "Particle filters for state estimation of jump Markov linear systems," *IEEE Transactions on Signal Processing*, 49, no. 3, pp. 613–624, 2001. doi: [10.1109/78.905890](https://doi.org/10.1109/78.905890).
- [29] I. Goodman, R. Mahler, and H. Nguyen, *Mathematics of Data Fusion*, Theory and Decision Library B. Springer Netherlands, 1997, ISBN: 9780792346746.
- [30] B.-N. Vo, S. Singh, and A. Doucet, "Random finite sets and sequential Monte Carlo methods in multi-target tracking," in *2003 Proceedings of the International Conference on Radar (IEEE Cat. No.03EX695)*, 2003, pp. 486–491. doi: [10.1109/RADAR.2003.1278790](https://doi.org/10.1109/RADAR.2003.1278790).

- [31] D. Daley and D. Vere-Jones, *An introduction to the theory of point processes*. Springer, Nov. 2003.
- [32] Y. Bar-Shalom and T. Fortmann, *Tracking and Data Association*, Mathematics in science and engineering. Academic Press, 1988, ISBN: 9780120797608.
- [33] N. Dalal and B. Triggs, “Histograms of oriented gradients for human detection,” in *2005 IEEE Computer Society Conference on Computer Vision and Pattern Recognition (CVPR'05)*, vol. 1, 2005, 886–893 vol. 1. doi: [10.1109/CVPR.2005.177](https://doi.org/10.1109/CVPR.2005.177).
- [34] Y. Li, X. Xu, N. Mu, and L. Chen, “Eye-gaze tracking system by haar cascade classifier,” in *2016 IEEE 11th Conference on Industrial Electronics and Applications (ICIEA)*, 2016, pp. 564–567. doi: [10.1109/ICIEA.2016.7603648](https://doi.org/10.1109/ICIEA.2016.7603648).
- [35] J. Redmon, S. Divvala, R. Girshick, and A. Farhadi, “You only look once: Unified, real-time object detection,” in *2016 IEEE Conference on Computer Vision and Pattern Recognition (CVPR)*, 2016, pp. 779–788. doi: [10.1109/CVPR.2016.91](https://doi.org/10.1109/CVPR.2016.91).
- [36] P. Jiang, D. Ergu, F. Liu, Y. Cai, and B. Ma, “A review of YOLO algorithm developments,” *Procedia Computer Science*, 199, pp. 1066–1073, 2022, The 8th International Conference on Information Technology and Quantitative Management (ITQM 2020 2021): Developing Global Digital Economy after COVID-19, ISSN: 1877-0509. doi: <https://doi.org/10.1016/j.procs.2022.01.135>.
- [37] K. He, G. Gkioxari, P. Dollár, and R. Girshick, “Mask R-CNN,” in *2017 IEEE International Conference on Computer Vision (ICCV)*, 2017, pp. 2980–2988. doi: [10.1109/ICCV.2017.322](https://doi.org/10.1109/ICCV.2017.322).
- [38] *What is image segmentation?* [Online]. Available: <https://www.ibm.com/topics/image-segmentation> (visited on 05/04/2024).
- [39] Y. Guo and B. Yang, “A survey of semantic segmentation methods in traffic scenarios,” in *2022 International Conference on Machine Learning, Cloud Computing and Intelligent Mining (MLC-CIM)*, 2022, pp. 452–457. doi: [10.1109/MLCCIM55934.2022.00083](https://doi.org/10.1109/MLCCIM55934.2022.00083).
- [40] R. Mohan and A. Valada, “Efficientps: Efficient panoptic segmentation,” *International Journal of Computer Vision (IJCV)*, 2021.
- [41] R. Girshick, J. Donahue, T. Darrell, and J. Malik, “Rich feature hierarchies for accurate object detection and semantic segmentation,” in *2014 IEEE Conference on Computer Vision and Pattern Recognition*, 2014, pp. 580–587. doi: [10.1109/CVPR.2014.81](https://doi.org/10.1109/CVPR.2014.81).
- [42] T.-Y. Lin, P. Dollár, R. Girshick, K. He, B. Hariharan, and S. Belongie, “Feature pyramid networks for object detection,” in *2017 IEEE Conference on Computer Vision and Pattern Recognition (CVPR)*, 2017, pp. 936–944. doi: [10.1109/CVPR.2017.106](https://doi.org/10.1109/CVPR.2017.106).
- [43] J. Zhang, D. Sun, Z. Luo, A. Yao, L. Zhou, T. Shen, Y. Chen, L. Quan, and H. Liao, “Learning two-view correspondences and geometry using order-aware network,” *International Conference on Computer Vision (ICCV)*, 2019.
- [44] A. Kirillov, R. Girshick, K. He, and P. Dollár, *Panoptic feature pyramid networks*, 2019. arXiv: [1901.02446](https://arxiv.org/abs/1901.02446) [cs.CV].
- [45] Y. Xiong, R. Liao, H. Zhao, R. Hu, M. Bai, E. Yumer, and R. Urtasun, *Upsnet: A unified panoptic segmentation network*, 2019. arXiv: [1901.03784](https://arxiv.org/abs/1901.03784) [cs.CV].
- [46] Y. Yang, H. Li, X. Li, Q. Zhao, J. Wu, and Z. Lin, *Sognet: Scene overlap graph network for panoptic segmentation*, 2019. arXiv: [1911.07527](https://arxiv.org/abs/1911.07527) [cs.CV].
- [47] Y. Wu, G. Zhang, Y. Gao, X. Deng, K. Gong, X. Liang, and L. Lin, *Bidirectional graph reasoning network for panoptic segmentation*, 2020. arXiv: [2004.06272](https://arxiv.org/abs/2004.06272) [cs.CV].
- [48] H. Sun, C. Li, B. Liu, H. Zheng, D. D. Feng, and S. Wang, *Aunet: Attention-guided dense-upsampling networks for breast mass segmentation in whole mammograms*, 2019. arXiv: [1810.10151](https://arxiv.org/abs/1810.10151) [cs.CV].

- [49] N. Otsu, “A threshold selection method from gray-level histograms,” *IEEE Transactions on Systems, Man, and Cybernetics*, 9, no. 1, pp. 62–66, 1979. doi: [10.1109/TSMC.1979.4310076](https://doi.org/10.1109/TSMC.1979.4310076).
- [50] J. Canny, “A computational approach to edge detection,” *IEEE Transactions on Pattern Analysis and Machine Intelligence*, PAMI-8, no. 6, pp. 679–698, 1986. doi: [10.1109/TPAMI.1986.4767851](https://doi.org/10.1109/TPAMI.1986.4767851).
- [51] L. Vincent and P. Soille, “Watersheds in digital spaces: An efficient algorithm based on immersion simulations,” *IEEE Transactions on Pattern Analysis and Machine Intelligence*, 13, no. 6, pp. 583–598, 1991. doi: [10.1109/34.87344](https://doi.org/10.1109/34.87344).
- [52] R. Girshick, J. Donahue, T. Darrell, and J. Malik, “Region-based convolutional networks for accurate object detection and segmentation,” *IEEE Transactions on Pattern Analysis and Machine Intelligence*, 38, no. 1, pp. 142–158, 2016. doi: [10.1109/TPAMI.2015.2437384](https://doi.org/10.1109/TPAMI.2015.2437384).
- [53] G. Coleman and H. Andrews, “Image segmentation by clustering,” *Proceedings of the IEEE*, 67, no. 5, pp. 773–785, 1979. doi: [10.1109/PROC.1979.11327](https://doi.org/10.1109/PROC.1979.11327).
- [54] J. Long, E. Shelhamer, and T. Darrell, “Fully convolutional networks for semantic segmentation,” in *2015 IEEE Conference on Computer Vision and Pattern Recognition (CVPR)*, 2015, pp. 3431–3440. doi: [10.1109/CVPR.2015.7298965](https://doi.org/10.1109/CVPR.2015.7298965).
- [55] O. Ronneberger, P. Fischer, and T. Brox, *U-Net: Convolutional networks for biomedical image segmentation*, 2015. arXiv: [1505.04597 \[cs.CV\]](https://arxiv.org/abs/1505.04597).
- [56] L.-C. Chen, G. Papandreou, I. Kokkinos, K. Murphy, and A. L. Yuille, “Deeplab: Semantic image segmentation with deep convolutional nets, Atrous convolution, and fully connected CRFs,” *IEEE Transactions on Pattern Analysis and Machine Intelligence*, 40, no. 4, pp. 834–848, 2018. doi: [10.1109/TPAMI.2017.2699184](https://doi.org/10.1109/TPAMI.2017.2699184).
- [57] A. Vaswani, N. Shazeer, N. Parmar, J. Uszkoreit, L. Jones, A. N. Gomez, L. Kaiser, and I. Polosukhin, *Attention is all you need*, 2023. arXiv: [1706.03762 \[cs.CL\]](https://arxiv.org/abs/1706.03762).
- [58] K. He, X. Zhang, S. Ren, and J. Sun, “Deep residual learning for image recognition,” in *2016 IEEE Conference on Computer Vision and Pattern Recognition (CVPR)*, 2016, pp. 770–778. doi: [10.1109/CVPR.2016.90](https://doi.org/10.1109/CVPR.2016.90).
- [59] J. L. Ba, J. R. Kiros, and G. E. Hinton, *Layer normalization*, 2016. arXiv: [1607.06450 \[stat.ML\]](https://arxiv.org/abs/1607.06450).
- [60] D. P. Kingma and J. Ba, *Adam: A method for stochastic optimization*, 2017. arXiv: [1412.6980 \[cs.LG\]](https://arxiv.org/abs/1412.6980).
- [61] A. Raklin, O. Shamir, and K. Sridharan, *Making gradient descent optimal for strongly convex stochastic optimization*, 2012. arXiv: [1109.5647 \[cs.LG\]](https://arxiv.org/abs/1109.5647).
- [62] A. Kirillov, E. Mintun, N. Ravi, H. Mao, C. Rolland, L. Gustafson, T. Xiao, S. Whitehead, A. C. Berg, W.-Y. Lo, P. Dollár, and R. Girshick, *Segment anything*, 2023. arXiv: [2304.02643 \[cs.CV\]](https://arxiv.org/abs/2304.02643).
- [63] T.-Y. Lin, P. Goyal, R. Girshick, K. He, and P. Dollár, “Focal loss for dense object detection,” *IEEE Transactions on Pattern Analysis and Machine Intelligence*, 42, no. 2, pp. 318–327, 2020. doi: [10.1109/TPAMI.2018.2858826](https://doi.org/10.1109/TPAMI.2018.2858826).
- [64] F. Milletari, N. Navab, and S.-A. Ahmadi, “V-net: Fully convolutional neural networks for volumetric medical image segmentation,” in *2016 Fourth International Conference on 3D Vision (3DV)*, 2016, pp. 565–571. doi: [10.1109/3DV.2016.79](https://doi.org/10.1109/3DV.2016.79).
- [65] T. Ren, S. Liu, A. Zeng, J. Lin, K. Li, H. Cao, J. Chen, X. Huang, Y. Chen, F. Yan, Z. Zeng, H. Zhang, F. Li, J. Yang, H. Li, Q. Jiang, and L. Zhang, *Grounded SAM: Assembling open-world models for diverse visual tasks*, 2024. arXiv: [2401.14159 \[cs.CV\]](https://arxiv.org/abs/2401.14159).
- [66] S. Liu, Z. Zeng, T. Ren, F. Li, H. Zhang, J. Yang, C. Li, J. Yang, H. Su, J. Zhu, and L. Zhang, *Grounding DINO: Marrying DINO with grounded pre-training for open-set object detection*, 2023. arXiv: [2303.05499 \[cs.CV\]](https://arxiv.org/abs/2303.05499).
- [67] J. Li, D. Li, C. Xiong, and S. Hoi, *Blip: Bootstrapping language-image pre-training for unified vision-language understanding and generation*, 2022. arXiv: [2201.12086 \[cs.CV\]](https://arxiv.org/abs/2201.12086).

- [68] Y. Zhang, X. Huang, J. Ma, Z. Li, Z. Luo, Y. Xie, Y. Qin, T. Luo, Y. Li, S. Liu, Y. Guo, and L. Zhang, *Recognize anything: A strong image tagging model*, 2023. arXiv: 2306.03514 [cs.CV].
- [69] R. Rombach, A. Blattmann, D. Lorenz, P. Esser, and B. Ommer, *High-resolution image synthesis with latent diffusion models*, 2022. arXiv: 2112.10752 [cs.CV].
- [70] J. Lin, A. Zeng, H. Wang, L. Zhang, and Y. Li, “One-stage 3d whole-body mesh recovery with component aware transformer,” in *2023 IEEE/CVF Conference on Computer Vision and Pattern Recognition (CVPR)*, 2023, pp. 21 159–21 168. doi: 10.1109/CVPR52729.2023.02027.
- [71] C. Wu, S. Yin, W. Qi, X. Wang, Z. Tang, and N. Duan, *Visual ChatGPT: Talking, drawing and editing with visual foundation models*, 2023. arXiv: 2303.04671 [cs.CV].
- [72] X. Huang, Y.-J. Huang, Y. Zhang, W. Tian, R. Feng, Y. Zhang, Y. Xie, Y. Li, and L. Zhang, *Open-set image tagging with multi-grained text supervision*, 2023. arXiv: 2310.15200 [cs.CV].
- [73] Y. Chen, J. Liu, X. Zhang, X. Qi, and J. Jia, *Voxelnest: Fully sparse voxelnet for 3d object detection and tracking*, 2023. arXiv: 2303.11301 [cs.CV].

## Gitlab repository

All source codes for the practical part of this thesis and text files in L<sup>A</sup>T<sub>E</sub>X form can be found in author's faculty gitlab repository here: [gitlab.fit.cvut.cz/seibemic/dp](https://gitlab.fit.cvut.cz/seibemic/dp).

README.md .....	Brief introduction to this thesis
src .....	Source files of this thesis
experiments .....	Figures and graphs for experiments
impl .....	Source code of the implementation of the proposed method
PHD.ipynb .....	Jupyter notebook dedicated for trying out the method
text .....	Folder including files for this thesis in L <sup>A</sup> T <sub>E</sub> X form
seibemic-thesis.pdf .....	The text of this work in PDF format